"A tube based configuration formalism for entangled linear polymers under flow"

Adrien Leygue

"A tube based configuration formalism for entangled linear polymers under flow"

Leygue, Adrien

ABSTRACT

In this thesis, we propose a new microstructural model to describe the rheology of entangled linear polymers. In order to reduce the number of non-linear adjustable parameters, we develop a model capable of predicting both the linear and the non-linear response, using a single set of material parameters. In a first step, a linear differential formulation of the thermal constraint release mechanism is introduced and validated against experimental results for linear polystyrene melts. In a second step, we extend the linear model to the non-linear regime by generalizing the state variables to conformation tensors and accounting for the relevant non-linear relaxation phenomena. The numerical predictions of the resulting model are then compared to experimental data for entangled polymer melts and solutions in different flow regimes. Finally, we show, on a simple reptation model, how the single generator bracket formalism of non-equilibrium thermodynamics can be used for the phenomenological improvement of microstructural constitutive models.

CITE THIS VERSION

Université catholique de Louvain
Faculté des Sciences Appliquées

Center for System Engineering and Applied Mechanics

A tube based configuration formalism for entangled linear polymers under flow

Adrien Leygue

Thèse présentée en vue de l'obtention du grade de Docteur en Sciences Appliquées

Jury:
Christian Bailly (Promoteur), UCL
Antony N. Beris, Univ. Delaware (USA)
Vincent Blondel (Président), UCL
François Dupret, UCL
Roland Keunings (Promoteur), UCL
Giuseppe Marrucci, Univ. Napoli (Italie)
Jay D. Schieber, IIT (USA)
Ken Walters, Univ. Wales (Wales)

Juillet 2005

Acknowledgements

As my time as PhD student comes to an end, I wish to thank those who helped me along the hazardous journey of doctoral research. Those who took an active part in the journey, and those who simply were present and made the journey easier, happier. It is impossible to cite you all, but you should know that your presence was important to me.

My thoughts go in particular to my advisors Roland Keunings and Christian Bailly, for their open-mindedness and their confidence in me. Their positive attitude guided me along my thesis, promoting independent research and thinking. I am also grateful for giving me the opportunity to meet other fellow rheologists around the world, during congresses, workshops or informal meetings.

I very much enjoyed the company of Antony Beris during his sabbatical leave at CESAME. It has been a pleasure working with him and I particularly appreciated his patience while trying to teach us the subtle refinements of non-equilibrium thermodynamics.

For many fruitful discussions, I would like to thank Prof. G. Marrucci, Prof. G. Ianniruberto, Prof. J. Schieber, Dr. M. Laun, Dr. H. Burhin and Dr. C-Y Liu.

Beside my doctoral research, I really appreciated the close collaboration with Vincent Legat in many teaching activities. During our numerous discussions, he also shed some external and valuable light on my research work.

Working within CESAME would not be the same without the famous coffee breaks. I therefore thank all the attendees of these most important social events over the past years.

Two very special persons I wish to thank are Evelyne van Ruymbeke and my long-time officemate and friend Fabrice Loix. Their company clearly made my stay at CESAME brighter.

Finally I am most grateful to Samantha who was with me through the ups and downs of those years. She was there to give me the bit of confidence I was often lacking, and to listen to so many spaghetti-explanations.

Adrien.

Contents

Introduction

It is known to most of us that many of the fluids we encounter, even on a daily basis, cannot be described neither as simple liquids nor as solids. These so-called complex fluids exhibit a complex rheological behaviour. The understanding and the prediction of their flow properties often require understanding the physics of the material at a scale smaller than the one of macroscopic interest.
Polymeric materials belong to the large class of viscoelastic materials. At short time scales, their behaviour is solid-like while their long time behaviour is more liquid-like. The understanding and the prediction, at the size scale of continuum mechanics, of the rheological properties of polymers are a longstanding scientific challenge of the greatest interest for the polymer industry. The processing conditions of e.g. a polymer melt as well as the final properties of the product are deeply influenced by the rheological properties of the material.

In this manuscript, we focus on the microstructural constitutive modelling of topologically linear entangled polymers.

Microstructural modelling is the process in which one tries to predict and understand macroscopic properties of a material, based on its local microstructure. It is aimed at understanding the factors that govern the material behaviour at the size scales at which they are utilized. In this work, the macroscopic level is that of continuum mechanics, while the microscopic level is the molecular scale or an intermediate mesoscopic level. A model consists therefore of two main building blocks:

1. an expression for computing the macroscopic properties from the parameters and variables describing the microstructure.
2. An expression for computing the evolution of the microstructural variables due to the macroscopic strain, the relaxation dynamics of the microstructure and other relevant external driving forces.

Despite the tremendous increase in available computing power, the most promising atomistic simulations are still orders of magnitude below the macroscopic scale in the molecular weight, number of molecules and timescales they can reach [1; 2]. To model the macroscopic behaviour of entangled polymers, it is still necessary to transfer the information from micro-scale models to coarser meso-scale models, keeping only the essence of molecular dynamics. This process often involves averaging some quantities over the set of microscopic variables, and using some closure approximations with sometime uncontrolled consequences [3]. A key issue when dealing simultaneously with two levels of description such as the macroscopic continuum and the atomistic details is to be able to transfer information between those levels and create a coupling dynamics occurring at different size- and time-scales.

Continuum mechanics models for entangled polymers focus on the polymeric contribution to the stress tensor found in the conservation equation of momentum. In microstructural models, one assumes that, at each material point, there is a microstructure which can be characterized by a set of identifiable constants and variables. Furthermore, the mathematical expressions for the stresses induced by the microstructure and the dynamics of the microstructural variables are derived from assumptions on the physical processes found within the microstructure. Apart from the stresses, microstructural models can provide additional information on the state of the microstructure such as its average orientation. This extends the scope of the model and allows for its validation through the comparison with experimental measurements other than the stress.

Microstructural models used to model entangled polymers are often opposed to so-called phenomenological models that do not try to bridge length scales. Phenomenological models are often simply considered as black-box models, with enough adjustable parameters, that only focus on relating the stresses to the strain history. The faint connection between model and the physics of the material only allows the model to be used as a predictive tool whose parameters are not a priori connected to any specific physical property. Such phenomenological models are nevertheless useful when the investigated system is too complex to model from first principles.
The line between microstructural and phenomenological models is actually thinner that one would tend to believe, and many models with microstructural foundations are used as phenomenological models with adjustable parameters.

In this thesis, we build a differential microstructural constitutive model for polydisperse entangled linear polymers. In order to reduce the number of non-linear adjustable parameters, the model should aim at predicting both the linear and the non-linear response of entangled linear polymers with the same parameters. This would allow most of the parameters to be identified on the linear response for which both experiments and theory are more reliable. The relevance of the linear parameters in

non-linear flows could also be evaluated.

We take the first step towards this constitutive model by constructing a mathematically linear model that can quantitatively predict the linear response of linear entangled polymers. The most critical part actually is to derive a general linear differential expression for the thermal constraint release mechanism. In a second step, we extend the linear model to the non-linear regime by generalizing the state variables to conformation tensors and accounting for the relevant non-linear relaxation phenomena. The numerical predictions of the resulting model are then compared to experimental data for entangled polymer melts and solutions in different flow regimes.

This manuscript is structured as follows: chapters 1 to 4 focus on the construction and the evaluation of the model. They correspond to published or submitted publications to referred scientific journals. There is a strong continuity between those chapters, as each of them presents an extension or an application of the previous ones. Chapter 5 presents some early work on reptation models. Beside the scientific results, this chapter is meant to propose a path for the possible extension of the model built in the previous chapters. In a last section named *Related Contributions* we present some additional doctoral research carried out in the frame of this thesis.

In chapter 1, we present a new differential formulation of the thermal constraint release phenomenon for linear entangled polymers. This new formulation predicts a relaxation modulus identical to that predicted by the double reptation theory of Tsenoglou [4] or Des Cloizeaux [5] for both monodisperse and polydisperse systems. Additionally, we discuss a simple approximation of our approach as well as its possible use for building simple constitutive equations that account for constraint release in a polydisperse environment.

This chapter has been the subject of the following publication:
A. Leygue, C. Bailly, R. Keunings. A differential formulation of thermal constraint release for entangled polymers. *J. Non Newtonian Fluid Mech.*, In press, 2005.

The following communication is also based on this work:

- A. Leygue, C. Bailly, R. Keunings. A New Formulation of the Double Reptation Theory, Proc 6th Nat. Congress on Theoretical and Applied Mechanics, E. Dick et al. (Eds), paper #121 in edited CD-ROM (2003).

In chapter 2, we present a simple tube theory for linear entangled polymers that accounts for reptation, contour-length fluctuations and thermal constraint release. This theory is based on a new differential formulation of the thermal constraint release phe-

nomenon presented in chapter 1 which is extended here to account for contour-length fluctuations. We apply the theory to mono- and poly-disperse polystyrene melts and demonstrate its ability to produce quantitative predictions. Additionally, we discuss a linear approximation of our approach that preserves the structure of the model. While most quantitative tube theories for predicting the linear viscoelasticity are mathematically non-linear, our approach allows one to address the linear viscoelastic response of a polydisperse entangled system with a linear theory.

This chapter has been the subject of the following publication:
A. Leygue, C. Bailly, R. Keunings. A differential tube-based model for predicting the linear viscoelastic moduli of polydisperse entangled linear polymers. *J. Non Newtonian Fluid Mech.*, Submitted 2005.

In chapter 3, we present a tube-based constitutive model for polydisperse entangled linear polymers. The model is constructed as the non-linear extension of the linear model presented in chapter 2, which is capable of predicting quantitatively the linear viscoelasticity of polydisperse linear systems. The constitutive equation accounts for the major linear and non-linear phenomena thought to be important in the description of entangled linear polymers: reptation, contour-length fluctuations, thermal constraint release, convective constraint release and chain stretch effects. In the non-linear regime convective constraint release couples the relaxation of the different masses and provides a non-linear mixing rule for the model. The predictive capabilities of the model are tested on published results for mono- and bi-disperse entangled solutions [6; 7], both in shear and extension.

This chapter has been the subject of the following publication:
A. Leygue, C. Bailly, R. Keunings. A tube-based constitutive equation for polydisperse entangled linear polymers. *J. Non Newtonian Fluid Mech.*, Submitted 2005.

The following communications are also based on this work:

- A. Leygue, C.Y. Liu, N. Coppin, H. Burhin, C. Bailly, R. Keunings, Evaluation of a new constitutive equation for mixtures of entangled linear polymers and application to the study of LAOS flow of polystyrene melts, 76th Annual Meeting of the American Society of Rheology, Lubbock, Texas, USA (February 2005).
- A. Leygue, C. Bailly, R. Keunings. Evaluation of a new constitutive equation for blends of entangled linear polymers, Proc. 14th Int. Congress on Rheology, Korean Society of Rheology, Seoul, paper #280 in edited CD-ROM (2004).
- A. Leygue, C. Bailly, R. Keunings, A Constitutive Equation for Blends of Entangled Linear Polymers, 1st Ann. European Rheology Conf. (AERC 2003),

Guimarães, Portugal (September 2003).

In chapter 4, we discuss the predictive capabilities of the CRAFT model derived in chapter 3. Numerical predictions of the model are compared to experimental data of Large Amplitude Oscillatory Shear (LAOS) flows and uniaxial extension of well characterized polystyrene samples. All the parameters of the CRAFT model are identified from the linear viscoelastic moduli of a subset of the samples or derived from microstructural knowledge.
We find that for monodisperse systems, the CRAFT model can quantitatively reproduce the experimental LAOS data. For polydisperse systems, discrepancies appear as high mass chains show some anomalous stretch in shear. In extension, the model can predict quantitatively the unique experimental data of Bach et al. [8] provided that finite extensibility is reduced to very low values.

This chapter will be the subject of a publication which is currently in preparation.

The following communication is also based on this work:

- A. Leygue, C.Y. Liu, N. Coppin, H. Burhin, C. Bailly, R. Keunings, Investigation of LAOS flow of polydisperse polystyrene melts using a new constitutive equation for mixtures of entangled linear polymers, 2nd Ann. European Rheology Conf. (AERC 2005), Grenoble, France (April 2005).
- A. Leygue, C. Bailly, R. Keunings, A Differential Constitutive Equation for the Simulation of Linear Polydisperse Entangled Systems: Evaluation for Not So Simple Flows, XIVth Int. Workshop on Numerical Methods for Non-Newtonian Flows, Santa Fe, New Mexico, USA (June 2005).

In chapter 5, using the single generator bracket formalism of non-equilibrium thermodynamics, we build a thermodynamically consistent constitutive equation of the differential type for linear entangled polymers. The starting point of our developments is the MGI rheological model proposed by Marrucci et al. [9] , which can be viewed as a modification of the classical Doi-Edwards reptation theory that includes convective constraint release and a modified strain measure. The proposed constitutive equation has an additional parameter which governs the dissipative part of the model. The MGI model is recovered as a particular case, but with a stress-conformation relationship which contains an additional term suggested by non-equilibrium thermodynamics. Predictions of the proposed model in steady and transient shear flows are shown to be in qualitative agreement with experimental observations.

This work has been the subject of the following publication:

A. Leygue, A.N. Beris, R. Keunings. A constitutive equation for entangled linear polymers inspired by reptation theory and consistent with non-equilibrium thermodynamics. *J. Non Newtonian Fluid Mech.*, 101:95–111, 2001.

The following communications are also based on this work:

- A. Leygue, A.N. Beris, R. Keunings, A Constitutive Equation for Entangled Linear Polymers Inspired by Reptation Theory and Consistent with Non-Equilibrium Thermodynamics, XIIth Int. Workshop on Numerical Methods for Non-Newtonian Flows, Monterey, California, USA (July 2001).
- A. Leygue, A.N. Beris, R. Keunings, Constitutive Equations for Linear Polymer Melts Inspired by Reptation Theory and Non-Equilibrium Thermodynamics, 72nd Annual Meeting of the American Society of Rheology, Hilton Head Island, South Carolina, USA (February 2001).
- A. Leygue, A.N. Beris, R. Keunings, Modelling the Flow of Linear Polymer Melts Using a Modified Version of the MGI Model, 4th EUROMECH Fluid Mechanics Conference, Eindhoven, The Netherlands (November 2000).
- A. Leygue, A.N. Beris, R. Keunings, Thermodynamical Considerations on Constitutive Equations for Entangled Polymer Melts. Proc. 13th Int. Congress on Rheology, D.M. Binding et al. (Eds), British Society of Rheology, Glasgow, Vol. 2, 111-113 (2000).
- A. Leygue, A.N. Beris, R. Keunings, Using Non-Equilibrium Thermodynamics to Improve the Modelling of Linear Polymer Melts, with Convective Constraint Release and Force Balance on Entanglements, Workshop on Non-Equilibrium Thermodynamics and Complex Fluids, Oxford, UK (August 2000).

In section Related Contributions A, we study the flow response in large amplitude oscillatory shear of the molecular stress function (MSF) model that has recently been proposed by Wagner *et al.* [10]. The MSF model is derived from molecular theory and has only two parameters to describe the nonlinear material response. The model predictions are analysed in both the frequency and time domain. It shows good agreement with experimental data for a linear high density polyethylene melt. At low and medium strains, MSF model predictions are in excellent agreement with experimental data and predictions of a six-mode Giesekus model which has six parameters to describe the nonlinear material response. At medium strains, the basic Doi–Edwards model, which has no nonlinear parameters, already underpredicts the data. At high strains, the MSF model predictions agree slightly better with the experimental data than the Giesekus model. Surprisingly, however, it is the Doi–Edwards model that shows excellent agreement with experimental data at high strains. For the linear melt

we consider, it outperforms the models that have nonlinear parameters, both in the time and frequency domain.

This work has been the subject of the following publication:
P. Wapperom, A. Leygue, R. Keunings. Numerical simulation of large amplitude oscillatory shear of a high-density polyethylene melt using the MSF model. *J. Non Newtonian Fluid Mech.*, Accepted for publication.

Chapter 1

A differential formulation of thermal constraint release for entangled linear polymers

1.1 Introduction

Following the introduction on the reptation picture by de Gennes [11], Doi and Edwards [12] proposed a tube-based theory to explain the linear rheology of linear entangled polymers. The numerous variations of the tube model have now reached a high level of maturity and are now capable of a quantitative description of the linear viscoelastic properties of linear entangled polymers (see e.g. [13; 14; 15; 16; 17]). The success of these theories is such that the focus is now on the prediction of the linear viscoelastic response of systems with a much more complex architecture, e.g. symmetric [18] or asymmetric stars [19], and mixtures of star and linear polymers [20; 21]. The key of these successes essentially is an accurate description of: (i) the reptation dynamics (if present), (ii) the fluctuations of the length of the tube [12], and (iii) thermal constraint release phenomena [22], which is a closure to the mean field approximation of the tube. Accounting for the coupling between those effects is of critical importance. For linear polymers, the distinction made between reptation and contour length fluctuations is somehow arbitrary as these are only different modes of a one-dimensional Rouse chain escaping a tube. This distinction has recently been made thinner by Graham and co-workers [23] who proposed to model the relaxation

through reptation and contour length fluctuations using a modified diffusion process, where diffusivity is position-dependent along the primitive path. Thermal constraint release is today handled efficiently either through dynamic dilution or through double reptation [5; 4]. The latter theory can actually be viewed as an approximation of Rouse tube motion induced by constraint release events. In the monodisperse case, Likhtman et al. [16] have showed how double reptation is a good approximation of Rouse tube motion. The mixing rule induced by double reptation has also been recovered within the implementation of constraint release found in a stochastic full chain reptation model developed by Hua et al. [24].
A more complete theory of constraint release involving both tube dilation and rouse tube motion has been proposed by Viovy et al. [25].

In the present text, we present a new mathematical formulation of the thermal constraint release phenomenon for monodisperse systems, which we prove to be equivalent to the double reptation theory of Des Cloizeaux [5] and Tsenoglou [4]. This new formulation is then extended to the case of polydisperse systems where it yields a mixing rule identical to the one of double reptation. In parallel, we propose a simple approximation of our theory, which can easily be used as a starting point for building non-linear constitutive equations of the differential type. Finally, we show that our approach to constraint release can simplify integral non-linear integral constitutive equations of polydisperse systems such as the extension proposed by Pattamaprom et al. [6] of the so-called MLD model of Mead et al. [26].

1.2 Classical double reptation

In this section, we first recall basic elements of reptation theory and its extension to double reptation. In a fixed network of entanglements, reptation theory [11; 12] suggests that a polymeric chain is constrained in a tube-like region and therefore can only relax through curvilinear diffusion along its primitive path. Neglecting length fluctuations of the primitive path, one can describe the relaxation of the chain (or equivalently the destruction/renewal of the tube) through the following diffusion equation [12]:

$$\begin{aligned} \frac{\partial P_0}{\partial t} &= \alpha_d \frac{\partial^2 P_0}{\partial s^2} \,, \\ P_0(t,-1) &= 0 \,, \\ P_0(t,1) &= 0 \text{ for } t > 0 \,, \\ P_0(0,s) &= 1 \text{ for } -1 < s < 1 \,, \end{aligned} \tag{1.1}$$

where the equilibrium length of the primitive chain has been normalized to 2 and α_d is a characteristic diffusion constant scaling like the inverse of the cube of the molecular

mass. The subscript $\cdot_0$ indicates that we do not consider any constraint release yet.

The quantity $P_0(t^*,s)$ is the probability for a tube segment with curvilinear position s along the primitive chain of not having relaxed between $t=0$ and $t=t^*$.

From P_0, we define the relaxation kernel K_0 as:

$$K_0(t) = \frac{1}{2}\int_{-1}^{1} P_0(t,s)\,\mathrm{d}s\ , \tag{1.2}$$

which is but the average of P_0 over s. Using the analytical solution of (1.1), the relaxation kernel $K_0(t)$ can be found to be [12]:

$$K_0(t) = \frac{8}{\pi^2}\sum_{p\,\mathrm{odd}}\frac{1}{p^2}\exp\left(-\frac{p^2 t}{\tau_\mathrm{d}}\right)\ , \tag{1.3}$$

where the longest relaxation time τ_d is defined as:

$$\tau_\mathrm{d} = \frac{4}{\pi^2\,\alpha_d}. \tag{1.4}$$

Under simple reptation the relaxation modulus $G_0(t)$ is proportional to the relaxation kernel:

$$G_0(t) = G_N^0 K_0(t)\ , \tag{1.5}$$

where G_N^0 is the plateau modulus.

Introduced by Tsenoglou [4] and Des Cloizeaux [5], double reptation takes into account the mutual interactions of relaxing chains. In a sense, it is a closure to the mean field approximation of the tube. If one assumes that chains interact in a binary fashion (through entanglements), then whenever a chain segment relaxes through reptation, another segment must also relax through thermal constraint release. For mono-disperse linear entangled polymers, this simply gives the following relaxation modulus [5]:

$$G^\star(t) = G_N^0\,(K_0(t))^{1+\gamma}\ , \tag{1.6}$$

where γ should be equal to unity, but is often left as an adjustable parameter. A classical choice is to take γ slightly above unity ($\gamma = 4/3$)[27].

Except for the factor G_N^0, $G^\star(t)$ is the power $(1+\gamma)$ of $G_0(t)$. As $G_0(t)$ is often approximated by its dominant exponential, a crude approximation of double reptation is therefore to simply divide the characteristic relaxation time τ_d by $(1+\gamma)$.

In a polydisperse system, double reptation provides a mixing rule for predicting the relaxation modulus based on the relaxation kernel of all the present species:

$$G^\star(t) = G_N^0 \left(\sum_{i=1} \phi^{(i)} K_0^{(i)}(t) \right)^{1+\gamma}, \tag{1.7}$$

where $\phi^{(i)}$ is the volume fraction of species i, and $K_0^{(i)}$ its relaxation kernel. The disengagement time $\tau_d^{(i)}$ of species (i) is then assumed to be proportional to a particular power of the molecular weight $M^{(i)}$ of the species. This use of double reptation as a mixing rule is quite common and has been proved to give good predictions of the relaxation modulus as a function of the molecular weight distribution of the sample (see e.g. [14; 15]).

1.3 Constraint release in monodisperse systems

In this section, we propose a modification to Eq. (1.1) in order to simultaneously account for reptation and constraint release through double reptation. We will not address the issue of contour length fluctuations in this work as we wish to focus on the thermal constraint release phenomenon only. The incorporation of contour length fluctuations might indeed lead us to modify the typical diffusion operator of the reptation theory.

The classical approach of double reptation is based on the principle of first computing the relaxation kernel of a chain relaxing in a fixed network, and then modifying it in order to take into account the effect of the surrounding relaxing chains. This two-step method is not suited for the construction of non-linear constitutive equations, as the mixing rule is nonlinear, and does not offer a dynamical description of the processes involved. Instead, we would like to find a differential problem, similar to Eq.(1.1), such that it would describe the relaxation dynamics of the different segments of the primitive chain under reptation and thermal constraint release.

As any segment of the primitive chain can relax either through reptation or constraint release, we choose to add a second term on the right hand side of Eq.(1.1) to account for the latter phenomena. This new term is constructed as follows: Assuming that thermal constraint release can occur with the same probability on any unrelaxed segment [22], it must have an intensity, along the chain, proportional to the fraction of

locally unrelaxed segments. This leads to the following differential problem:

$$\begin{aligned} \frac{\partial P_\gamma}{\partial t} &= \alpha_d \frac{\partial^2 P_\gamma}{\partial s^2} + \beta P_\gamma \,, \\ P_\gamma(t,-1) &= 0 \,, \\ P_\gamma(t,1) &= 0 \text{ for } t > 0 \,, \\ P_\gamma(0,s) &= 1 \text{ for } -1 < s < 1 \,, \end{aligned} \tag{1.8}$$

where β is the rate of thermal constraint release. Following the concept of double reptation, we make this rate proportional to the rate of relaxation through reptation:

$$\beta(t) = \gamma \frac{\int_{-1}^{1} \alpha_d \frac{\partial^2 P_\gamma}{\partial s^2} \,\mathrm{ds}}{\int_{-1}^{1} P_\gamma \,\mathrm{ds}} \,, \tag{1.9}$$

where the parameter γ describes the fact that the relaxation of one chain segment through reptation might induce the relaxation of more than one other segment ($\gamma \geq 1$). We will prove later that γ actually is the same as is Eq. (1.6). It is worth noticing that due to the sign and concavity of $P_\gamma(t,s)$, we have $\beta(t) <= 0$. This is consistent with the plus-sign found on the right-hand-side of Eq. (1.8). As $\beta(t)$ is not constant in time, the relaxation due to constraint release does not obey a simple first order decay.

Another interpretation of Eqs. (1.8,1.9) is the following: For any tube segment that relaxes on a given chain through reptation, there is another tube segment that will relax. While the first disappearing segment will be located at a chain end, the second has to be picked randomly among all the unrelaxed tube segments. The expression $\int_{-1}^{1} \alpha_d \frac{\partial^2 P_\gamma}{\partial s^2} \,\mathrm{ds}$ simply measures the rate of relaxation through reptation, while the function $\frac{P_\gamma}{\int_{-1}^{1} P_\gamma \,\mathrm{ds}}$ describes how this rate of relaxation should be redistributed along the chain; i.e. proportionally to the local fraction of unrelaxed chain segments (or surviving tube segments).

It can be verified by simple substitution that Eqs. (1.8-1.9) have the following analytical solution:

$$P_\gamma(t,s) = P_0(t,s) \left(\frac{1}{2} \int_{-1}^{1} P_0(t,s') \,\mathrm{ds}' \right)^\gamma = P_0(t,s) \left(K_0(t)\right)^\gamma \,, \tag{1.10}$$

which is a product of two factors where the first one can be interpreted as accounting for the relaxation of a chain in a fixed environment, while the second one would account for the relaxation of the environment.

Finally, we define the relaxation modulus $G_\gamma(t)$ as proportional to the fraction of

unrelaxed chain segments:

$$G_\gamma(t) = G_N^0 \frac{1}{2} \int_{-1}^{1} P_\gamma(t,s)\, \mathrm{d}s \ . \tag{1.11}$$

This approach to constraint release predicts exactly the same relaxation modulus as double reptation. The equivalence of both formulations is easily seen through the comparison of Eqs. (1.6) and (1.11), where P_γ has been substituted by its analytical expression (1.10). We also see that the parameter γ has the same meaning in both formulas and that the expression (1.9) for β can be simplified as:

$$\beta(t) = \gamma \frac{\dfrac{\partial K_0(t)}{\partial t}}{K_0(t)} \ . \tag{1.12}$$

In describing the relaxation of a polymeric system one might not only be interested in the relaxation modulus $G_\gamma(t)$ but also in the dynamics of relaxation through reptation and constraint release along the chain. Such information is needed, for example, in the full contour-variable reptation model proposed by Mead and coworkers [26]. Under simple reptation, tube segments are renewed at the chain's ends only, while thermal constraint release allows the renewal of the orientation of internal tube segments. If one neglects constraint release ($\gamma = 0$), the variation of $P_0(t,s)$ is only due to a flux from the inside of the chain towards the chain's ends, where all the actual relaxation occurs. When γ is not zero, $P_\gamma(t,s)$ also decreases due to a local relaxation, and the total loss along the chain is γ times the loss at the chain's ends. This difference in the dynamics of internal segments can be best observed at early times when looking at the relaxation of the segments at the center of the chain. On Fig. 1.1, we compare $P_0(t,s)$ and $P_\gamma(t,s)$ at the center of the chain; i.e. $s = 0$ and for $\gamma = 1$. At early times, $P_0(t,0)$ exhibits a plateau which comes from the fact that inner segments can only relax through reptation and must therefore wait for the chain to reptate far enough before having the opportunity to relax. On the other hand, we see that $P_\gamma(t,0)$ does not have that feature, as some inner segments can relax through thermal constraint release as soon as the outer segments relax through reptation.

1.4 Construction of a simple linear viscoelastic model

From the partial differential equation (PDE) (1.8) we proposed for the evolution of P_γ, it is possible to build a linear viscoelastic model that accounts for both reptation and constraint release in simple shear flows. Let us define $\sigma(t,s)$ as the non-dimensional

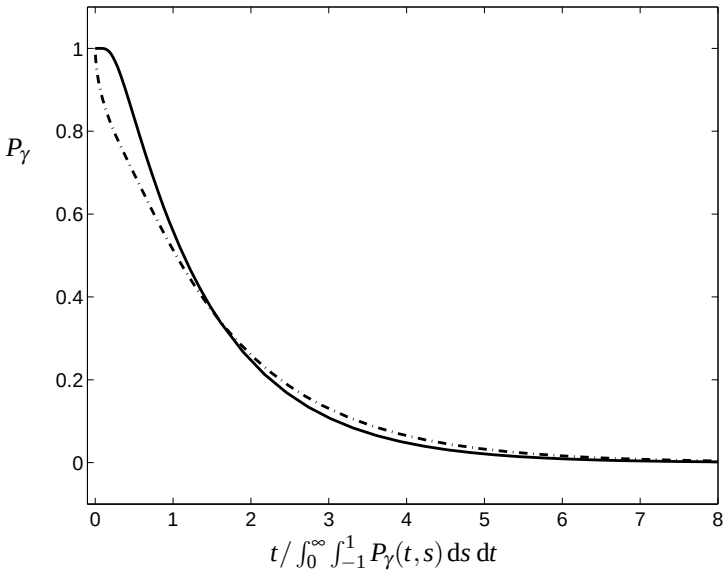

Figure 1.1: Comparison of the relaxation dynamics at the center of the primitive chain with ($P_1(t,0)$: $\cdot-$) and without ($P_0(t,0)$: $-$) constraint release.

stress carried at time t by tube segments at position s along the primitive path.

$$\sigma(t,s) = \int_{-\infty}^{t} P_\gamma(t-t',s)\dot{\gamma}_{xy}(t')\,\mathrm{d}t', \tag{1.13}$$

where $\dot{\gamma}_{xy}(t')$ is the shear rate at time t'. This simple linear model reads:

$$\begin{aligned}
\frac{\partial\sigma}{\partial t} &= \dot{\gamma} + \alpha_d \frac{\partial^2\sigma}{\partial s^2} + \int_{-\infty}^{t} \beta(t-t') P_\gamma(t-t',s)\dot{\gamma}_{xy}(t')\,\mathrm{d}t' \,, \qquad (1.14)\\
\sigma(t,-1) &= 0 \,,\\
\sigma(t,1) &= 0 \text{ for } t>0 \,,\\
\sigma(0,s) &= 0 \text{ for } -1<s<1 \,,\\
\beta(t) &= \gamma \frac{\frac{\partial K_0(t)}{\partial t}}{K_0(t)} \,, \qquad (1.15)\\
\tau_{xy}(t) &= G_N^0 \frac{1}{2}\int_{-1}^{1} \sigma(t,s)\,\mathrm{d}s \,,
\end{aligned}$$

where τ_{xy} is the shear stress.

In order to obtain from (1.14-1.15) a simple differential linear model we approximate the relaxation kernel $K_0(t)$ appearing in Eq. (1.15) by a single decreasing expo-

nential with characteristic time $\gamma\tau_{\rm cr}$. The new model simply reads:

$$\begin{aligned} \frac{\partial\sigma}{\partial t} &= \dot{\gamma} + \alpha_d \frac{\partial^2\sigma}{\partial s^2} - \frac{\sigma}{\tau_{\rm cr}} \,, \\ \sigma(t,-1) &= 0 \,, \\ \sigma(t,1) &= 0 \text{ for } t > 0 \,, \\ \sigma(0,s) &= 0 \text{ for } -1 < s < 1 \,, \\ \tau_{xy} &= G_N^0 \frac{1}{2} \int_{-1}^{1} \sigma \, \mathrm{d}s \,. \end{aligned} \tag{1.16}$$

The response of this simplified model after a unit step strain is:

$$\sigma(t,s) = P_0(t,s) \exp\left(-\frac{t}{\tau_{\rm cr}}\right) . \tag{1.17}$$

The scalar $\tau_{\rm cr}$ is of the order of τ_d and represents the average disentanglement time through thermal constraint release phenomena. Its value is chosen such that Eqs. (1.14) and (1.16) yield the same zero-shear viscosity. From the analytical solution of (1.16), we find that $\tau_{\rm cr}$ is the solution of the following equation:

$$\int_0^{+\infty} (K_0(t))^{(1+\gamma)} \, \mathrm{d}t = \int_0^{+\infty} \left(K_0(t) \exp\left(-\frac{t}{\tau_{\rm cr}}\right)\right) \mathrm{d}t \,. \tag{1.18}$$

The approximate model (1.16) is of little use by itself, but it is a first step towards a more realistic non-linear differential constitutive equation which would have the same structure in terms of differential operators along the s coordinate.

The zero-shear viscosity η_0 predicted by these models is a function of α_d and γ. It can easily be proved that η_0 scales like α_d^{-1}, but does not scale exactly like $(1+\gamma)^{-1}$. For $\gamma = 0$ we can prove that $\eta_0 = \dfrac{G_N^0}{3\alpha_d}$, but for higher values of γ we have to compute η_0 numerically. Defining the effective relaxation time $\tau_{\rm eff}$ as $\tau_{\rm eff} = \dfrac{\eta_0}{G_N^0}$, we illustrate on Fig. (1.2) how this quantity changes with respect to γ. When $\gamma = 1$, the effective relaxation time is less than half (≈ 0.42) the relaxation time when double reptation is ignored. Thermal constraint release is traditionally accounted for in constitutive equations simply by dividing the relaxation time by 2, which is apparently not enough when one considers the full spectrum of relaxation times instead of the dominant one only.

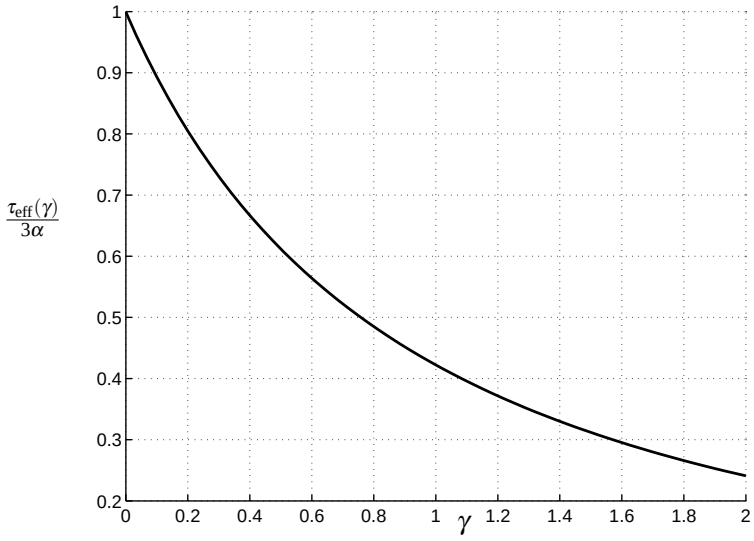

Figure 1.2: Normalized effective relaxation time as a function of γ

1.5 Constraint release in polydisperse systems

Using the same approach, the above formulation of constraint release can easily be extended to polydisperse systems.

In the absence of thermal constraint release, we can consider that all species reptate independently. From a modeling point of view, this would lead to a set of uncoupled partial differential equations (PDEs), where each PDE describes a particular species. As soon as constraint release comes into play, the relaxation of the species is coupled because they are each other's environment (including themselves). The key issue is therefore to compute consistently the rate β of relaxation of the environment.

Assuming that the polydisperse system is made of molecules with a discrete distribution of N masses, let us define $P_\gamma^{(i)}(t,s)$ as the tube survival probability for molecules

of mass $M^{(i)}$. The time evolution of $P_\gamma^{(i)}(t,s)$ is described by the following PDE:

$$\begin{aligned} \frac{\partial P_\gamma^{(i)}}{\partial t} &= \alpha_d^{(i)} \frac{\partial^2 P_\gamma^{(i)}}{\partial s^2} + \beta P_\gamma^{(i)} , \\ P_\gamma^{(i)}(t,-1) &= 0 , \\ P_\gamma^{(i)}(t,1) &= 0 \text{ for } t > 0 , \\ P_\gamma^{(i)}(0,s) &= 1 \text{ for } -1 < s < 1 . \end{aligned} \tag{1.19}$$

In view of Eq. (1.9), the rate of constraint release β is consistently defined as:

$$\beta = \gamma \frac{\sum_i \phi^{(i)} \int_{-1}^{1} \alpha_d^{(i)} \frac{\partial^2 P_\gamma^{(i)}}{\partial s^2} \, \mathrm{d}s}{\sum_i \phi^{(i)} \int_{-1}^{1} P_\gamma^{(i)} \, \mathrm{d}s} , \tag{1.20}$$

where $\phi^{(i)}$ is the volume fraction of species (i) and γ keeps the same meaning as in the monodisperse case. The diffusion coefficient $\alpha_d^{(i)}$ has the form:

$$\alpha_d^{(i)} = \frac{4}{\pi^2 K_d \left(M^{(i)}\right)^3} , \tag{1.21}$$

where K_d is an adjustable material parameter and the exponent 3 accounts for the scaling of the disengagement time τ_d with respect to the molecular mass.

When $\gamma = 0$, all PDEs (1.19)are decoupled and their solutions $P_0^{(i)}(t,s)$ can be computed easily as each equation describes the relaxation through simple reptation of a particular species. When $\gamma \neq 0$, Eq.(1.19) has the following solution:

$$P_\gamma^{(i)}(t,s) = P_0^{(i)}(t,s) \left(\sum_j \frac{1}{2} \int_{-1}^{1} \phi^{(j)} P_0^{(j)}(t,s') \, \mathrm{d}s' \right)^\gamma , \tag{1.22}$$

and $P_0^{(i)}(t,s)$ is the tube survival probability under simple reptation. In the previous expression, the first term accounts for the relaxation of the chains through reptation only, while the second accounts for the relaxation of the environment. Finally, we define the relaxation modulus as:

$$G_\gamma(t) = G_N^0 \sum_i \frac{\phi^{(i)}}{2} \int_{-1}^{1} P_\gamma^{(i)}(t,s) \, \mathrm{d}s . \tag{1.23}$$

It is straightforward to check that the resulting modulus is identical to the modulus one would obtain with the mixing rule (1.7) of double reptation.

Similarly to what we did for monodisperse systems, it is possible to build upon this approach a linear viscoelastic model for polydisperse systems. Defining $\sigma^{(i)}(t,s)$ as

the stress carried by chain segments of species (i) and coordinate s along the primitive path, we obtain the following model:

$$\begin{aligned}
\frac{\partial \sigma^{(i)}}{\partial t} &= \dot{\gamma} + \alpha_d \frac{\partial^2 \sigma^{(i)}}{\partial s^2} + \int_{-\infty}^{t} \beta(t-t') P_\gamma^{(i)}(t-t',s)\dot{\gamma}_{xy}(t')\,\mathrm{d}t' \,, \quad (1.24)\\
\sigma^{(i)}(t,-1) &= 0 \,,\\
\sigma^{(i)}(t,1) &= 0 \text{ for } t>0 \,,\\
\sigma^{(i)}(0,s) &= 0 \text{ for } -1<s<1 \,,\\
\beta(t) &= \gamma \frac{\sum_i \phi^{(i)} \frac{\partial K_0{}^{(i)}t)}{\partial t}}{\sum_i \phi^{(i)} K_0^{(i)}(t)} \,, \quad (1.25)\\
\tau_{xy}(t) &= G_N^0 \sum_i \frac{\phi^{(i)}}{2} \int_{-1}^{1} \sigma^{(i)}(t,s)\,\mathrm{d}s \,. \quad (1.26)
\end{aligned}$$

This linear viscoelastic model only needs N objects, namely the N functions $\sigma^{(i)}$ to reproduce the full complexity of thermal constraint release within a polydisperse system of N masses. It is also capable of accounting for an arbitrary mixing exponent γ. This new formulation of constraint release could therefore be used as a starting point for the implementation of complex integral constitutive equations for polydisperse systems.

The classical way to implement double reptation in a constitutive equation is to make the assumption of binary interactions between chains (i.e. $\gamma = 1$), and to have an equation for each possible interaction between all N masses. As many as N^2 modes (all $M^{(i)}$ $M^{(j)}$ pairs) are therefore required to fully model double reptation.
Such a constitutive equation has been proposed by Pattamaprom and Larson [6], as an extension of the so-called toy-MLD model by Mead and coworkers [26]. The implementation of thermal constraint release (or reptative constraint release, following the authors) within the polydisperse version of the toy-MLD model accounts for all possible interactions (N^2) between all N polymeric masses. This high algorithmic complexity can dramatically increase the computational simulation cost when dealing with polymeric systems composed of many different masses.

Using Eqs. (1.24-1.26) to implement thermal constraint release removes the constraint on the value of γ and reduces the algorithmic complexity of the resulting model.

1.6 Conclusions

We have proposed a new differential formulation of thermal constraint release in monodisperse and polydisperse entangled polymeric systems. The core of our ap-

proach is a differential problem that allows the direct computation of the tube survival probability when both reptation and thermal constraint release are active. Although this theory predicts a relaxation modulus mathematically equivalent to the one predicted by the double reptation theory of Tsenoglou [4] and Des Cloizeaux [5], it does not use a nonlinear mixing rule, and thus is easier to extend to a full constitutive equation.

Chapter 2

A differential tube-based model for predicting the linear viscoelastic moduli of polydisperse entangled linear polymers

2.1 Introduction

Tube theories addressing the quantitative prediction of the linear viscoelastic properties of entangled systems based on their microstructure have now reached a high level of maturity. Following the pioneering work of de Gennes [11] on reptation, numerous tube models are now capable of a quantitative description of the linear viscoelastic properties of linear entangled polymers (see e.g. [13; 14; 15; 16; 17]). The success of these theories is such that the focus is now on the prediction of the linear viscoelastic response of systems with a much more complex architecture such as mixtures of star and linear polymers [20; 28; 29]. A striking fact about all those theories is that they are highly non-linear, despite their focus on the linear rheology of entangled systems.

In order to predict the relaxation modulus of an entangled polymer, one must de-

scribe how the polymeric chains escape from their constraining tubes and how this relaxation process affects the tubes themselves. For linear polymers, the escape of a chain can occur through reptation or contour-length fluctuations [12]. Although they are often addressed separately, these two phenomena can be viewed as different modes of a Rouse chain trapped in a tube potential. For example, the stochastic description of linear chains [24; 30; 16] does not consider reptation and fluctuations separately as fluctuations correspond to the breathing modes of a one-dimensional Rouse chain escaping from a tube. Different authors have proposed coupled descriptions of reptation and contour-length fluctuations either considering a position-dependent [31; 23] or a time-dependent [32] diffusion process along the primitive path.

Thermal Constraint Release [22] theories address the effects, on the tube, of the relaxation of the surrounding chains. In a sense, constraint release is a closure to the tube potential. A rigorous description of constraint release proposed by Viovy et al. [25] results in a potential increase in the effective tube diameter and a Rouse motion of the tube itself. The double reptation picture [4; 5] provides a simple and successful alternative to complex constraint release theories. Double reptation actually is a fair approximation of Rouse tube motion induced by constraint release events. Likthman and Mc Leish have recently shown that generalized double reptation is essentially correct up to the Rouse time of the chain [16]. For polydisperse systems, double reptation induces a non-linear mixing rule which has actually been recovered in the stochastic reptation model proposed by Hua et al. [24].

In this chapter, we present a simple tube model for mixtures of linear polymers. This theory, valid in the linear regime only, proposes a coupled description of reptation, contour-length fluctuations and constraint release. Reptation and contour-length fluctuations are accounted for through a position dependent diffusion mechanism proposed by Graham et al. [23], while thermal constraint release is introduced using an extension of a new differential formulation of double reptation [33]. Our theory allows one to compute directly the tube survival probability along the primitive path. Furthermore, the extension to the polydisperse case yields a perfectly linear mixing rule. Then we demonstrate the predictive capabilities of our approach on a large set of polystyrene samples. Finally, we show how it is possible to build a linear approximation of our theory that retains both the structure of the model and the physical meaning of the variables. The resulting model is therefore a fully linear model (linear equations and mixing rule) that can predict the linear viscoelastic properties of entangled linear polymers.

2.2 Tube theory for a monodisperse system

In this section we present a tube theory for entangled linear systems. We first consider the monodisperse case and then extend the theory to account for polydispersity.

Let s ($-1 \leq s \leq 1$) be a parametric coordinate along the primitive path of a polymer chain in a monodisperse environment. Let us define $P_\gamma^f(t,s)$ the probability for a tube segment with position s to survive between the arbitrary initial time 0 and time t. The superscript f denotes that we do account for contour-length fluctuations, while the parameter γ is representative of the effectiveness of constraint release. Two limiting cases are $P_0^f(t,s)$ and $P_\gamma(t,s)$. The quantity $P_0^f(t,s)$ is representative of a chain relaxing in a fixed network of entanglements where no constraint release occurs, while $P_\gamma(t,s)$ properly describes a very long chain where the length-fluctuations become negligible. Reptation theory [11; 12] suggests that the time evolution of $P_0^f(t,s)$ is governed by a diffusion operator along the coordinate s. This operator represents the diffusive motion of the chain inside its tube that yields the destruction/renewal of a tube segment that reaches the chain ends. Following Des Cloizeaux [31] and Graham [23], we consider that the effect of contour-length fluctuations can be accounted for through a position-dependent diffusion constant. The simplest form for the evolution of $P_0^f(t,s)$ is therefore [12]:

$$\frac{\partial}{\partial t}P_0^f = \frac{\partial}{\partial s}\left(\alpha_d^f(s)\frac{\partial}{\partial s}P_0^f\right), \tag{2.1}$$

$$P_0^f(t,-1) = 0, \tag{2.2}$$

$$P_0^f(t,1) = 0 \text{ for } t>0, \tag{2.3}$$

$$P_0^f(0,s) = 1 \text{ for } -1<s<1,$$

where Eqs. (2.2-2.3) come from the assumption that chain ends are fully relaxed.

As suggested in [23] we consider $\alpha_d^f(s)$ to be constant along the primitive path, except at the chain end in two regions of size proportional to $\sqrt{M/M_e}$, where M is the molecular weight of the polymeric chain and M_e is the molecular weight between entanglements. In those regions, where contour-length fluctuations allow for a faster renewal of the tube segments, the diffusion coefficient is proportional to the inverse of the quadratic distance to the chain end. As the molecular weight of the polymer increases, the influence of contour-length fluctuations becomes more and more negligible. In that limiting case, the reptation picture [11] tells us that the diffusion constant should scale like the inverse of the cube of the molecular weight of the polymer. The

full expression for $\alpha_d^f(s)$ becomes:

$$\alpha_d^f(s) = \frac{4}{K_d\pi^2M^3}\frac{{K_f}^2M_e}{M(1-s)^2} \text{ if } s > \left(1-K_f\sqrt{\frac{M_e}{M}}\right), \tag{2.4}$$

$$\frac{4}{K_d\pi^2M^3}\frac{{K_f}^2M_e}{M(1-s)^2} \text{ if } s < \left(K_f\sqrt{\frac{M_e}{M}}-1\right), \tag{2.5}$$

$$\frac{4}{K_d\pi^2M^3} \text{ otherwise,} \tag{2.6}$$

where K_d is a material parameter. The adjustable parameter K_f is close to unity and controls the depth of the contour-length fluctuations within the model. We do not claim any universal value for K_f and consider it as a parameter that has to be identified for each material. This is similar to the parameter $M^\star$ of Des Cloizeaux [32] that also controls fluctuations. Taking $K_f = 0$ actually suppresses the fluctuations as the diffusion constant becomes constant along the chain. In that special case, one recovers the simple reptation picture of Doi and Edwards [12].

At this point, it is worth noticing that the simple scaling we adopt for the width of the fluctuation zone cannot be valid for poorly entangled systems. When M is only a few times M_e, the reptation picture tends to break down as fluctuations become the dominant relaxation mechanism.

Finally we account for constraint release using the approach we developed in [33]. This is done by adding a local relaxation term to Eq. (2.1) representative of relaxation through constraint release. Following the double reptation picture, we postulate that the rate of constraint release is proportional to the rate of relaxation through reptation and contour-length fluctuations, and that constraint release events occur with the same probability on all unrelaxed segments. The first assumption translates the fact that constraint release is actually driven by the other relaxation mechanisms. The second one states that the probability for a segment to relax through constraint release does not depend on its position along the chain. At a given position along the primitive path, the rate of relaxation through constraint release must therefore be proportional to the local tube survival probability. The resulting differential problem for $P_\gamma^f(t,s)$ reads:

$$\begin{aligned}
\frac{\partial P_\gamma^f}{\partial t} &= \frac{\partial}{\partial s}\left(\alpha_d^f(s)\frac{\partial}{\partial s}P_\gamma^f\right)+\beta P_\gamma^f, \qquad (2.7)\\
P_\gamma^f(t,-1) &= 0,\\
P_\gamma^f(t,1) &= 0 \text{ for } t>0,\\
P_\gamma^f(0,s) &= 1 \text{ for } -1<s<1,
\end{aligned}$$

where β is the rate of thermal constraint release. We now extend the expression for β proposed in [33] to account for both reptation and contour-length fluctuations:

$$\beta = \gamma \frac{\int_{-1}^{1} \frac{\partial}{\partial s}\left(\alpha_d^f(s)\frac{\partial}{\partial s}P_\gamma^f\right) \mathrm{d}s}{\int_{-1}^{1} P_\gamma \, \mathrm{d}s} \,, \tag{2.8}$$

where γ is an adjustable parameter of order unity that controls the amount of constraint release in the system. It is important to notice that β is not constant in time and therefore the local relaxation does not obey a simple first-order decay.

The relaxation modulus $G(t)$ is simply defined as being proportional to the average tube survival probability along the chain:

$$G(t) = G_N^0 \frac{1}{2} \int_{-1}^{1} P_\gamma^f(t,s) \, \mathrm{d}s \,, \tag{2.9}$$

G_N^0 being the plateau modulus.

In order to predict the high frequency response, the expression (2.9) for the relaxation modulus has to be modified to account for the Rouse modes of the chain. In practice, this is simply done by superposing a Rouse relaxation modulus $G_r(t)$ on the relaxation modulus coming from reptation. Following [15], the expression for the Rouse relaxation modulus for a chain of mass M writes:

$$G_r(t) = G_N^0 \left(\sum_{p=Z+1}^{\infty} \frac{1}{Z} \exp\left(-\frac{p^2}{\tau_r}\right) + \frac{1}{3} \sum_{p=1}^{Z} \frac{1}{Z} \exp\left(-\frac{p^2}{\tau_r}\right) \right) \,, \tag{2.10}$$

where $\tau_r = K_r M^2$ and K_r is an additional linear material parameter. The integer Z is defined as the closest integer to the ratio M/M_e. Although K_d, K_r, M and M_e are linked through the underlying segmental dynamics and should not be specified independently, they are considered as independent parameters in this chapter. In chapter 4, we make use of the relations summarized in [34] to reduce the number of independent linear parameters.

2.3 Extension to the polydisperse case

We now extend the theory presented in the previous section to the polydisperse case, without adding any adjustable parameter. The extension procedure is similar to the we proposed in [33], where contour-length fluctuations were neglected. Let us consider a polydisperse system of polymers with N different masses $M^{(i)}$. Let $P_\gamma^{f\,(i)}(t,s)$ be the

tube survival probability at time t and parametric position s for the chains of mass $M^{(i)}$. We assume that all chains reptate and fluctuate independently of the polydispersity of the system. The rate of constraint release is however the same for all chains and is computed from the relaxation of all masses. The differential problem governing the evolution of $P_\gamma^{f\,(i)}$ reads:

$$\begin{aligned}
\frac{\partial P_\gamma^{f\,(i)}}{\partial t} &= \frac{\partial}{\partial s}\left(\alpha_d^{f\,(i)}(s)\frac{\partial}{\partial s}P_\gamma^{f\,(i)}\right)+\beta P_\gamma^{f\,(i)}\,, \qquad (2.11)\\
P_\gamma^{f\,(i)}(t,-1) &= 0\,,\\
P_\gamma^{f\,(i)}(t,1) &= 0 \text{ for } t>0\,,\\
P_\gamma^{f\,(i)}(0,s) &= 1 \text{ for } -1<s<1\,.
\end{aligned}$$

In view of Eq. (2.8), the rate of constraint release β is consistently defined as:

$$\beta = \gamma\frac{\sum_i \phi^{(i)}\int_{-1}^{1}\frac{\partial}{\partial s}\left(\alpha_d^{f\,(i)}(s)\frac{\partial}{\partial s}P_\gamma^{f\,(i)}\right)\,\mathrm{d}s}{\sum_i \phi^{(i)}\int_{-1}^{1}P_\gamma^{f\,(i)}\,ds}\,, \qquad (2.12)$$

where $\phi^{(i)}$ is the volume fraction of species (i) and γ keeps the same meaning as in the monodisperse case. The diffusion coefficient $\alpha_d^{f\,(i)}(s)$ is computed from Eq. (2.4), where $M^{(i)}$ is substituted for M. Similarly to Eq. (2.9), we define the relaxation modulus as the volume average over the different species of the tube survival probability:

$$G(t) = G_N^0\sum_{i=1}^{N}\frac{\phi^{(i)}}{2}\int_{-1}^{1}P_\gamma^{f\,(i)}(t,s)\,\mathrm{d}s\,. \qquad (2.13)$$

By directly computing the relevant quantity i.e. the tube survival probability under reptation, contour-length fluctuations and thermal constraint release, we alleviate the need for a non-linear mixing rule.
In order to correctly model the short-time behaviour, the Rouse relaxation modulus (2.10) can be added for each species using a linear mixing rule.

2.4 Numerical solution of the model

Although the above theory is quite simple from a mathematical point of view, a closer look at Eq. (2.11) shows that the differential problems for all masses are coupled through the constraint release term. This in numerically expensive for a large number of masses. The numerical cost can however be reduced dramatically through the use of a semi-analytical solution that decouples the different masses.

In the absence of constraint release, i.e. when $\gamma = 0$, the partial differential equations (2.11) become decoupled. The functions $P_0^{f\,(i)}(t,s)$ can therefore be computed numerically at a reasonable cost using a finite difference scheme. Through direct substitution, one can verify that the following expression for $P_\gamma^{f\,(i)}(t,s)$ satisfies Eq. (2.11):

$$P_\gamma^{f\,(i)}(t,s) = P_0^{f\,(i)}(t,s)\left(\sum_{i=1}^{N}\frac{\phi^{(i)}}{2}\int_{-1}^{1}P_0^{f\,(i)}(t,s)\,\mathrm{d}s\right)^{\gamma}. \tag{2.14}$$

The computation of $P_\gamma^{f\,(i)}$ with this method has a truly negligible numerical cost as, for a large number of masses, the algorithmic complexity is reduced from quadratic to linear in N.

2.5 Model predictions

We now present predictions of the model in the monodisperse case. Next, we apply the model for the prediction of linear viscoelastic moduli of different samples of polydisperse polystyrene melts. For all predictions, a Rouse spectrum described by Eq. (2.10) has been superposed using a linear mixing rule.

In Fig. 2.1, we show the molecular weight dependence of the zero-shear viscosity of a monodisperse system. In the limit of highly entangled chains, the viscosity scales like the cube of the molecular mass. As the number of entanglements gets lower, this scaling gradually changes to an exponent 3.4. In this example we chose to set $\gamma = 1$ and $K_f = 0.6$. The value of the other parameters does not change the shape of the viscosity curve but merely translates it vertically and horizontally.

To evaluate the model, we test its ability to correctly predict the linear viscoelastic properties of six polydisperse polystyrene samples. The parameters of the model are estimated using the molecular weight distribution and the viscoelastic moduli of a single sample. The value of the parameters is then frozen for the subsequent predictions on the remaining five samples. The data of the six samples named PS1, PS2, PS3, PS60, PS275 and PS330 were kindly provided to us by BASF. We also received the molecular weight distribution and the viscoelastic moduli at 170 ℃from BASF. The characteristics of the various samples are provided in Table 2.5. Samples PS1, PS60 and PS275 are quite monodisperse, while PS2 and PS330 have a much broader molecular weight distribution. PS3 is a trimodal sample with a fraction of very high masses. The parameter estimation is actually quite a delicate task for two reasons. In the first place, the sensitivity of the model to the different parameters can be very uneven. Second, not all samples are suited to perform this estimation, if they only

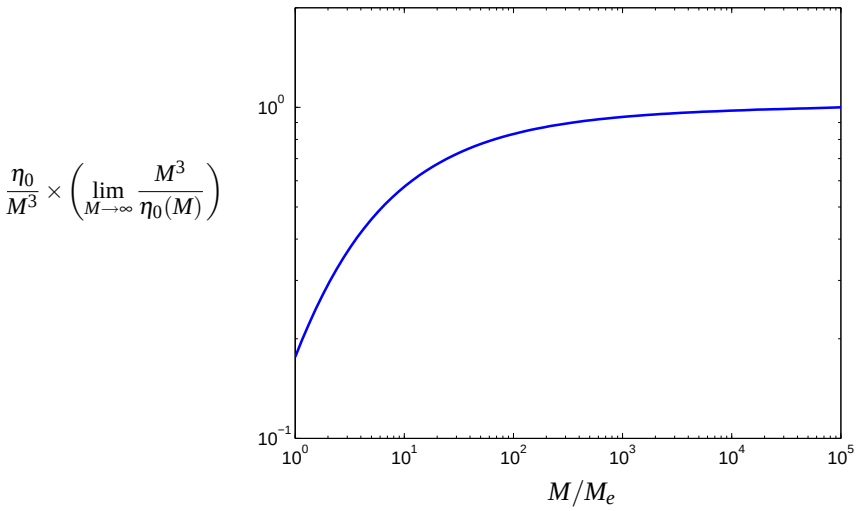

Figure 2.1: Dependence of the zero-shear viscosity η_0 with the molecular mass for a strictly monodisperse sample.

provide information in a narrow molecular weight range which is not representative of the physics built in the theory. Therefore, we chose to use the broad sample PS3 to fit the parameters of the model. In order to account for the whole molecular weight distribution, we discretize it with a small fixed step in logarithmic space. The efficient semi-analytical method described in Section 2.4 still allows us to compute quickly the model predictions. The parameters resulting from the fitting procedure are reported in Table 2.2. The molecular weight distribution as well as the measured and predicted viscoelastic moduli for PS3 are reported in Fig. 2.2(a,b). We see there a good quantitative agreement between the data and the predictions, over a wide range of frequencies.

Name	$M_w\,(\mathrm{kD})$	$M_n\,(\mathrm{kD})$	M_w/M_n
PS1	320	270	1.18
PS2	274	101	2.72
PS3	407	143	2.83
PS60	69.6	62.7	1.11
PS275	290	253	1.07
PS330	324	112	2.89

Table 2.1: Characteristics of the six PS samples provided by BASF.

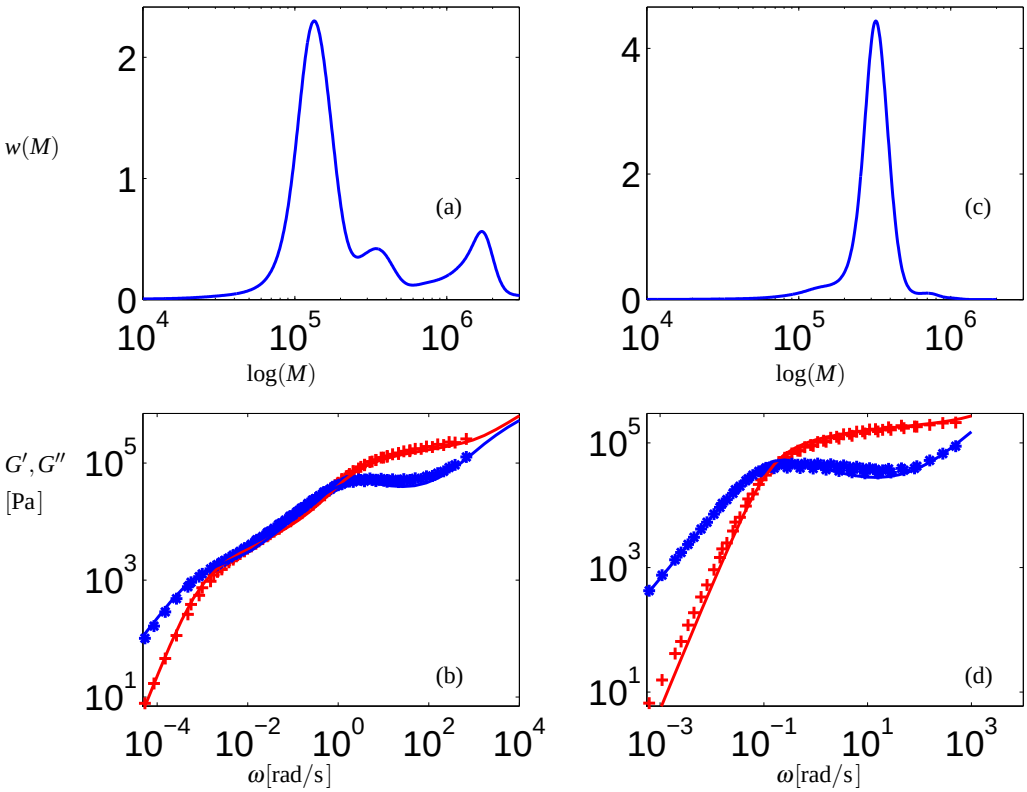

Figure 2.2: Molecular weight distribution and linear viscoelastic moduli of PS3 (a,b) and PS1 (c,d). Plain lines are the model's output, while the dots are the experimental data.

In Fig. 2.2 to 2.4 we show, for a wide range of molecular weight distributions, the quantitative agreement between experimentally measured viscoelastic moduli and the model's predictions. All these predictions were obtained using the single set of parameters from Table 2.2. The main discrepancies between predictions and measurements are found at low and high frequencies.
At low frequency, the model sometimes fails to correctly predict the storage modulus. In this frequency range the dominating mechanisms are reptation and constraint

G_N^0	K_d	K_r	K_f	γ
$2.1\,10^5$	$5.0\,10^{-16}$	$2.0\,10^{-12}$	0.6	1.15

Table 2.2: Parameters resulting from the fitting of the model on the PS3 data.

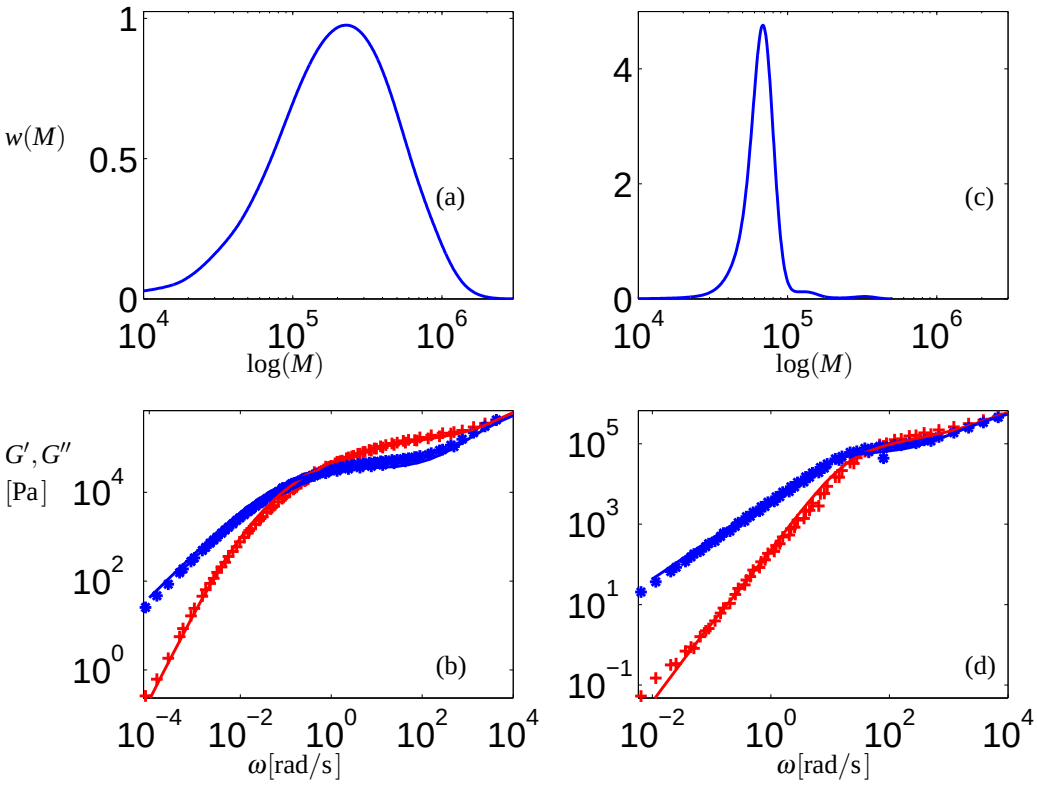

Figure 2.3: Molecular weight distribution and linear viscoelastic moduli of PS2 (a,b) and PS60 (c,d). Plain lines are the model's output, while the dots are the experimental data.

release. Furthermore, the parameter γ, which controls constraint release, has the main influence on the slope of the storage modulus in this region. We would therefore suggest that a more accurate treatment of constraint release would help resolve these discrepancies.

At intermediate and high frequencies the loss modulus tends to be underestimated. We connect this feature to the crude description of contour-length fluctuations we implemented.

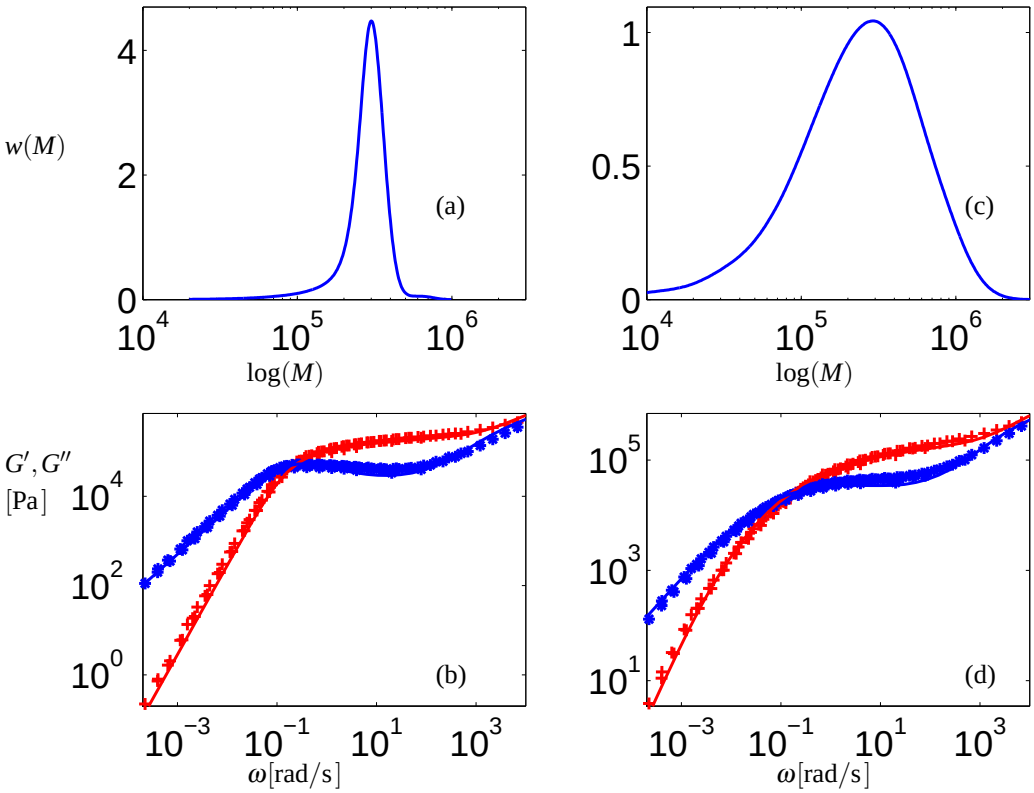

Figure 2.4: Molecular weight distribution and linear viscoelastic moduli of PS275 (a,b) and PS330 (c,d). Plain lines are the model's output, while the dots are the experimental data.

2.6 Linear approximation of the theory

Despite the relative simplicity of our theory, it remains non-linear due to the time dependence of the rate of constraint release β. This non-linearity is not a problem *per se* but having to rely on a non-linear theory to describe linear properties of a system prevents us from building a theory for the non-linear regime on top of the previous one. In the present section we propose a simple linear approximation of our theory that preserves its general mathematical structure.

The non-linearity of our theory comes from the time-dependent relaxation induced by constraint release. Therefore, we propose to approximate constraint release through a superposition of few linear modes. Let us call $Q_{CR}(t)$ or constraint release kernel the

second factor of the right-hand-side of Eq. (2.14). This factor represents the effects of constraint release on $P_0^{f\,(i)}(t,s)$:

$$Q_{CR}(t) = \left(\sum_{i=1}^{N} \frac{\phi^{(i)}}{2} \int_{-1}^{1} P_0^{f\,(i)}(t,s)\, \mathrm{d}s \right)^{\gamma} . \tag{2.15}$$

Let us assume that the constraint release kernel $Q_{CR}(t)$ can be approximated by a finite sum of decreasing time-exponentials:

$$Q_{CR}(t) \approx \sum_{j=0}^{N_{CR}} w_j \exp(-t/\tau_j) , \tag{2.16}$$

where w_j and τ_j are adjustable parameters. For a given of N, we compute w_j and τ_j using a minimisation procedure for the the quadratic error between the exact constraint release kernel (2.15) and its approximation (2.16). We can now define $P_\gamma^{f\,(i,j)}(t,s)$ as the solution of the following linear differential problem:

$$\begin{aligned}
\frac{\partial P_\gamma^{f\,(i,j)}}{\partial t} &= \frac{\partial}{\partial s}\left(\alpha_d^{f\,(i)}(s) \frac{\partial}{\partial s} P_\gamma^{f\,(i,j)} \right) - \frac{1}{\tau_j} P_\gamma^{f\,(i,j)} , \qquad (2.17)\\
P_\gamma^{f\,(i,j)}(t,-1) &= 0 ,\\
P_\gamma^{f\,(i,j)}(t,1) &= 0 \text{ for } t > 0 ,\\
P_\gamma^{f\,(i,j)}(0,s) &= 1 \text{ for } -1 < s < 1 .
\end{aligned}$$

As for Eq. (2.11), the analytical solution of Eq. (2.17) can be expressed as a function of $P_0^{f\,(i)}$:

$$P_\gamma^{f\,(i,j)}(t,s) = P_0^{f\,(i)}(t,s) \exp(-t/\tau_j) . \tag{2.18}$$

Making use of Eq. (2.16), one can verify that the following expression for the relaxation modulus correctly approximates Eq. (2.13) of the original theory:

$$G(t) = G_N^0 \sum_{i=0}^{N} \left(\frac{\phi^{(i)}}{2} \int_{-1}^{1} \left(\sum_{j=1}^{N_{CR}} P_\gamma^{f\,(i,j)}(t,s) \right) \mathrm{d}s \right) . \tag{2.19}$$

In the previous expression, the sub-expression contained within the innermost parenthesis actually is an approximation of $P_\gamma^{f\,(i)}(t,s)$. The quality of this linear approximation depends only on the quality of the approximation of the constraint release kernel (2.15) by a sum of decreasing exponentials. In Fig. (2.5) we show for sample PS2 that, with seven modes, the linear approximation is almost indistinguishable from the original model.

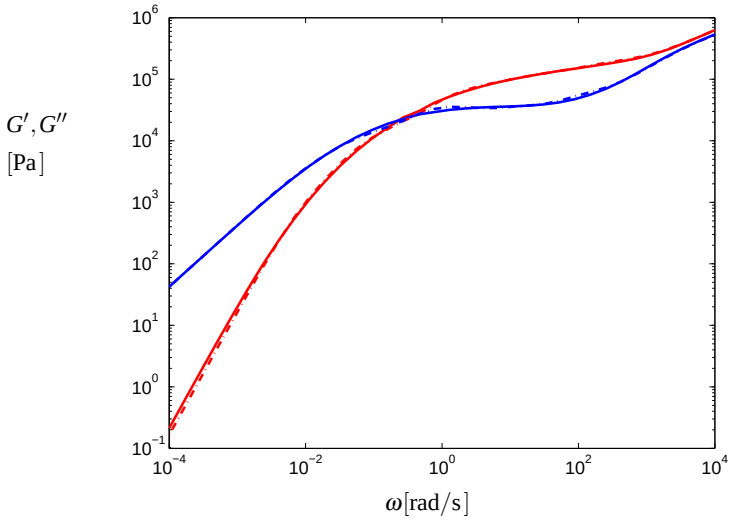

Figure 2.5: Comparison between the viscoelastic moduli of the full model (-) and its linear approximation(-.). Seven modes were used to approximate the constraint release kernel of the full model.

2.7 Conclusions

We have presented a simple tube theory for linear entangled systems. The specificity of this theory is that, for a monodisperse system, a single partial differential equation is used to compute the tube survival probability under reptation, contour-length fluctuations and thermal constraint release. Reptation and contour-length fluctuations are modelled simultaneously by position-dependent diffusion along the primitive path. Thermal constraint release is introduced through a time dependent relaxation term. The intensity of the thermal constraint release is controlled by reptation and contour-length fluctuations. In a polydisperse environment, we directly compute the tube survival probability under the influence of all masses with a set of coupled partial differential equations. Additionally, we proposed a semi-analytical method for the numerical solution of our model. This method reduces the algorithmic complexity from quadratic to linear in terms of the number of masses, thus making the computational cost negligible even for a broad molecular weight distribution.
Although some discrepancies remain, we have shown the good predictive properties of our theory on a wide range of molten polystyrene samples.
Finally, we have proposed a linear approximation of our theory, that enables us to address the linear viscoelastic properties of entangled linear polymers with a linear

theory. As shown in the next chapter, this approximation is suited as a starting point for building constitutive equations for the non-linear regime.

Chapter 3

A tube-based constitutive equation for polydisperse entangled linear polymers

3.1 Introduction

Following the introduction on the reptation picture by de Gennes [11], Doi and Edwards [12] proposed a first tube-based theory to explain the linear rheology of linear entangled polymers. Variations of the tube model have reached a very high level of maturity and are capable of a quantitative description of the linear viscoelastic properties of linear entangled polymers [15; 16; 17]. The key of these successes essentially is an accurate description of the reptation dynamics (if present), the fluctuations of the length of the tube and thermal constraint release phenomena, which is a closure to the tube mean field approach. Accounting for coupling between those effects is of critical importance. For linear polymers, the distinction made between reptation and contour-length fluctuations is somehow arbitrary as they represent different modes of the dynamics of a one-dimensional Rouse chain escaping a tube. This distinction is not found in stochastic tube theories where the full chain is modelled [24; 30; 16]. Contour-length fluctuations and reptation have been accounted for by using a modified diffusion process along the primitive path. In those theories, one either considers a time dependent [31] or a position dependent [32; 23; 35] diffusivity along the primitive path. Thermal constraint release is today well understood through dynamic dilution

[22] and Rouse motion of the tube. The complex interplay between those phenomena has been thoroughly investigated [25; 29]. Double reptation [4; 5] provides a simple and efficient method to account for constraint release. It essentially provides a reasonable approximation to Rouse tube motion, especially at early times [16]. The essence of Double reptation has actually been recovered within the implementation of constraint release found in a stochastic full chain reptation model developed by Hua and Schieber [24].

The development of theories for the non-linear response of entangled polymers is much more limited and even in the case of monodisperse linear chains, additional phenomena are still proposed as being important in the description of the flow properties of some systems [36]. The Doi-Edwards (D-E) model [12] was a first attempt to build a tube-based constitutive equation. Despite the many assumptions found within the D-E model, mostly for mathematical convenience, the predictions of the model are in very good agreement with experimental data for step deformations. For other types of flow the D-E model fails even in the prediction of qualitative features of the non-linear rheology of entangled systems. Among the failures of the D-E model, the most noticeable is the prediction of a shear banding instability in weakly non-linear flows which has never been observed in experiments. This instability is a direct consequence of the non-monotonic curve one can observe when the steady state shear stress is plotted versus the shear rate. Because reptation is the only relaxation mechanism of the D-E model, all tube segments become fully aligned in the shear direction when the shear rate $\dot{\gamma}$ is larger than the inverse reptation time $1/\tau_d$, which causes the decrease of the shear stress. The excessive shear thinning of the D-E model prevents it from being used in complex flow simulations without considering an additional Newtonian contribution to the viscosity.

In a first attempt to improve the theory, Marrucci and Grizzuti [37] proposed a constitutive model known as the Doi-Edwards-Marrucci-Grizzuti (DEMG) model which, unlike the original D-E theory, did not assume the instantaneous retraction of the chain inside the tube. This incorporation of tube stretching effects at a timescale τ_r, much smaller than the timescale τ_d of reptation, led to improved predictions of the transient response of the model. In particular, it showed overshoots in both shear stress and first normal stress difference upon startup of shear. Although the inclusion of stretch effects might smear out the shear instability of the D-E model for moderately entangled systems, this approach will inevitably fail as one increases the molecular mass M of the entangled species. Indeed, as the time scale of the one dimensional Rouse relaxation associated with stretch scales like M^2, an increase in M can render τ_r arbitrarily small with respect to τ_d which scales like M^3. For highly entangled species, the approximation of instantaneous chain retraction is therefore valid and cannot be held responsible for the shear banding instability of the D-E model.

Finally, in 1996, Marrucci [38] successfully pointed out constraint release as the key to overcome the problem. Although constraint release may be considered to play only a mild role in describing the linear viscoelastic behaviour of a monodisperse material, it has a much greater influence in the non-linear regime where constraint release events may not only be triggered by reptation but also by chain retraction. For flows where the deformation rate $\dot{\gamma}$ lies between $1/\tau_d$ and $1/\tau_r$ the rate of constraint release would then be proportional to $\dot{\gamma}$, which is the rate of retraction necessary to maintain the chain at its equilibrium length. This type of constraint release is called Convective Constraint Release (CCR) as, from the point of view of the chain, constraints are convected by the flow along the tube. The first attempts by Ianniruberto and co-workers [39] and Marrucci et al. [9] to incorporate CCR into a constitutive equation were focusing on flow regimes where $\dot{\gamma} \leq 1/\tau_r$ and assumed complete chain retraction. As the rate of CCR has then to be computed from the relative alignment of the microstructure with the flow field, it is difficult to obtain a general CCR formulation that does not rely on a switch function to turn CCR off when it would yield unrealistic predictions. The thermodynamical validity of such formulations of CCR for differential constitutive equations has been discussed by Leygue et al. [40].

More successful constitutive equations account explicitly for chain stretch and compute the rate of CCR directly from the rate of chain retraction. Using a very detailed integral model, Mead et al. [26] showed how CCR, combined with tube length fluctuations and stretch effects, could prevent the excessive shear thinning and solve other problems of the D-E model. Their approach however relied on a separate representation of the average stretch and orientation of the tube and still needed a switch function to balance CCR between the relaxation of stretch and orientation.

Recently, Marrucci and Ianniruberto [41] proposed a promising single segment model that incorporates both chain stretch and CCR in a coupled representation. This new model is simple enough to be easily used for complex flow simulations [42] but yet retains the necessary physics.

The construction of microstructural constitutive models for entangled systems is a process in which many mathematical approximations have to be made in order to obtain a closed set of partial differential equations. From this angle, stochastic models offer an attractive approach, where the mathematical complexity of the approximations is partially replaced by the numerical complexity and cost of stochastic differential equations. Based on microstructural mechanical models, successful full chain stochastic reptation models have been proposed by Hua et al. [24] and Masubuchi et al. [30]. These models are very useful to understand the influence of some physical effects but their numerical complexity still prevents them from being used in complex flow simulations.

In the present text, we present the CRAFT model; a new tube-based constitutive equation for entangled linear polymers. We first recall a simple linear theory for the prediction of the linear viscoelastic properties of polydisperse systems [35]. Then, we extend this theory to a full constitutive equation for entangled linear polymers. This constitutive model incorporates, in a full chain approach, the major molecular mechanisms thought to be important to describe the flow of entangled polymers: reptation, contour-length fluctuations, thermal and convective constraint release, chain stretch and finite extensibility of the polymeric chains. The central point of this new model is that thermal and convective constraint release are modeled in a unified fashion where the latter appears as a nonlinear addition to the former. Additionally, the linearization of our model is equivalent to the original linear theory. Most of the parameters of the constitutive model can therefore be identified and understood from the linear viscoelastic response. For polydisperse systems, constraint release actually provides the mixing rule in both the linear and nonlinear regimes, with no additional parameter. The acronym CRAFT stands for Constraint Release on Average Full Tensorial chain, the main feature of our model is its implementation of constraint release, on a tensorial representation of the averaged primitive chains. Finally, we analyse the predictions of the CRAFT constitutive equation and compare them with recently published experimental data for concentrated polystyrene solutions in various rheometrical flows.

3.2 A linear model for linear entangled polymers

Most of today's quantitative theories [17; 14; 13; 15; 16; 21] that predict the relaxation modulus as a function of the molecular weight distribution and a few material parameters are mathematically non-linear. This feature does not allow for their direct extension to a full constitutive equation for predicting the non-linear rheology. Starting from a mathematically linear model for predicting the linear viscoelasticity of linear polymers [35], we build the CRAFT constitutive equation as a non-linear extension. As non-linear relaxation phenomena are incorporated into the constitutive equation we always require that they do not change its linear response. The model is therefore able to describe both the linear and non-linear rheology of entangled systems. In this section, we briefly recall the simple linear model in the polydisperse case.

In a polydisperse mixture of entangled linear polymers, let us consider the chains of a given mass $M^{(i)}$ among the N masses. Let s be a curvilinear coordinate along the primitive path. For simplicity, all lengths are made non-dimensional with respect to half the equilibrium length of the primitive path. Therefore we have $-1 \leq s \leq 1$. We then define $P_\gamma^{f\,(i)}(t,s)$ as the probability for a chain segment of coordinate s of being in a tube segment that is older than t. This tube survival probability decreases

in time under the combined effects of reptation, contour-length fluctuations and thermal constraint release. Although the spectrum of relaxation times due to reptation and contour-length fluctuations is relatively narrow for a given mass, a polydisperse environment will yield a broad spectrum of relaxation times for $P_\gamma^{f\,(i)}(t,s)$. The tube survival probability is therefore approximated by a sum of modes corresponding to the dominant relaxation times induced by thermal constraint release:

$$P_\gamma^{f\,(i)}(t,s) \approx \sum_{j=1}^{N_{CR}} w_j P_\gamma^{f\,(i,j)}(t,s)\ , \tag{3.1}$$

where N_{CR} is representative of the number of characteristic relaxation times τ_j induced by thermal constraint release and w_j represent the relative weights of those times. This description in terms of modes of constraint release implies that, for a fixed (i), the contribution of reptation and contour-length fluctuations to the dynamics of $P_\gamma^{f\,(i,j)}(t,s)$ is identical for all (j).

Let us now focus on the dynamics of $P_\gamma^{f\,(i,j)}(t,s)$. Following [23], reptation and fluctuations are modelled together by a diffusion operator with a variable diffusivity along the coordinate s. Additionally, thermal constraint release is introduced through a linear relaxation term with a characteristic time τ_j. The resulting differential problem for $P_\gamma^{f\,(i,j)}(t,s)$ reads:

$$\begin{aligned}
\frac{\partial P_\gamma^{f\,(i,j)}}{\partial t} &= \frac{\partial}{\partial s}\left(\alpha_d^{f\,(i)}(s)\frac{\partial}{\partial s}P_\gamma^{f\,(i,j)}\right) - \frac{1}{\tau_j}P_\gamma^{f\,(i,j)}\ , \qquad (3.2)\\
P_\gamma^{f\,(i,j)}(t,-1) &= 0\ ,\\
P_\gamma^{f\,(i,j)}(t,1) &= 0 \text{ for } t>0\ ,\\
P_\gamma^{f\,(i,j)}(0,s) &= 1 \text{ for } -1<s<1\ .
\end{aligned}$$

Contour-length fluctuations are assumed to modify the diffusion coefficient $\alpha_d^{f\,(i)}(s)$ up to a depth of order $\sqrt{M^{(i)}/M_e}$, where M_e is the entanglement molecular weight. The expression for $\alpha_d^{f\,(i)}(s)$ reads:

$$\alpha_d^{f\,(i)}(s) = \frac{4}{K_d\pi^2{M^{(i)}}^3}\frac{{K_f}^2M_e}{M^{(i)}\left(1-s\right)^2} \text{ if } s>\left(1-K_f\sqrt{\frac{M_e}{M^{(i)}}}\right) \tag{3.3}$$

$$\frac{4}{K_d\pi^2{M^{(i)}}^3}\frac{{K_f}^2M_e}{M^{(i)}\left(1-s\right)^2} \text{ if } s<\left(K_f\sqrt{\frac{M_e}{M^{(i)}}}-1\right) \tag{3.4}$$

$$\frac{4}{K_d\pi^2{M^{(i)}}^3} \text{ otherwise,} \tag{3.5}$$

where K_d is a material parameter. The adjustable parameter K_f is close to unity and controls the depth of the contour-length fluctuations within the model.

The relaxation times τ_j, induced by thermal constraint release, and their associated weights w_j are such that they yield a constraint release kernel as close as possible to the constraint release kernel that double reptation would induce:

$$\sum_{j=0}^{N_{CR}} w_j \exp(-t/\tau_j) \approx \left(\sum_{i=1}^{N} \frac{\phi^{(i)}}{2} \int_{-1}^{1} P_0^{f\,(i)}(t,s)\,\mathrm{d}s \right)^{\gamma} . \tag{3.6}$$

The parameter γ is a mixing exponent of order unity and the functions $P_0^{f\,(i)}(t,s)$ are the tube survival probabilities with thermal constraint release neglected. They are computed from the following differential problem:

$$\begin{aligned} \frac{\partial}{\partial t} P_0^{f\,(i)} &= \frac{\partial}{\partial s} \left(\alpha_d^{f\,(i)}(s) \frac{\partial}{\partial s} P_0^{f\,(i)} \right) , \\ P_0^{f\,(i)}(t,-1) &= 0 , \\ P_0^{f\,(i)}(t,1) &= 0 \text{ for } t > 0 , \\ P_0^{f\,(i)}(0,s) &= 1 \text{ for } -1 < s < 1 . \end{aligned} \tag{3.7}$$

The relaxation modulus is proportional to the average tube survival probability over all masses:

$$G(t) = G_N^0 \sum_{i=1}^{N} \sum_{j=1}^{N_{CR}} \phi^{(i)} w_j \frac{1}{2} \int_{-1}^{1} P_\gamma^{f\,(i,j)}(t,s)\,\mathrm{d}s , \tag{3.8}$$

where G_N^0 is the plateau modulus, and $\phi^{(i)}$ is the volume fraction of mass $M^{(i)}$. In order to make quantitative predictions of the linear viscoelastic moduli at high frequencies, one should also account for the Rouse relaxation modes of the chains. The Rouse relaxation time τ_r of an unentangled chain is given by:

$$\tau_r = K_r M^2 , \tag{3.9}$$

where K_r is a linear material parameter. Following van Ruymbeke et al. [15], the Rouse spectrum $G_r(t)$ for that entangled chain writes:

$$G_r(t) = G_N^0 \left(\sum_{p=Z+1}^{\infty} \frac{1}{Z} \exp\left(-\frac{p^2}{\tau_r} \right) + \frac{1}{3} \sum_{p=1}^{Z} \frac{1}{Z} \exp\left(-\frac{p^2}{\tau_r} \right) \right) . \tag{3.10}$$

The integer Z is defined as the closest integer to the ratio M/M_e. The Rouse modulus of each mass $M^{(i)}$ is to be superposed to the reptation relaxation modulus using a linear

mixing rule.
Although K_d, K_r, M and M_e are linked through the underlying segmental dynamics and should not be specified independently, they are considered as independent parameters in this chapter.

The set of equations presented in this section is closed and forms a mathematically linear model that can predict quantitatively the linear viscoelastic response of entangled linear polymers. In the following sections, we will extend this model to a full constitutive equations for non-linear flow regimes.

3.3 Construction of the CRAFT constitutive equation

For the sake of simplicity we will present the construction of the CRAFT model for the monodisperse case only and for only one characteristic time of thermal constraint release. This simplification allows us to discard the (i, j) superscripts we had to consider in the previous section. The polydisperse case with a full thermal constraint release spectrum will be presented as a natural extension in a latter section.

The variables of the CRAFT model are the components of a second order conformation tensor $\mathbf{c}(t,s)$ defined along the coordinate s of the primitive path. The dynamics of this tensor are controlled by a PDE which accounts for the following phenomena:

- affine deformation of the micro-structure,
- reptation of the primitive chain,
- contour-length fluctuations,
- relaxation of tube stretch,
- thermal and convective constraint release,
- finite extensibility of the polymeric chain.

In the next sections, we will first define some additional notations and then consider the contribution of each phenomenon to the evolution of $\mathbf{c}(t,s)$.

3.3.1 Variables and notations

Let us consider a single polymeric chain, trapped in a fixed tube, as shown in Fig. 3.1. Both the primitive chain and the tube exist in real space (3-D), but can be referenced through a single parametric coordinate s. For simplicity, all lengths in real space are made non-dimensional with respect to half of the equilibrium length of the primitive path. At equilibrium, the non-dimensional length of the primitive path is therefore 2.

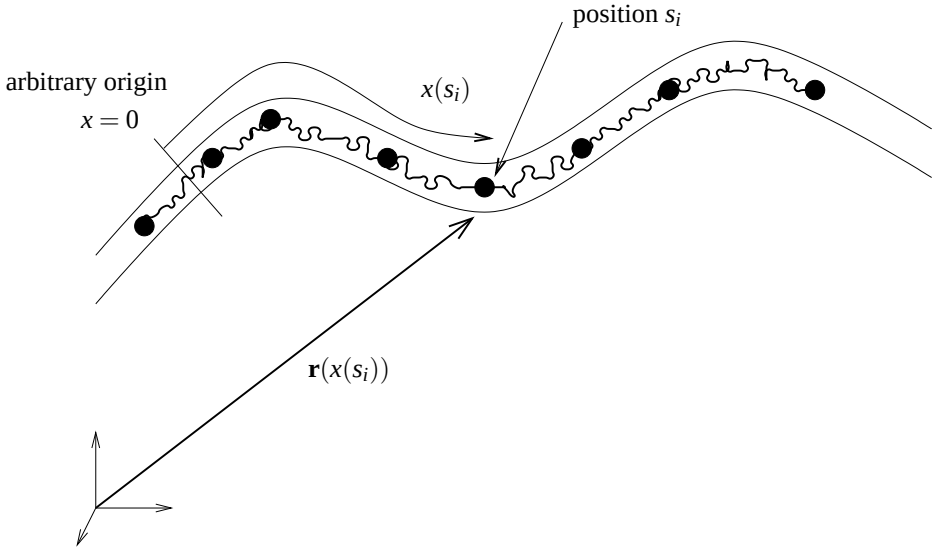

Figure 3.1: Illustration of the notations used to build the CRAFT model.

Let $x(t,s)$ be the position of the primitive chain along the tube, where s ($-1 \leq s \leq 1$) is a Lagrangian coordinate along the chain. At equilibrium, s is a curvilinear coordinate which implies that $(x-s)$ is a constant. The position of the origin $x = 0$ is actually arbitrary. The position of the tube in real space is defined by the vector $\mathbf{r}(x)$, and by definition of x and $\mathbf{r}$ we have:

$$\left\| \frac{\partial \mathbf{r}}{\partial x} \right\| = 1 \, . \tag{3.11}$$

For a system composed of many chains, let us define the second-order conformation tensor $\mathbf{c}(t,s)$ as:

$$\mathbf{c}(t,s) = 3 \left\langle \frac{\partial \mathbf{r}}{\partial s} \frac{\partial \mathbf{r}}{\partial s} \right\rangle \, , \tag{3.12}$$

where $\langle\cdot\rangle$ is the statistical ensemble average over all chains. This definition of $\mathbf{c}$ yields:

$$\mathrm{tr}\,\mathbf{c} = 3\left\langle \left(\frac{\partial x}{\partial s}\right)^2 \right\rangle , \tag{3.13}$$

which is the average local stretch along the primitive path. We now have to propose an evolution equation for the set of tensors $\mathbf{c}(t,s)$ as well as a way to compute the stress tensor.

3.3.2 Affine deformation

We decide to couple the dynamics $\mathbf{c}(t,s)$ to the velocity field with the assumption of affine deformation of the micro-structure. The induced strain measure is therefore the classical affine strain measure. At the microstructural level, this yields the following evolution equation for the tangent vector $\frac{\partial \mathbf{r}}{\partial s}$:

$$\frac{D}{Dt}\frac{\partial \mathbf{r}}{\partial s} = \boldsymbol{\kappa}\cdot\frac{\partial \mathbf{r}}{\partial s} , \tag{3.14}$$

where $\boldsymbol{\kappa}$ is the velocity gradient. Through direct substitution of Eq. (3.14) in Eq. (3.12), we find the following evolution equation for $\mathbf{c}(t,s)$:

$$\frac{D\mathbf{c}}{Dt}(t,s) = \boldsymbol{\kappa}\cdot\mathbf{c} + \mathbf{c}\cdot\boldsymbol{\kappa}^T , \tag{3.15}$$

or

$$\overset{\triangledown}{\mathbf{c}}\,(t,s) = 0 . \tag{3.16}$$

When all relaxation phenomena can be neglected (e.g. in a step deformation) the evolution of $\mathbf{c}(t,s)$ is governed by the upper convected time derivative and $\mathbf{c}(t,s)$ is therefore equal to the Finger strain tensor.

3.3.3 Reptation and fluctuations dynamics

To incorporate reptation within the model, we postulate that the dissipative dynamics of reptation is governed by the same operator that governs the relaxation of $P_\gamma^f(t,s)$:

$$\frac{\partial}{\partial s}\left(\alpha_d(s)\frac{\partial \cdot}{\partial s}\right) . \tag{3.17}$$

Through this differential operator, we explicitly take into account the connectivity of the chain and the physical process of reptation. Hence, we build a full chain model

rather than a single segment model. As reptation is a diffusion process in real space which we solve in parametric space s, the onset of chain stretch should be accounted for in the change of variable from x to s. To ensure a constant rate of diffusion in real space, Graham et al. [23] modify the diffusion operator as the stretch increases. We do agree with the physics and the mathematics behind this proposal, but we choose not to incorporate it in our model. The reason is twofold. In the first place, Marrucci has showed [38] that Convective Constraint Release (CCR) becomes the dominant relaxation mechanism as soon as the rate of deformation is greater than the inverse reptation time. As the stretch relaxation time is smaller than the reptation time, this occurs even before the onset on chain stretch. The renormalisation of the diffusion operator due to chain stretch will therefore be significant for flow regimes where reptation has already been superseded by CCR. Second, we believe that even before the onset of chain stretch, anisotropy effects within the entangled network are likely to appear and modify the diffusion process in a more significant way.

At the chain ends, we assume that the primitive chain is always fully relaxed in both stretch and orientation. For $s = \pm 1$, the vectors $\dfrac{\partial \mathbf{r}}{\partial s}$ are therefore uniformly distributed on the unit sphere, which yields:

$$\mathbf{c}(t, \pm 1) = \delta \; . \tag{3.18}$$

The validity of this assumption can be questioned as it implies that no matter the strength of the flow, the chain ends will always be fully relaxed. Ignoring anisotropy effects, we can nevertheless assume that this assumption is valid for flow rates up to the inverse of the segmental time τ_e.

3.3.4 Chain stretch dynamics

In this section, we address the problem of describing the relaxation of chain stretch and its coupling with orientation.

Let us model the retraction of the chain as due to a one-dimensional Rouse motion of the chain inside the tube. The projection along the primitive path of the microscopic force balance at position s yields the following evolution equation for $x(t,s)$:

$$\frac{\partial x}{\partial t} = \alpha_r \frac{\partial^2 x}{\partial s^2} \; , \tag{3.19}$$

$$\frac{\partial}{\partial s} x(t, \pm 1) = 1 \; , \tag{3.20}$$

where s is the Lagrangian coordinate along the chain, $x(t,s)$ is the curvilinear position for the chain along the tube and α_r is a characteristic diffusion constant, scaling like

the inverse of the square of the molecular mass. Eq. (3.20) is a boundary condition expressing that chain ends are always fully relaxed in stretch. The steady state solution of (3.19) is linear in s and the equilibrium length of the chain is 2.

Under the assumption that the tube is a fixed object, i.e. reptation phenomena are slow compared to the relaxation of stretch along the primitive path, we would like to find the contribution of the chain dynamics (3.19) to the evolution of $\mathbf{c}$. Considering the definition of $\mathbf{c}$, let us first try to obtain a tractable expression for the following quantity:

$$\frac{\partial}{\partial t}\left(\frac{\partial \mathbf{r}(x(t,s))}{\partial s}\frac{\partial \mathbf{r}(x(t,s))}{\partial s}\right) . \tag{3.21}$$

From (3.19), applying chain differentiation we can approximate (3.21) as:

$$\frac{\partial}{\partial t}\left(\frac{\partial \mathbf{r}}{\partial s}\frac{\partial \mathbf{r}}{\partial s}\right) \approx \frac{\alpha_r}{2}\frac{\partial}{\partial s}\left(\frac{\partial x}{\partial s}\right)^2 \frac{\partial}{\partial s}\left(\frac{\partial \mathbf{r}}{\partial x}\frac{\partial \mathbf{r}}{\partial x}\right) + \alpha_r\left(\frac{\partial \mathbf{r}}{\partial x}\frac{\partial \mathbf{r}}{\partial x}\right)\frac{\partial^2}{\partial s^2}\left(\frac{\partial x}{\partial s}\right)^2 . \tag{3.22}$$

The only approximation made to obtain the previous expression is:

$$\begin{aligned}\frac{\partial^2}{\partial s^2}\left(\frac{\partial x}{\partial s}\right)^2 &= 2\frac{\partial x}{\partial s}\frac{\partial^2 x}{\partial s^2}\frac{\partial x}{\partial s} + 2\left(\frac{\partial^2 x}{\partial s^2}\right)^2 \\ &\approx 2\frac{\partial x}{\partial s}\frac{\partial^2 x}{\partial s^2}\frac{\partial x}{\partial s} .\end{aligned}$$

The purpose of this approximation is to obtain a closed form for the evolution equation of $\left(\frac{\partial \mathbf{r}}{\partial s}\frac{\partial \mathbf{r}}{\partial s}\right)$. The term which is neglected is the square of a curvature term and the approximation can therefore be interpreted as a mild curvature assumption. The validity of this approximation has been successfully tested for a single chain relaxing in a tube after a step strain in shear or extension [43].

To go from the relaxation of a single chain to the relaxation of $\mathbf{c}$, we need to average (3.22) over the ensemble of chains. In this process, we approximate the average of products/ratios by the products/ratios of the averaged quantities. These closure approximations are required in order to obtain a closed set of equations for the averaged stretch dynamics. The resulting evolution equation for $\mathbf{c}$ is the following:

$$\frac{\partial \mathbf{c}}{\partial t} = \frac{\alpha_r}{2}\frac{\partial \mathrm{tr}\,\mathbf{c}}{\partial s}\frac{\partial}{\partial s}\frac{\mathbf{c}}{\mathrm{tr}\,\mathbf{c}} + \alpha_r\frac{\mathbf{c}}{\mathrm{tr}\,\mathbf{c}}\frac{\partial^2 \mathrm{tr}\,\mathbf{c}}{\partial s^2} . \tag{3.23}$$

As taking the trace of the previous expression makes the first term of the right-hand side disappear, we see that the second term alone governs the relaxation of stretch along the chain. More specifically, stretch relaxes through a diffusion process with a

time scale of order $\frac{1}{\alpha_r}$. This term also couples the relaxation of the diagonal and non-diagonal components of $\mathbf{c}$ in such a way that it does not modify the purely orientational part: $\frac{\mathbf{c}}{\mathrm{tr}\,\mathbf{c}}$. Indeed, if $\frac{\partial \mathbf{c}}{\partial t} = \alpha_r \frac{\mathbf{c}}{\mathrm{tr}\,\mathbf{c}} \frac{\partial^2 \mathrm{tr}\,\mathbf{c}}{\partial s^2}$ then $\frac{\partial}{\partial t}\left(\frac{\mathbf{c}}{\mathrm{tr}\,\mathbf{c}}\right) = 0$.

The first term on the right-hand side of (3.23) influences the local orientation only. It can be interpreted as a transport term along the s coordinate, wherein the velocity is proportional to the stretch gradient and the transported quantity is purely orientational: $\frac{\mathbf{c}}{\mathrm{tr}\,\mathbf{c}}$. As chain retraction occurs, it slows down the overall relaxation as the orientation of the chain is transfered from the inner segments to the outer, and more relaxed, segments.

In view of the many approximations needed to obtain Eq. (3.23), one might rely on the bracket formalism of non-equilibrium thermodynamics [44] to obtain an alternative phenomenological expression for the evolution of $\mathbf{c}$ induced by the chain stretch dynamics. The form of Eq. (3.23) provides however a guide to build the appropriate dissipation bracket. A simple expression for the dissipation bracket [45] yields the following expression:

$$\frac{\partial \mathbf{c}}{\partial t} = \alpha_r \mathbf{c} \frac{\partial}{\partial s} \frac{1}{\mathrm{tr}\,\mathbf{c}} \frac{\partial \mathrm{tr}\,\mathbf{c}}{\partial s} + \alpha_r \frac{\mathbf{c}}{\mathrm{tr}\,\mathbf{c}} \frac{\partial^2 \mathrm{tr}\,\mathbf{c}}{\partial s^2} \,. \tag{3.24}$$

This expression is very close to Eq. (3.23) and is compatible with the bracket formalism of non-equilibrium thermodynamics. Future work should focus on its evaluation and its comparison with Eq. (3.23) in different flow regimes.

3.3.5 Constraint Release

Generalising our approach of thermal constraint release from section (3.2), we assume it is possible to model both thermal and convective constraint release phenomena as a local relaxation process where the rate of relaxation due to CCR is computed from the dynamics of stretch relaxation. Furthermore, we assume that thermal and convective constraint release are independent allowing us to sum their rates.

The procedure to compute the rate of thermal constraint release has been detailed in section 3.2. For the sake of clarity, we will assume here that thermal constraint release can be described with a single relaxation time τ_{cr}. The remaining issue is therefore to give a valid expression of the rate of constraint release f_{ccr} under the following constraints:

- As the constitutive equation must be applicable in any type of flow and in any coordinate system, only the invariants of $\mathbf{c}$ can be used for expressing f_{ccr}.
- The velocity gradient cannot be used explicitly for computing f_{ccr} without special attention. From a thermodynamical point of view, this would bring an additional coupling between the velocity and the variables describing the microstructure, which has to be accounted for in the stress tensor [44]. Furthermore, such a coupling might lead to a negative rate of entropy production in some flows and a switch function is therefore needed to prevent this [40].
- In the linear regime, the expression for f_{ccr} must vanish.
- In the non-linear regime, f_{ccr} should account for CCR. Its value has then to governed by stretch relaxation.

A first possibility to compute the rate of CCR would be to follow Mead et al. [26] and simply take the rate of convection of mesh of entanglements, relative to the rate at which the chain is stretched. Neglecting some pre-factors of order unity, this would yield the following expression:

$$f_{\text{ccr}}(t) = -\frac{\displaystyle\int_{-1}^{1} \alpha_r \frac{\partial^2}{\partial s^2} \operatorname{tr}\mathbf{c}(t,s)\,\mathrm{d}s}{\displaystyle\int_{-1}^{1} \operatorname{tr}\mathbf{c}(t,s)\,\mathrm{d}s}\,. \tag{3.25}$$

Although this expression is quite appealing, it can lead to negative rates of CCR in some reversing flows such as Large Amplitude Oscillatory Shear (LAOS) flows. For well entangled systems, the reptation time τ_d and stretch relaxation time τ_r can be well separated. If the characteristic time of the LAOS flow ν^{-1} is such that $\tau_r << \nu^{-1} << \tau_d$, the microstructure can be fully oriented but not stretched at all when the maximum strain is reached. When the flow starts to reverse, the flow kinematics will tend to compress the chains below their equilibrium length. The stretch relaxation processes will therefore tend to increase the length of the chains to preserve their length, leading to a negative value for $f_{\text{ccr}}(t)$. Therefore we propose the following more general expression for the rate of CCR:

$$f_{\text{ccr}}(t) = -\frac{\displaystyle\int_{-1}^{1} \frac{D}{Dt} a(\mathbf{c}(t,s))\Big|_{\text{stretch}}\,\mathrm{d}s}{\displaystyle\int_{-1}^{1} a(\mathbf{c}(t,s))\,\mathrm{d}s}\,, \tag{3.26}$$

where $a(\mathbf{c}(s))$ is the contribution from the chain segments with position s to the local free energy density. The notation $\frac{D\cdot}{Dt}\big|_{\text{stretch}}$ represents the Lagrangian variation of a

quantity due to the relaxation of stretch. Under the hypothesis that sub-chains are Gaussian, $a(\mathbf{c})$ takes the form [44]:

$$a(\mathbf{c}) = G_N^0 \left(\mathrm{tr}\,(\mathbf{c}) - \ln \det(\mathbf{c})\right) , \tag{3.27}$$

which is the free energy one would use if $\mathbf{c}$ was describing Hookean dumbbells. Finite extensibility issues have also been neglected in the definition of $a(\mathbf{c})$. In the next section, when finite extensibility will be taken into account, we will use the free energy corresponding to FENE-P dumbbells. In appendix 3.10, we show that Eq. (3.26) always yields a positive rate of constraint release. Except for reversing flows where the flow might tend to compress the polymeric coils, the first term of Eq. (3.27) is always dominant and the rate of CCR (3.26) actually reduces to Eq. (3.25).

Finally we want to account for chain stretch effects, which locally reduce the rate of relaxation through CCR. Indeed, if one assumes that the tube persistence length is fixed, a stretched portion of the chain will have more constraint release sites than under equilibrium condition. Consequently, we define the local rate of relaxation due to constraint release $f_{\mathrm{cr}}^{\mathrm{loc}}$ as the sum of the rates of thermal and convective constraint release divided by the local stretch ratio:

$$f_{\mathrm{cr}}^{\mathrm{loc}}(t,s) = \left(\frac{1}{\tau_{\mathrm{cr}}} + f_{\mathrm{ccr}}(t)\right) \frac{3}{\mathrm{tr}\,\mathbf{c}(t,s)} . \tag{3.28}$$

A more detailed discussion of this modification of the rate of CCR can be found in [23].

3.3.6 The CRAFT model for monodisperse systems

In this section, we propose a model containing all the elements we presented so far plus finite extensibility effects. Additionally, we provide an expression for the stress tensor τ_p. Based on the assumption that one can simply add all the terms we proposed

for the time evolution of $\mathbf{c}$, we propose the following constitutive equation:

$$\begin{aligned}\overset{\triangledown}{\mathbf{c}}(t,s) &= \frac{\partial}{\partial s}\left(\alpha_d^f(s)\frac{\partial}{\partial s}(f\mathbf{c})\right)+\alpha_r\frac{\mathbf{c}}{\mathrm{tr}\,\mathbf{c}}\frac{\partial^2}{\partial s^2}(f\mathrm{tr}\,\mathbf{c}) \\ &\quad+\frac{\alpha_r}{2}\frac{\partial(f\mathrm{tr}\,\mathbf{c})}{\partial s}\frac{\partial}{\partial s}(\frac{\mathbf{c}}{\mathrm{tr}\,\mathbf{c}}) \\ &\quad-\left(\frac{1}{\tau_{\mathrm{cr}}}+f_{\mathrm{ccr}}\right)\frac{3}{\mathrm{tr}\,\mathbf{c}}(f\mathbf{c}-\delta)\end{aligned} \tag{3.29}$$

with,

$$\mathbf{c}(t,\pm 1) = \delta \tag{3.30}$$

$$f_{\mathrm{ccr}} = -\frac{\displaystyle\int_{-1}^{1}\left.\frac{Da(\mathbf{c})}{Dt}\right|_{\mathrm{stretch}}\mathrm{ds}}{\displaystyle\int_{-1}^{1}a(\mathbf{c})\,\mathrm{ds}}\,, \tag{3.31}$$

$$f(\mathbf{c}) = \frac{b-3}{b-\mathrm{tr}\,\mathbf{c}} \tag{3.32}$$

$$a(\mathbf{c}) = \left((b-3)\ln(1-\frac{\mathrm{tr}\,\mathbf{c}}{b})-\ln\det(\mathbf{c})\right) \tag{3.33}$$

$$\tau_p = G_N^0\frac{1}{2}\int_{-1}^{1}(f\mathbf{c}-\delta)\,\mathrm{ds}\;. \tag{3.34}$$

In the previous set of equations, $\alpha_d^f(s)$ is defined from Eq. (3.3), while α_r is defined as:

$$\alpha_r = \frac{4}{\pi^2 K_r M^2}\,, \tag{3.35}$$

where M is the molar mass of the polymeric chains. For both the linear and non-linear rheology the model has seven parameters: K_d, K_r, K_f, M_e, G_N^0, b and γ. Out of those seven, only b actually is a truly non-linear parameter.

The parameter b is called the finite extensibility parameter and is such that $\mathrm{tr}\,\mathbf{c} < b$. Defining L_{eq} as the equilibrium length of the primitive chain and $L_{\max}$ its maximum length, we have:

$$b = 3\frac{L_{\max}^2}{L_{\mathrm{eq}}^2} = 3N_k\,, \tag{3.36}$$

where N_k is the number of Kuhn steps between entanglements at equilibrium.

The parameter K_r is the scaling parameter for the Rouse time τ_r, which controls both the high frequency regime of the linear viscoelastic moduli and the stretch relaxation dynamics. Consequently, this parameter can be identified either on the linear

or on the non-linear response of the system. In this chapter we consider K_r as independent from K_d and M_e, and we will preferably identify its value on some non-linear experiment.

3.4 Computing numerical predictions

The CRAFT model has the form of a set of non-linear coupled PDEs along the s coordinate. The equations are coupled through the trace of $\mathbf{c}$ which appears in the stretch relaxation and constraint release terms, but also through the determinant of $\mathbf{c}$ which is found in the expression for f_{ccr}.

Before trying to solve these equations numerically, one can use the symmetry of the problem to reduce the s domain to the interval $]0,1[$. Zero flux boundary conditions are then imposed at $s = 0$. To solve the resulting PDEs on the reduced domain, we chose to discretize them along the s coordinate using a finite difference scheme. The discretization has to be fine enough to capture the boundary layer that appears at the chain ends for high deformation rates. Integration in time of the discretized system is then performed using an adaptive Runge-Kutta or Gear ODE solver. This last step should be performed with care, as the simulation of high molecular masses or very polydisperse systems is very likely to induce many different time-scales in the ODE, that may differ by orders of magnitude. The use of an ODE solver for stiff problems is therefore highly recommended, especially at high deformation rates.

In its discretized form, the model can be interpreted as a coupled multi-segment constitutive equation where the coupling between the modes is naturally imposed through the discretized differential operators along the primitive path.

3.5 Predictions in simple shear flow

In this section, we present the steady state and transient responses of the CRAFT model for simple shear flows. For all the figures, we set the value of γ to 1.15 and we define M_e as $M_e = \frac{3M\tau_r}{\tau_d}$.

In Fig. 3.2, we report the steady shear stress of the CRAFT model as a function of the Deborah number $\text{De} = \dot{\gamma}\tau_{\text{eff}}$, where $\dot{\gamma}$ is the shear rate and $\tau_{\text{eff}} = \frac{\eta_0}{G_N^0}$. Finite extensibility has been neglected as $b \to \infty$. We see that when the ratio τ_d/τ_r is small

enough, the curve is monotonic, but as this ratio gets bigger a shallow maximum appears in the curve. This feature is however smeared out as soon as polydispersity comes into play.

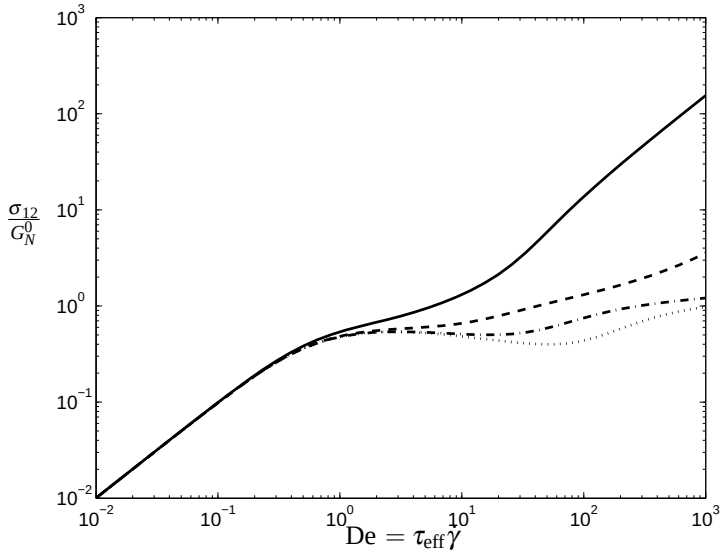

Figure 3.2: Steady state shear stress as a function of the Deborah number. The four curves correspond to different τ_d/τ_r ratios ($-$: ratio$=10$, $--$: ratio$=30$, $-\cdot$: ratio$=100$, $\cdots$: ratio$=300$).

Fig. 3.3 shows the transient shear viscosity for various shear rates for $\tau_d/\tau_r = 100$ and no finite exensibility effects. We observe that as the shear rate increases, an overshoot appears in the viscosity curve due to the transient stretching of the chain. At high shear rates the model also predicts a slight undershoot following the undershoot. In a following section we will see that these over- and under-shoots are observed experimentally and can be predicted quantitatively.

In Fig.3.4, we show the effects of finite extensibility on the predictions of the steady state shear stress. The parameters are identical to those used for Fig. 3.2 except for the finite extensibility parameter which we set to $b = 100$. Accounting for finite extensibility only changes the results at high shear rates, where it leads to reduced levels of stress.

In Fig. 3.5, we show the transient shear viscosity for different Deborah numbers. The ratio τ_d/τ_r is set to 30 while the finite extensibility parameter is set to 100. Accounting for finite extensibility can eventually lead, in the transient regime of very fast flows, to stress levels corresponding, at first sight, to more than affine deformations.

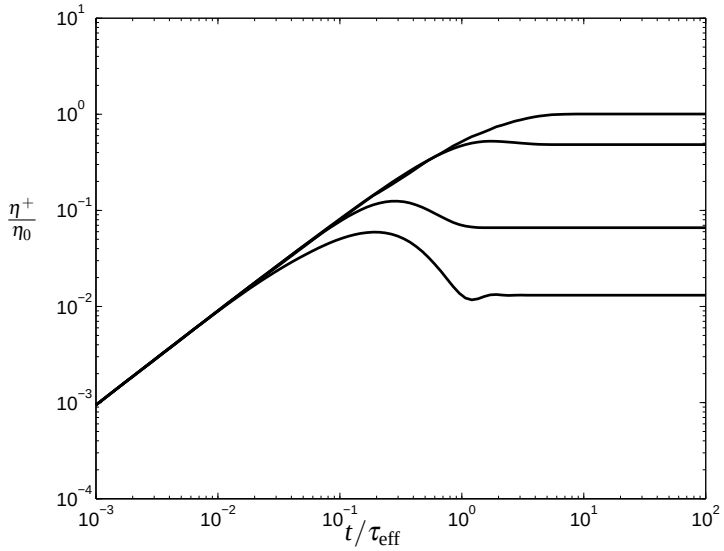

Figure 3.3: Transient shear viscosity for four different Deborah numbers. From the top, the respective Deborah numbers are 0.01, 1, 10 and 100. Finite extensibility has been neglected and $\tau_d/\tau_r = 30$.

This behaviour can nevertheless be expected as we are dealing with non-Gaussian chains. .

3.6 Predictions in uniaxial extension

As seen in recent publications [46; 7; 8; 36], there is a growing interest in measuring, predicting and understanding extensional flows of entangled systems. Fig. 3.6 shows the steady state Trouton ratio as predicted by the CRAFT model for different values of the finite extensibility parameter b and a ratio τ_d/τ_r of 100. As the extension rate increases we clearly see four different regimes:

1. The first regime corresponds to slow flows, where the material can relax sufficiently fast in order to maintain its equilibrium structure. Its response is therefore linear and the Trouton ratio is constant. As the flow rate increases, the microstructure begins to align in the flow direction. At the onset of this phenomenon, the additional stress, only due to orientation, actually grows faster that the flow rate. This is why one can observe a shallow maximum of the

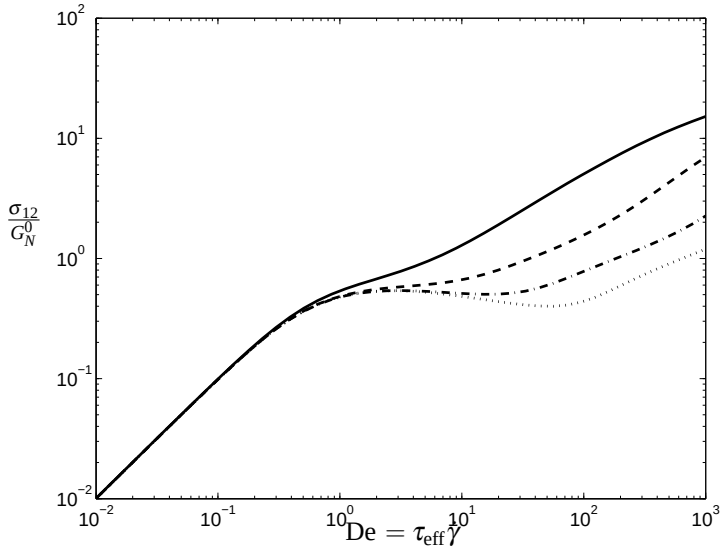

Figure 3.4: Steady state shear stress as a function of a Deborah number. The four curves correspond to different τ_d/τ_r ratios ($-$: ratio$=10$, $--$: ratio$=30$, $-\cdot$: ratio$=100$, $\cdots$: ratio$=300$). The parameter b is set to $b = 100$.

Trouton ratio when $\dot{\varepsilon}\tau_d$ is of order unity.

2. For increasing flow rates, reptation cannot prevent the microstructure from reaching a full orientation, but stretch relaxation is still fast enough to maintain the chains unstretched. As the stress saturates, we observe a decrease of the Trouton ratio. In this regime, the slope of the curve can reach a value of -1, if the reptation and stretch relaxation times are well separated. Even for a monodisperse system, the transition to this regime can actually be quite slow as our model exhibits the full spectrum of reptation coupled with constraint release.

3. When the flow is fast enough to stretch the chain, the extensional stress grows again beyond the value corresponding to full orientation of the microstructure in the flow direction. The stress growth is stopped when the chain reaches its full extension, and that is why this growth is not seen at all if the finite extensibility parameter b is small enough.

4. In the fourth regime, the Trouton ratio is a decreasing function of the extension rate. In this regime constraint release is the dominant mechanism and, as the chain is fully stretched, it has to retract as fast as it is stretched by the flow in order to remain below its maximum length. The induced rates of CCR are therefore of the order of the extension rate, which explains the decreasing Trouton

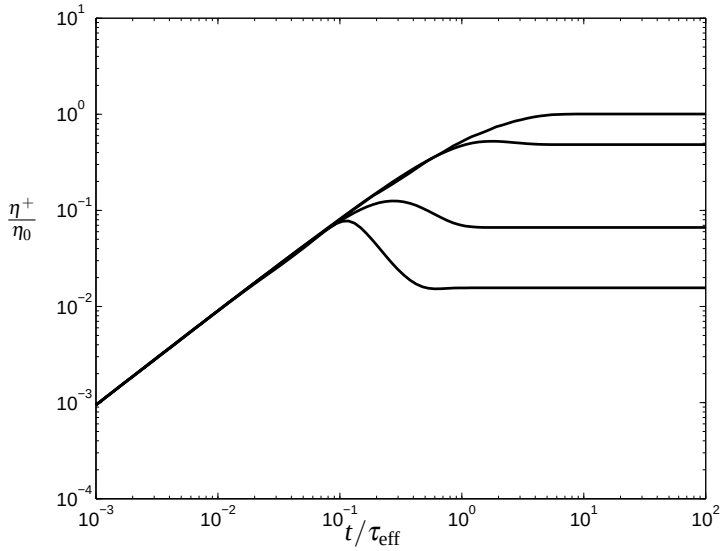

Figure 3.5: Transient shear viscosity for four different Deborah numbers. From the top, the respective Deborah numbers are 0.01, 1, 10 and 100. The finite extensibility parameter b is set to 100 and $\tau_d/\tau_r = 30$.

ratio. The exact shape of the curve actually depends on the non-linear expressions involved in the implementation of finite extensibility.

In Fig. 3.6, we see that for low values of the parameter b, the third regime is suppressed and the extensional viscosity is a monotonously decreasing function. Indeed, as the extensibility of the chains is very small they are almost instantaneously stretched to their maximum length once the flow rate is high enough. This instantaneous transition from unstretched to stretched corresponds to the instantaneous transition from the second to the fourth regime. .

3.7 The CRAFT constitutive equation for polydisperse systems

So far, we have focused on monodisperse systems, where all molecules have the same mass. In this section, we present the extension of the CRAFT constitutive equation to the polydisperse case. Going from the monodisperse to the polydisperse case with the

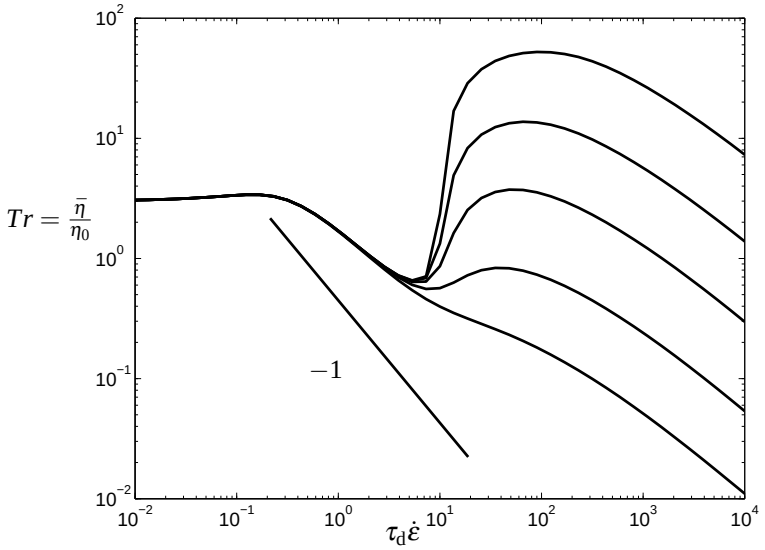

Figure 3.6: Steady state Trouton ratio for $\tau_d/\tau_r = 30$ and different values of the finite extensibility parameter b. From the top, the respective values of b are 1000, 300, 100, 30 and 10.

CRAFT model is actually very similar to what we did for linear visco-elasticity: the key issue is to find a consistent expression for the rate of constraint release f_{ccr} which couples the relaxation of all masses.

Let us consider a polymeric system with N different molecular masses $M^{(i)}$, each of them having a volume fraction $\phi^{(i)}$. The polydisperse CRAFT constitutive equation assumes that all masses relax independently except for the constraint release term. Indeed, as the chains all relax within the same environment, the rate of relaxation f_{ccr} must be the same for all masses and must be computed from the rate of relaxation of all masses. Furthermore, a polydisperse environment yields a broad spectrum of relaxation times, and we cannot further assume a single relaxation time τ_{cr} for thermal constraint release but a spectrum of N_{CR} characteristic times τ_j. These times τ_j and their respective weights w_j are computed as described in section 3.2 and ensure the correct linear viscoelastic limit of the model.

The polydisperse CRAFT constitutive is expressed as a set of N times N_{CR} partial differential equations (one per mass fraction and one per thermal constraint release mode) which are coupled only through the single term of convective constraint release. The variables of the model are the set of conformation tensors $\mathbf{c}^{(i)}(t,s)$, which describes the conformation of all masses along the primitive path. The equations for

the polydisperse CRAFT model read:

$$\begin{aligned}
\overset{\triangledown}{\mathbf{c}}^{(i,j)}(t,s) &= \frac{\partial}{\partial s}\left(\alpha_d^{f^{(i)}}(s)\frac{\partial}{\partial s}(f^{(i,j)}\mathbf{c}^{(i,j)})\right) \\
&\quad +\alpha_r^{(i)}\frac{\mathbf{c}^{(i,j)}}{\mathrm{tr}\,\mathbf{c}^{(i,j)}}\frac{\partial^2}{\partial s^2}(f^{(i,j)}\mathrm{tr}\,\mathbf{c}^{(i,j)}) \\
&\quad +\frac{\alpha_r^{(i)}}{2}\frac{\partial(f^{(i,j)}\mathrm{tr}\,\mathbf{c}^{(i,j)})}{\partial s}\frac{\partial}{\partial s}(\frac{\mathbf{c}^{(i,j)}}{\mathrm{tr}\,\mathbf{c}^{(i,j)}}) \\
&\quad -\left(\frac{1}{\tau_j}+f_{\mathrm{ccr}}\right)\frac{3}{\mathrm{tr}\,\mathbf{c}^{(i,j)}}\left(f^{(i,j)}\mathbf{c}^{(i,j)}-\delta\right)
\end{aligned} \tag{3.37}$$

with,

$$\mathbf{c}^{(i,j)}(t,\pm 1) = \delta \tag{3.38}$$

$$f_{\mathrm{ccr}} = -\frac{\sum_{i,j} w_j\phi^{(i)}\int_{-1}^{1}\left.\frac{Da(\mathbf{c}^{(i,j)})}{Dt}\right|_{\mathrm{stretch}}\mathrm{ds}}{\sum_{i,j} w_j\phi^{(i)}\int_{-1}^{1} a(\mathbf{c}^{(i,j)})\,\mathrm{ds}}\,, \tag{3.39}$$

$$f(\mathbf{c}) = \frac{b-3}{b-\mathrm{tr}\,\mathbf{c}} \tag{3.40}$$

$$a(\mathbf{c}) = G_N^0\left((b-3)\ln(1-\frac{\mathrm{tr}\,\mathbf{c}}{b})-\ln\det(\mathbf{c})\right) \tag{3.41}$$

$$\tau_p = G_N^0\sum_{i=1}^{N}\sum_{j=1}^{N_{CR}} w_j\phi^{(i)}\frac{1}{2}\int_{-1}^{1}(f\mathbf{c}-\delta)\,\mathrm{ds}\,. \tag{3.42}$$

In the linear limit, this set of equations actually reduces to the linear model recalled in section 3.2. In the non-linear regime, the CRAFT constitutive equation provides a mixing rule where the coupling mechanism gradually switches from thermal to convective constraint release. The definition of the rate of convective constraint release f_{ccr} (3.39) is a natural extension of the monodisperse case that still ensures a positive instantaneous relaxation time.

3.8 Comparison with experimental data

In two successive publications, Pattamaprom et al. [6] and Ye et al. [7] presented a complete set of experimental data for mono and bi-disperse entangled polystyrene solutions. The features of the six solutions, named S1 to S6 are reported in Table 3.1. From the linear viscoelastic moduli of S6 shown in Fig. 3.11, one sees that it

contains a significant fraction of smaller masses. We will nevertheless assume that S6 is monodisperse and consider S2 to S5 as strictly bidisperse samples.

For all solutions, the authors reported the linear viscoelastic moduli, the steady shear viscosity and first normal stress difference as well as the steady uniaxial extensional stresses. For some solutions, transient shear and extensional data were also reported. As different reference temperatures were used for the experiments presented in [6] and [7], we shifted the timescales of the extensional stress measurements to have a reference temperature of 40°C.

This set of data allows us to specifically test the various components of the CRAFT constitutive equation. In a first step, we evaluate the ability of the CRAFT model to fit the experimental results for the monodisperse system S1. Then we validate the ability to predict the response for the other monodisperse system S6 through the two scaling laws of Eqs. (3.3,3.35). Finally we test the mixing rule in the non-linear regime on the solutions S2 to S5.

The procedure we used to adjust the parameters of the CRAFT model is the following:

- We adjusted the parameters K_d, G_N^0 and γ in order to quantitatively predict the low and intermediate frequencies of the viscoelastic moduli of S1. In this process, we assumed $K_f = 1$.
- Using the transient shear viscosity data for S1, we adjusted the parameter K_r. Only the data for the highest extension rate was used.
- The finite extensibility parameter, derived on a micro-structural basis, was taken from [7].

Table 3.2 summarizes the values of the parameters.

Name	features
S1	7 % vol. PS $M_w = 2.9\,10^6$ Dalton, $M_w/M_n = 1.09$
S6	7 % vol. PS $M_w = 8.4\,10^6$ Dalton, $M_w/M_n = 1.17$
S2	80% S1, 20% S6
S3	60% S1, 40% S6
S4	40% S1, 60% S6
S5	20% S1, 80% S6

Table 3.1: Description of the six entangled polystyrene solutions S1 to S6 [6]

In Fig. 3.7, we see the comparison between the experimental viscoelastic moduli of S1, and the predictions of the constitutive equation. At high frequencies, a Rouse spectrum contribution was added to the predictions. The Rouse time for the linear response was computed as $\tau_r = K_r M^2$ and is therefore identical to the characteristic time of stretch relaxation. From the comparison with the experimental data, it seems that a longer Rouse time should have been used in order to have quantitative predictions in the whole frequency range.

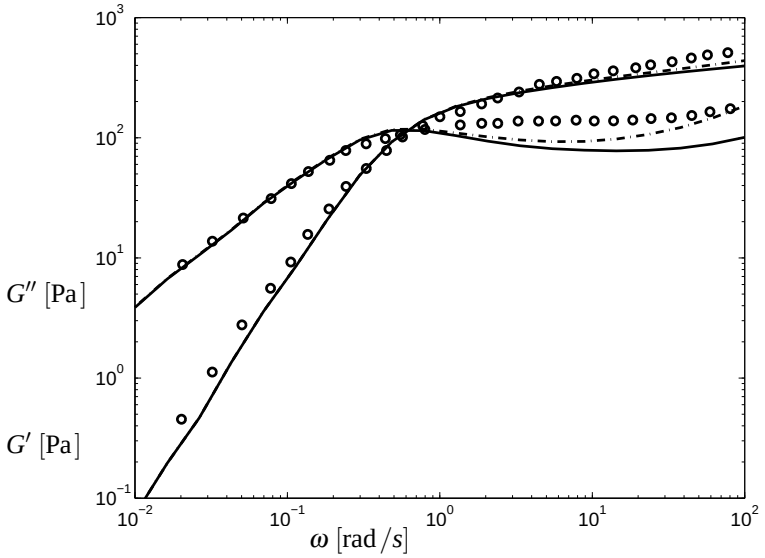

Figure 3.7: Linear viscoelastic moduli for S1. Comparison between experimental results [6](o) and the CRAFT model ($-$). The dashed lines are the predictions of the model for $K_r = 3.410^{-12}$ [sDalton^{-2}].

In Fig. 3.8, we report the experimental transient shear viscosity η^+ for S1, which we used for adjusting the stretch relaxation time of the model, together with the model predictions. We see that, with the appropriate stretch relaxation time, the CRAFT model predicts the steady state values and the transient behaviour. At high shear rates, the CRAFT model quantitatively predicts the large overshoot in viscosity followed by a shallow undershoot. At intermediate shear rates however, the model fails to quanti-

K_d	K_r	K_f	G_N^0	γ	b
$2.43\,10^{-19}$ [sDalton^{-3}]	$1.0\,10^{-14}$ [sDalton^{-2}]	1	465 [Pa]	1.0	942

Table 3.2: Parameters of the CRAFT model used for comparison with solutions S1 to S6 at 40°C.

tatively predict the overshoot in shear viscosity: stress built up during the overshoot relaxes too quickly. This failure is actually consistent with our observations for the linear response. In Figures 3.7 and 3.8, the dashed lines are the predictions of the model with the Rouse time increased by a factor 3.4. We see that this yields simultaneously better quantitative predictions both for the linear moduli and the transient shear viscosity at low deformation rates.

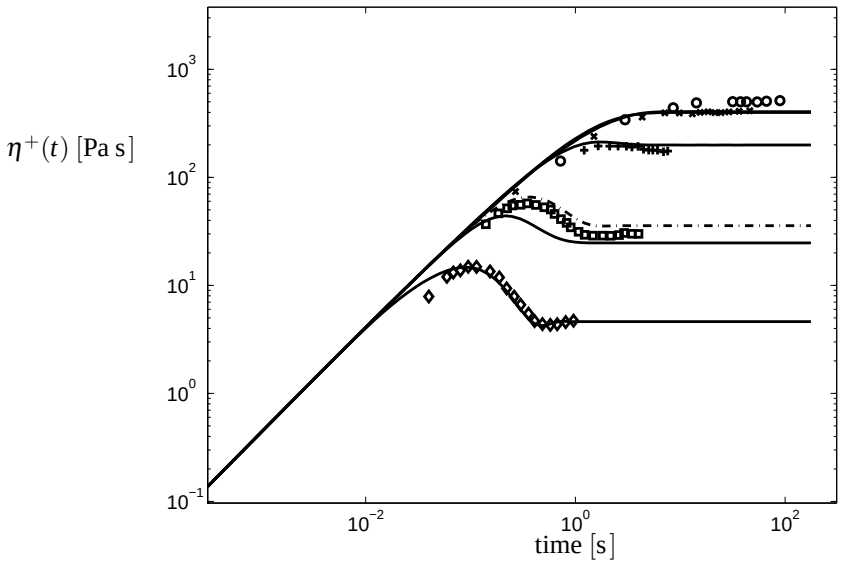

Figure 3.8: Transient shear viscosity for S1. Comparison between experimental results [6] (symbols) and the CRAFT model (−). From top to bottom, the curves correspond to the following flow rates: $0.01[s^{-1}]$, $0.1[s^{-1}]$, $1[s^{-1}]$, $10[s^{-1}]$ and $100[s^{-1}]$. The dashed lines is the prediction of the model for $K_r = 3.410^{-12}\,[\mathrm{sDalton}^{-2}]$, at a flow rate of $10[s^{-1}]$.

This closes the first step of parameters adjustment: the parameters are now frozen and we can examine the predictions of the models in shear for S1 and S6, and in shear and extension for the blends S2 to S5.

As foreseen in Fig. 3.8, Fig. 3.9 shows the excellent agreement of the steady shear viscosity of S1 with the model predictions. The steady state first normal stress difference is predicted quantitatively as well. The main difference between the data and the predictions is the “kink” one observes on the predicted curves at shear rates for which the chain becomes significantly stretched. These are not observed experimentally and suggest that the model predicts too much chain stretch in shear.

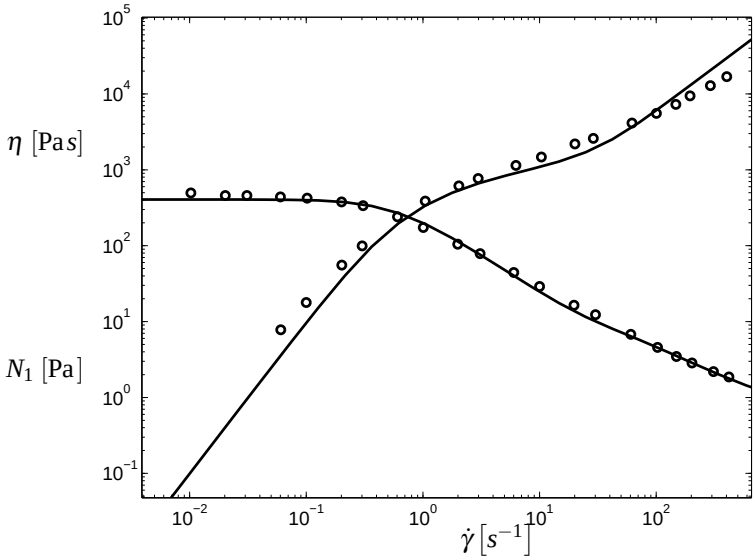

Figure 3.9: Steady state shear viscosity η and first normal stress difference N_1 for S1. Comparison between experimental results [6] (o) and the CRAFT model ($-$).

In Fig. 3.10, the experimental steady extensional viscosity is compared to the model predictions. The rise of the extensional viscosity due to the onset of chain stretch is well described, qualitatively and quantitatively, which tends to confirm the value we selected for the Rouse time. The viscosity decay observed at lower extension rates is overestimated by the model. Similar predictions have been obtained by Bhattacharjee et al. [46] in comparing similar entangled solutions with the predictions of different constitutive models. Further modelling efforts need to be spent to describe these deviations from the theoretical -1 slope. The fourth regime (see section 3.6) of the extensional viscosity is unfortunately out of the range of the experiments and the validity of the CRAFT predictions at high extension rates cannot be assessed.

Fig. 3.11 offers the same comparison as Fig. 3.7 but for the solution S6. Looking at the experimental loss modulus for intermediate frequencies clearly shows that the sample is not monodisperse as we are assuming. Nevertheless, we are able to correctly predict the low frequency range of the loss modulus, which ensures good predictions of the zero-shear viscosity η_0. As for solution S1, the Rouse time of the model is again too high to describe well the high frequency regime of G' and G''.

In Fig. 3.12, we show that the scaling law for α_r allows the CRAFT model to make good predictions of the extensional viscosity of solution S6. The onset of chain stretch is well predicted, but the sparsity of the data prevents any further analysis. The

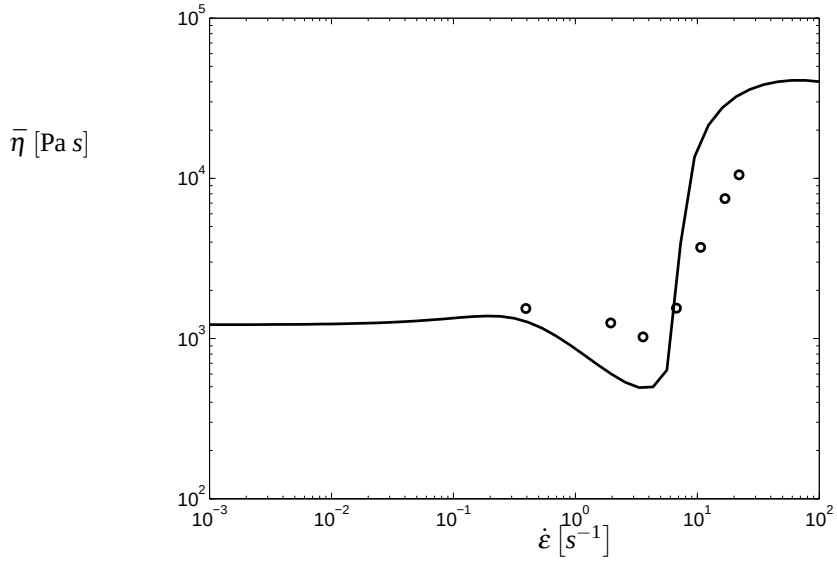

Figure 3.10: Steady extensional viscosity for S1. Comparison between experimental results [7] (o) and the CRAFT model ($-$).

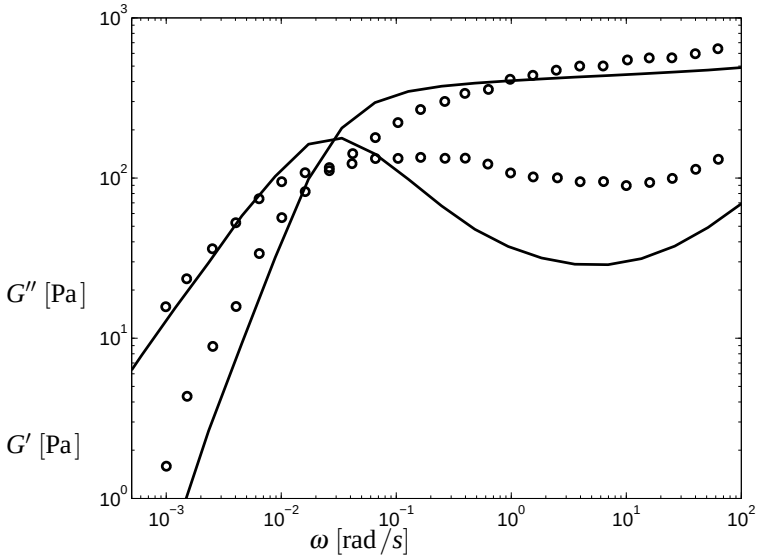

Figure 3.11: Linear viscoelastic moduli for S6. Comparison between experimental results [6] (o) and the CRAFT model ($-$).

presence of shorter chains in the sample is likely to explain the somewhat delayed hardening observed in the experimental data.

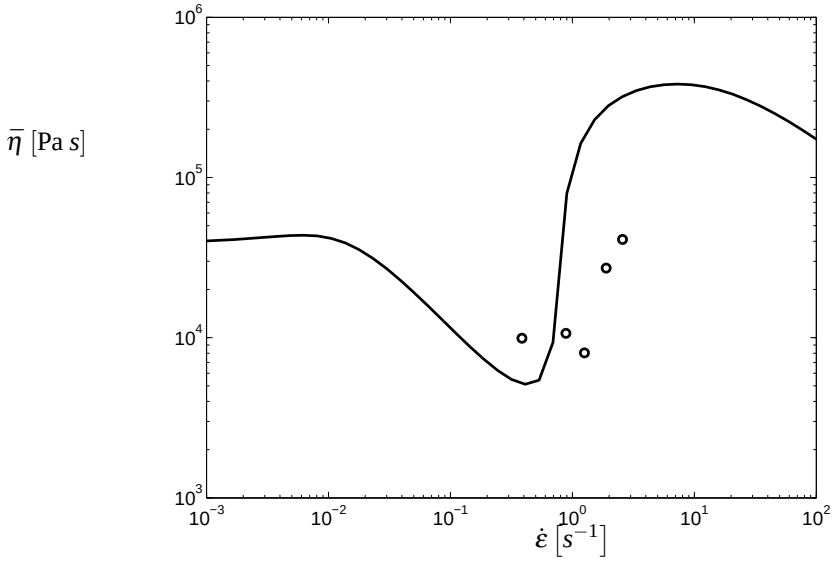

Figure 3.12: Steady extensional viscosity for S6. Comparison between experimental results [7] (o) and the CRAFT model ($-$).

In Fig. 3.13, we see that the model correctly predicts the steady shear viscosity and first normal stress difference of S6 over a wide range of shear rates. Discrepancies between predictions and experiments only occur at high shear rates, where the model predicts that the flow starts stretching the chains, leading to a change of slope of the curves. The kink in the predictions occurring at high shear rates is more visible for S6 than it is for S1, as the increase in molecular weight yields a greater separation between τ_d and τ_r.

Fig. 3.14 shows the predictions of the steady shear viscosity and first normal stress difference for the solutions S2 to S5. One should remember that the predictions for solutions S2 to S5 did not require any additional material parameter. From a global point of view, one can say that the agreement between predictions and experiments is quite good, but several comments arise from a closer look at the curves:

- the model is able to give a reasonable prediction of the zero shear rate viscosity η_0 for all solutions. This linear limit can be expected from the linear theory behind the CRAFT model.

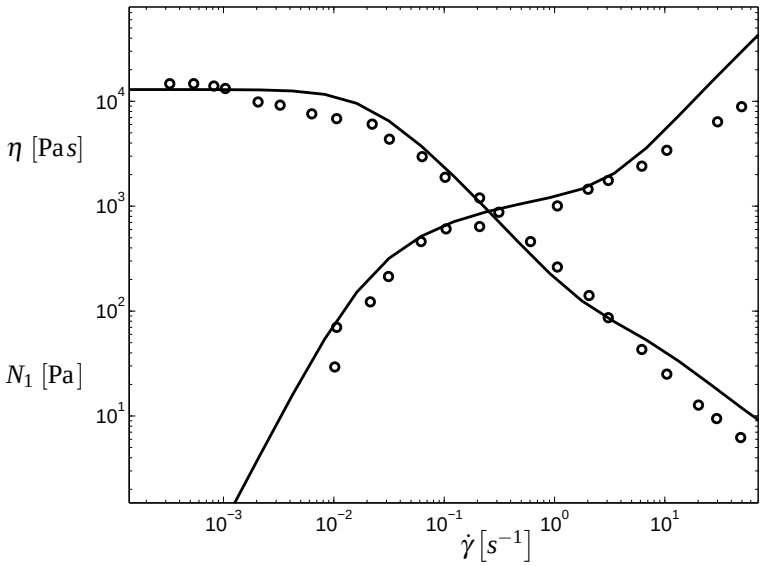

Figure 3.13: Steady state shear viscosity η and first normal stress difference N_1 for S6. Comparison between experimental results [6] (o) and the CRAFT model ($-$).

- For CCR dominated shear rates, the predictions of the CRAFT are in very good agreement with experiments. The non-linear mixing rule coming from our generalized convective constraint release seems quite efficient in this regime.

- As for the monodisperse samples, the CRAFT model predicts a transition to a "stretched regime" at high shear rates, which is not seen in the experiments.

Fig. 3.15 shows the predictions of the steady extensional viscosity together with experimental measurements for solutions S2 to S5. Because only few experimental points are available, we can only observe that the model is able to predict the extensional viscosity growth at about the right extension rate. Additionally, we still observe a too strong extensional thinning of the model. The experimental extension rates are too small in order to validate the behaviour of the CRAFT model in the last regime of the viscosity curve.

In Fig. 3.16, we show both the transient shear viscosity and first normal stress difference for S3. The ability of the CRAFT model to predict the transient response of bi-disperse samples actually is a strong test for its mixing rule. We see that for low and medium shear rates, the predictions are in excellent agreement with the data. At high shear rates, the occurence of high levels of stretch ruins the transient predictions.

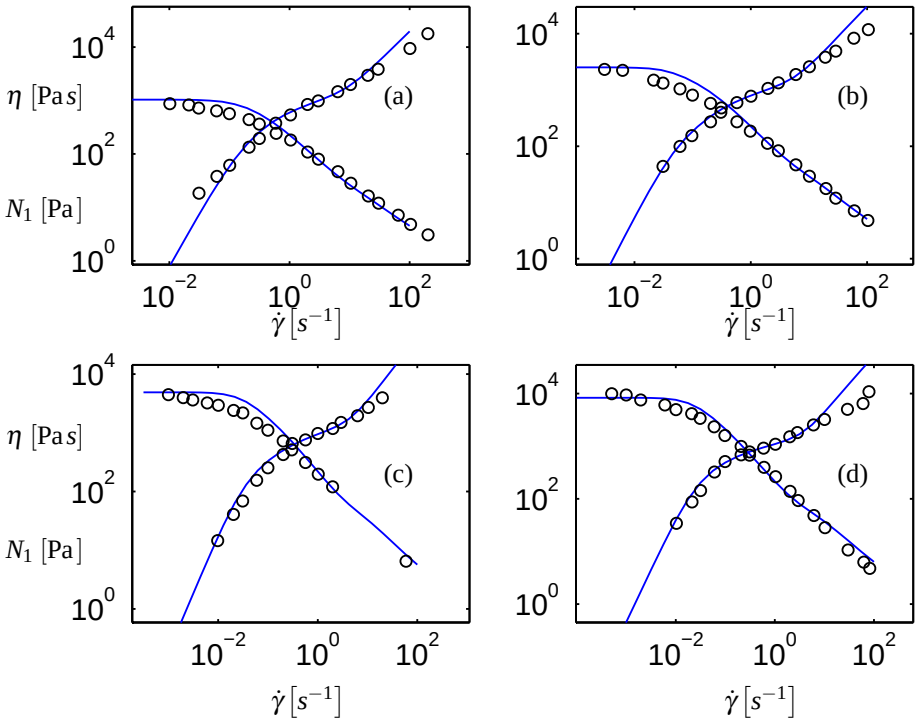

Figure 3.14: Steady state shear viscosity η and first normal stress difference N_1 for S2 (a), S3 (b), S4 (c) and S5 (d). Comparison between experimental results [6] (o)and the CRAFT model ($-$).

3.9 Conclusions

We have proposed a new tube-based constitutive equation named CRAFT for polydisperse linear entangled polymers. The model has the form of a set of coupled partial differential equations for a configuration tensor defined along the primitive chain coordinate.

In addition to reptation, contour-length fluctuations and thermal constraint release, CRAFT accounts for the coupled relaxation of stretch and orientation along the primitive chain. Convective Constraint Release (CCR) appears naturally in the model, as a non-linear correction to thermal constraint release.

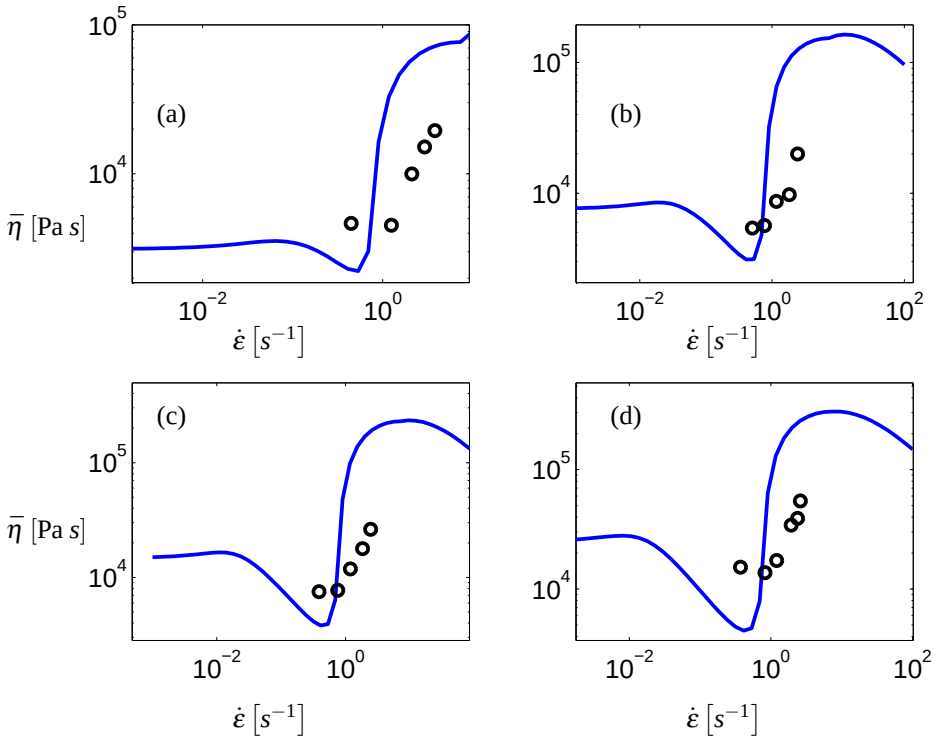

Figure 3.15: Steady extensional viscosity for S2 (a), S3 (b), S4 (c) and S5 (d). Comparison between experimental results [7] (o) and the CRAFT model ($-$).

The description of polydisperse systems with the CRAFT model requires no additional material parameter and the coupling between the different masses is provided by constraint release effects. In the linear regime the CRAFT model reduces to a simple theory [35] capable of quantitative predictions, even for polydisperse systems. The deep connection of the CRAFT model with a linear theory allows the identification of most of the parameters on linear viscoelastic data only.

The preliminary comparison of the CRAFT predictions with experimental data is very promising. On mono- and bi-disperse entangled polystyrene solutions, we have show that the CRAFT model is able to correctly predict the steady shear viscosity and first normal stress difference over a wide range of shear rates. Additionally, the onset of extensional strain hardening is well predicted for steady state flows. Transient experiments can be quantitatively predicted as well. The lesser quality of the predictions at high shear rates and the excessive extensional thinning of the model tend to indicate

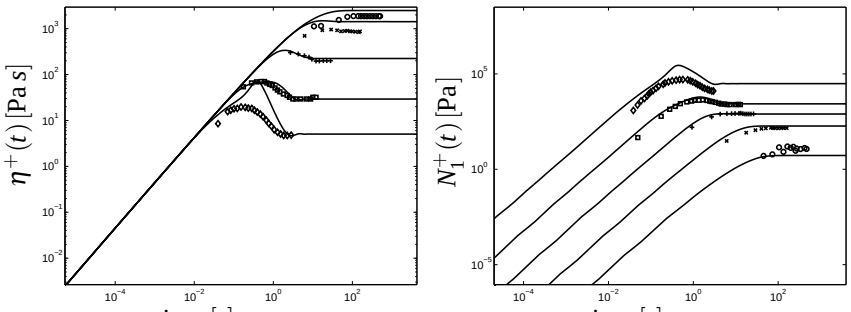

Figure 3.16: Transient shear viscosity (a) and transient first normal stress difference for S3. Comparison between experimental results [6] (symbols) and the CRAFT model (−). From top to bottom (a) and bottom to top (b), the curves correspond to the following flow rates: $0.01[s^{-1}]$, $0.1[s^{-1}]$, $1[s^{-1}]$, $10[s^{-1}]$ and $100[s^{-1}]$

that additional stretch relaxation mechanisms should be accounted for.

3.10 Appendix: On the rate of CCR

In this appendix, we prove that under certain conditions and assumptions, the rate of convective constraint release defined through Eq. (3.26) is always positive. For clarity, we will restrict ourselves to the monodisperse case.

From the definition of the tensor $\mathbf{c}(t,s)$ we see that its equilibrium value is the identity tensor. Furthermore, the evolution equation for $\mathbf{c}(t,s)$, is such that $\mathbf{c}(t,s)$ always remains symmetrical. We now assume that the tensor $\mathbf{c}(t,s)$ always remains strictly positive definite. We do not prove this assumption but if, for an arbitrary flow history, one of the eigenvalues of $\mathbf{c}(t,s)$ was to become negative it would have to become null, as a result of continuity. As the logarithm of the determinant of $\mathbf{c}(t,s)$ enters the evolution equation, we see that the differential equation would not be defined in such case.

When finite extensibility is not accounted for, $a(\mathbf{c})$ is defined as:

$$a(\mathbf{c}) = \mathrm{tr}\,(\mathbf{c}) - \ln\det(\mathbf{c})\ ,$$

and is equal to 3 at equilibrium. The gradient of $a(\mathbf{c})$ with respect to $\mathbf{c}$ is:

$$\frac{\partial a}{\partial \mathbf{c}} = \left(\delta - \mathbf{c}^{-1}\right) .$$

The function $a(\mathbf{c})$ is strictly positive when $\mathbf{c}$ is positive definite. This can be proved by noticing that the gradient of $a(\mathbf{c})$ with respect to $\mathbf{c}$ only vanishes at equilibrium and that the Hessian is positive definite as well. The denominator on the right hand side of Eq. (3.26) is therefore always strictly greater than zero. Let us now prove that the numerator (without the minus sign) is strictly negative.

The expression inside the integral of the numerator of Eq. (3.26) can be written as follows:

$$\begin{aligned}
\left.\frac{D}{Dt} a(\mathbf{c}(t,s))\right|_{\text{stretch}} &= \alpha_r \frac{\partial^2}{\partial s^2}(\operatorname{tr}\mathbf{c}) \frac{\mathbf{c}}{\operatorname{tr}\mathbf{c}} : \frac{\partial a}{\partial \mathbf{c}} \\
&= \alpha_r \frac{\partial^2}{\partial s^2}(\operatorname{tr}\mathbf{c}) \frac{\mathbf{c}}{\operatorname{tr}\mathbf{c}} : \left(\delta - \mathbf{c}^{-1}\right) \\
&= \alpha_r \frac{\partial^2}{\partial s^2}(\operatorname{tr}\mathbf{c}) \left(1 - \frac{3}{\operatorname{tr}\mathbf{c}}\right) . \qquad (3.43)
\end{aligned}$$

The numerator of Eq. (3.26) is therefore equal to:

$$\int_{-1}^{1} \alpha_r \frac{\partial^2}{\partial s^2}(\operatorname{tr}\mathbf{c}) \left(1 - \frac{3}{\operatorname{tr}\mathbf{c}}\right) \mathrm{d}s .$$

We will now conclude the proof by showing that the previous expression is always strictly negative.
Let $g(s)$ be a continuous and sufficiently smooth function on the interval $[-11]$. If $g(s)$ is strictly positive and is such that $g(1) = g(-1) = 3$, we have the following result:

$$\int_{-1}^{1} \frac{\partial^2}{\partial s^2} g(s') \left(1 - \frac{3}{g(s')}\right) \mathrm{d}s' \leq 0 .$$

The proof of this inequality only requires basic calculus and one integration by parts.

$$\begin{aligned}
&\int_{-1}^{1} \frac{\partial^2}{\partial s^2} g(s') \left(1 - \frac{3}{g(s')}\right) \mathrm{d}s' \\
= &\int_{-1}^{1} \frac{\partial^2}{\partial s^2} g(s') \,\mathrm{d}s' - \int_{-1}^{1} \frac{3}{g(s')} \frac{\partial^2}{\partial s^2} g(s') \,\mathrm{d}s' .
\end{aligned}$$

The first term is simply integrated, while the second is integrated by parts:

$$
\begin{aligned}
&= \left[\frac{\partial}{\partial s}g(s)\right]_{-1}^{1} - \left[\frac{3}{g(s)}\frac{\partial}{\partial s}g(s)\right]_{-1}^{1} - \int_{-1}^{1}\frac{3}{g(s')^2}\left(\frac{\partial}{\partial s}g(s')\right)^2 \mathrm{d}s' \qquad (3.44)\\
&= -\int_{-1}^{1}\underbrace{\frac{3}{g(s')^2}\left(\frac{\partial}{\partial s}g(s')\right)^2}_{\geq 0}\mathrm{d}s' \leq 0\,.
\end{aligned}
$$

The two first terms of Eq. 3.44 cancel each other as $g(-1) = g(1) = 3$, while the last term is non-negative. This concludes the proof that our definition of the rate of CCR always yields a non-negative value, even when the flow tends to drive the chain below its equilibrium length.

Chapter 4

Non-linear flows of well characterized polystyrene melts, simulation and comparison with experiments

4.1 Introduction

The description and the prediction of the rheology of linear entangled polymers rely nowadays more and more on microstructural models. A first breakthrough in modelling entangled systems came with the Doi and Edwards (DE) model [12]. Although the DE model can predict the damping function constructed from step strain experiments, the model does not account for chain stretch effects and is too shear thinning. Following the DE model, many tube-based models have been proposed to improve the predictions of the DE model while retaining its relative simplicity. Among the recent constitutive equations, the CRAFT is a constitutive model [47], which can make quantitative predictions in both the linear [35] and the non-linear [47] regimes. A particularity of the CRAFT model is that all of its parameters but one can be identified from the linear spectrum of the polymeric system. The only truly non-linear parameter controls finite extensibility and can be deduced from microstructural knowledge.

The non-linear response of entangled polymers can be probed through a variety of rheometrical shear and extensional flows, each of them providing different information on the tested material. The quality of a constitutive model is often established through the ability of the model to predict the response of the material under different flow regimes. Large Amplitude Oscillatory Shear flows (LAOS) and uniaxial extension provide tough test for constitutive equations.

At small amplitudes, oscillatory shear flows are used to measure the linear response of the material. Large amplitude oscillatory shear flows offer the opportunity to study the non-linear response of a material with a smooth flow where both the strain and the rate of strain are well controlled. The experimental methods and the data analysis associated with LAOS flows have been reviewed in detail by Giacomin and Dealy [48]. The spectral analysis of the response to LAOS flow, often referred at as Fourier-transform rheology, has been addressed by Wilhelm et al. [49; 50]. Although LAOS experimental data can be represented in the time and frequency domains, the interpretation of the non-linear response remains a challenge. The variety of non-linear responses observed under LAOS indicates that it might be used as a classification tool for the qualitative characterization of materials [51]. In a recent work, Debbaut and Burhin [52] have investigated the LAOS response of a commercial high density polyethylene melt. Up to moderate strains, the experimental results agreed with the predictions of a multi-mode Giesekus model. The comparison of LAOS data with the predictions of a constitutive model might offer the only way to a non-phenomenological interpretation of the measured non-linear response.

Extensional flows orient and stretch the polymeric chains to a large extent, and provide information on the branching structure, which cannot easily be inferred from the linear response. Bach et al. [8] have recently published unique experimental data on the extensional viscosity of monodisperse linear polystyrene melts. Marrucci and Ianniruberto [36] have shown how this set of data contradicts the predictions of most of todays constitutive equations. Moreover, they have suggested an additional relaxation phenomenon to account for the observed discrepancies.

In this work, we investigate linear polystyrene melts under LAOS and uniaxial extension using the CRAFT model. We first identify the linear parameters of the model from the linear response of two linear polystyrene samples. The only non-linear parameter, related to finite extensibility, is obtained from microstrutural knowledge. We show that as long as the chains are not stretched, the CRAFT model predicts quantitatively the LAOS response of mono- and poly-disperse polystyrene melts. In order to improve the predictions of the model for LAOS regimes where the chains become stretched, we introduce a phenomenological modification of the finite extensibility parameter. Finally, we show how this modification yields to predictions that qualitatively agree with the data of Bach et al. [8] in uniaxial extension.

4.2 The CRAFT model

The CRAFT model is a full chain microstructural constitutive equation for polydisperse entangled linear polymers. Details on the CRAFT model can be found elsewhere [47]. We will only recall the equations of the model and its structure. The model accounts, in a coupled description, for reptation contour-length fluctuations, chain stretch relaxation, thermal and convective constraint release. In order to model the connectivity of the polymeric chains, a lagrangian parametric coordinate s is defined along the primitive path. The variables of the model are the conformation tensors $\mathbf{c}^{(i,j)}(t,s)$ describing both the orientation and stretch of the microstructure along the primitive path. The superscript (i) corresponds to the i^{th} mass $M^{(i)}$ of a polydisperse system, while the superscript (j) corresponds to a multimode decomposition of the dynamics of thermal constraint release [35]. The evolution equation for $\mathbf{c}^{(i,j)}(t,s)$ reads:

$$\begin{aligned}
\overset{\triangledown}{\mathbf{c}}^{(i,j)}(t,s) &= \frac{\partial}{\partial s}\left(\alpha_d^{(i)}(s)\frac{\partial}{\partial s}(f^{(i,j)}\mathbf{c}^{(i,j)})\right) \qquad (4.1)\\
&\quad +\alpha_r^{(i)}\frac{\mathbf{c}^{(i,j)}}{\operatorname{tr}\mathbf{c}^{(i,j)}}\frac{\partial^2}{\partial s^2}(f^{(i,j)}\operatorname{tr}\mathbf{c}^{(i,j)})\\
&\quad +\frac{\alpha_r^{(i)}}{2}\frac{\partial(f^{(i,j)}\operatorname{tr}\mathbf{c}^{(i,j)})}{\partial s}\frac{\partial}{\partial s}(\frac{\mathbf{c}^{(i,j)}}{\operatorname{tr}\mathbf{c}^{(i,j)}})\\
&\quad -\left(\frac{1}{\tau_j}+f_{\text{ccr}}\right)\frac{3}{\operatorname{tr}\mathbf{c}^{(i,j)}}\left(f^{(i,j)}\mathbf{c}^{(i,j)}-\delta\right)\\
&\text{with,}\\
\mathbf{c}^{(i,j)}(t,\pm 1) &= \delta \qquad (4.2)\\
f_{\text{ccr}} &= -\frac{\sum_{i,j} w_j\phi^{(i)}\int_{-1}^{1}\left.\frac{Da(\mathbf{c}^{(i,j)})}{Dt}\right|_{\text{stretch}}\text{ds}}{\sum_{i,j} w_j\phi^{(i)}\int_{-1}^{1} a(\mathbf{c}^{(i,j)})\,\text{ds}}\,, \qquad (4.3)\\
f(\mathbf{c}) &= \frac{b-3}{b-\operatorname{tr}\mathbf{c}} \qquad (4.4)\\
a(\mathbf{c}) &= G_N^0\left((b-3)\ln(1-\frac{\operatorname{tr}\mathbf{c}}{b})-\ln\det(\mathbf{c})\right) \qquad (4.5)\\
\tau_p &= G_N^0\sum_{i=1}^{N}\sum_{j=1}^{N_{CR}} w_j\phi^{(i)}\frac{1}{2}\int_{-1}^{1}(f\mathbf{c}-\delta)\,\text{ds}\,. \qquad (4.6)
\end{aligned}$$

The first term on the right hand side of Eq. 4.1 accounts for the reptation of the primitive chain and contour-length fluctuations. The position dependent diffusion process models the enhanced relaxation observed at chain ends due to contour-length fluctua-

tions. The expression for the diffusion coefficient $\alpha_d^{f\,(i)}$ reads:

$$\alpha_d^{f\,(i)}(s) = \frac{4}{K_d\pi^2 {M^{(i)}}^3}\frac{{K_f}^2 M_e}{M^{(i)}\left(1-s\right)^2} \text{ if } s > \left(1-K_f\sqrt{\frac{M_e}{M^{(i)}}}\right) \tag{4.7}$$

$$\frac{4}{K_d\pi^2 {M^{(i)}}^3}\frac{{K_f}^2 M_e}{M^{(i)}\left(1-s\right)^2} \text{ if } s < \left(K_f\sqrt{\frac{M_e}{M^{(i)}}}-1\right) \tag{4.8}$$

$$\frac{4}{K_d\pi^2 {M^{(i)}}^3} \text{ otherwise,} \tag{4.9}$$

where K_d is a material parameter. The adjustable parameter K_f is close to unity and controls the depth of the contour-length fluctuations within the model. The mass dependent reptation disengagement time is defined as:

$$\tau_d(M) = K_d M^3 \ . \tag{4.10}$$

The second and third terms account for the stretch dynamics, coupled with the orientation of the microstructure. The coefficient $\alpha_r^{(i)}$ is defined as:

$$\alpha_r^{(i)} = \frac{4}{\pi^2 K_r {M^{(i)}}^2} \ , \tag{4.11}$$

where K_r is a material parameter. The Rouse time is defined as:

$$\tau_r(M) = K_r M^2 \ . \tag{4.12}$$

The last term of Eq. 4.1 accounts for thermal and convective constraint release. The rate of constraint release is defined as the sum of a constant contribution $\frac{1}{\tau_j}$ from thermal constraint release and a time dependent contribution f_{ccr} from convective constraint release. The thermal constraint release times τ_j are such that they provide a good approximation of the double reptation [5] approach to constraint release. For a given number N_{CR} of modes, the characteristic times τ_j and their respective weights w_j are such that they minimize the following expression:

$$\int_0^\infty \left(K_{CR}(t) - \sum_{j=1}^{N_{CR}} w_j \exp\left(\frac{-t}{\tau_j}\right)\right)^2 \mathrm{d}t \ , \tag{4.13}$$

under the constraint that:

$$\int_0^\infty K_{CR}(t)^{1/\gamma}\left(K_{CR}(t) - \sum_{j=1}^{N_{CR}} w_j \exp\left(\frac{-t}{\tau_j}\right)\right) \mathrm{d}t \ . \tag{4.14}$$

The constraint release kernel of double reptation $K_{CR}(t)$ is computed as:

$$K_{CR}(t) = \left(\sum_{i=1}^{N} \int_{-1}^{1} \phi^{(i)} P_0^f(t,s)\,\mathrm{d}s \right)^{\gamma} , \tag{4.15}$$

where N is the number of masses in the system, $\phi^{(i)}$ is the volume fraction of mass $M^{(i)}$ and γ is an adjustable parameter of order unity, representative of the effectiveness of thermal constraint release. The functions $P_0^f(t,s)$ are the solutions of the following differential problem:

$$\begin{aligned} \frac{\partial}{\partial t} P_0^{f\,(i)} &= \frac{\partial}{\partial s}\left(\alpha_d^{f\,(i)}(s) \frac{\partial}{\partial s} P_0^{f\,(i)} \right) , \\ P_0^{f\,(i)}(t,-1) &= 0 , \\ P_0^{f\,(i)}(t,1) &= 0 \text{ for } t > 0 , \\ P_0^{f\,(i)}(0,s) &= 1 \text{ for } -1 < s < 1 . \end{aligned} \tag{4.16}$$

The constraint (4.14) actually ensures that the zero-shear viscosity predicted by the model is not perturbed by the multi-mode approximation of thermal constraint release. To ensure that both τ_j and w_j are positive, the minimization procedure is carried out in logarithmic space.
The definition (4.3) of the rate of convective constraint release f_{ccr} is an ansatz that is equivalent e.g. to the expression proposed by Marrucci et al. [41] when stretch relaxation is the dominant relaxation mechanism and stretch levels are moderate. This particular expression has, however, the advantage of always predicting a positive rate of convective constraint release, even in reversing flows where other models [26; 41] would predict a negative value.

Finally, Eq. (4.6) for the stress tensor τ_p is nothing but a weighted average of the contributions from all segments of all masses and modes.
When predicting the linear viscoelastic moduli of an entangled system, we superpose a Rouse contribution to the predictions of the model using the expression found in [15].

The CRAFT model has been successfully validated [33] on a very complete set of published [6; 7] experimental data of concentrated polystyrene solutions.

4.3 Large Amplitude Oscillatory Shear Flows

Among the different flows used to study the rheological response of a material, the small amplitude oscillatory shear flow (SAOS) is the most widely used. It allows the measure of the linear elastic and loss moduli (G' and G'') which respectively characterize the in-phase and out-of-phase response of a material subject to a small amplitude periodic strain. On the other hand, a wide variety of shear and extensional flows are used to characterize the non-linear response of complex fluids. Among those techniques, Large Amplitude Oscillatory Shear flow (LAOS) can be seen as a non-linear, continuous, extension of small amplitude oscillatory shear flows.

In a LAOS flow, the deformation imposed on the material is of the form:

$$\gamma(t) = \gamma_0 \sin(\omega t) \,, \tag{4.17}$$

where γ_0 is the maximum strain and ω is the angular frequency. The time frequency ν is defined as $\nu = \frac{\omega}{2\pi}$. Unlike SAOS, LAOS experiments reach shear strains of several strain units. From Eq. (4.17), we see that the rate of strain is:

$$\dot{\gamma}(t) = \omega\gamma_0 \cos(\omega t) \,. \tag{4.18}$$

The two independent parameters of a LAOS flow, the angular frequency and the maximum strain, allow one to define a Deborah and a Weissenberg number which can be controlled independently:

$$\mathrm{De} = \lambda\omega \,, \tag{4.19}$$

$$\mathrm{We} = \lambda\omega\gamma_0 \,. \tag{4.20}$$

The Deborah number is the ratio of the characteristic relaxation time λ of the material to the characteristic time ω^{-1} of the deformation. An increase in the Deborah number represents a transition from a viscous to a more elastic response of the material. The Weissenberg number involves the maximum deformation and measures the amount of material non-linearity involved in the experiment. The linear regime probed by SAOS experiments is that of small Weissenberg numbers and arbitrary Deborah numbers. LAOS flows provide a tough test for constitutive models as this is one of the only rheometrical flows where the Deborah and the Weissenberg numbers can be tuned independently. In this work, we define the characteristic time λ from the ratio of the zero shear viscosity η_0 to the plateau modulus G_N^0.

Upon startup of a LAOS flow, a dynamic regime is established once the initial conditions have been "forgotten". In this dynamical regime, the shear stress σ is a periodic function of time with a zero mean. Consequently, the shear stress can be

decomposed in the following sum of harmonics:

$$\sigma = \sum_{i=1}^{\infty} A_n sin(n\omega t) + B_n cos(n\omega t) \, , \tag{4.21}$$

where A_n and B_n are the Fourier coefficients. The amplitude C_n of the harmonics is defined as $C_n = \sqrt{A_n^2 + B_n^2}$ and the phase angle δ_n as $\delta_n = \arctan\left(\frac{A_n}{B_n}\right)$. In these definitions, we explicitly assume that the applied deformation follows Eq. (4.17) and has therefore a zero phase angle. In the case of a perfect viscometric flow where inertia and wall slip effects are absent, the spectrum of σ only contains odd harmonics. For a more comprehensive analysis of Fourier-transform rheology, see Wilhelm et al. [49].

Fourier-transform rheology is a sensitive tool that can follow the transition from a linear to a non-linear response. Furthermore, fine details in the non-linear response can be identified from the higher harmonics. The analysis of the non-linear frequency response lies, however, only at the phenomenological level as long as it cannot be compared to the predictions of a constitutive model. Only B_1 can be related to the lost work per cycle and unit volume W_C:

$$W_C = \oint \sigma \mathrm{d}\gamma = \pi \gamma_0 B_1 \, [\mathrm{J/m^3}] \, . \tag{4.22}$$

4.4 Materials and parameters identification

We have access to the linear viscoelastic moduli and the LAOS data of four polystyrene samples: PS140, PS1, PS2 and PS3. The three samples PS1, PS2 and PS3 were provided by BASF, while PS140 is a well known calibration sample provided by Prof. C. Friedrich (Freiburger Materialforschungszentrum, Albert-Ludwigs-Universität). Samples PS140 and PS1 have a narrow molecular weight distribution and will be considered monodisperse for this work. On the other hand, PS2 shows a very broad molecular weight distribution, while PS3 is trimodal and has a significant amount of very high molecular weight chains. The molecular weight distributions of PS2 and PS3 are reported in Figures 4.4-b and 4.2-b. Details on the moments of the molecular weight distributions are reported in Table 4.4.

The linear moduli and molecular weight distribution of PS1, PS2 and PS3 have been measured by BASF, who also kindly provided samples for the experiments which were carried out in our facilities. All the data relative to PS140 have been produced by H. Burhin (Dynisco). The large amplitude oscillatory shear experiments were performed at 170° C in a closed pressurized chamber on a RPA2000 from Alpha Technologies, using closed bi-conical grooved plates. This same device has recently been

used by Debbaut and Burhin [52] to study the response of high density polyethylene under large amplitude oscillatory shear flows.

We now turn to the delicate task of identifying the parameters of the CRAFT model. From section 4.2, we see that there are seven parameters to identify: G_N^0, K_d, K_r, K_f, M_e, γ and b. Out of those seven parameters, the six first are related to the linear viscoelastic response, while the last one can be inferred from the number of Kuhn steps between entanglements. In order to reduce the uncertainty on the identified values of the linear parameters, we take advantage of the theoretical relations between K_d, K_r and M_e to eliminate one of the parameters. The six parameters to identify become: G_N^0, M_e, τ_e, K_f, γ and b. The new parameter τ_e, is the Rouse time of an entangled segment. The values of K_d and K_r are recovered from M_e and τ_e through the following expressions:

$$\begin{aligned} K_d &= 3\frac{\tau_e}{M_e^3} \\ K_r &= \frac{\tau_e}{M_e^2}\,. \end{aligned}$$

When dealing with samples having a broad molecular weight distribution $w(M)$, we have to discretize it into a finite number of representative molecular weights and volume fractions. For this work, we selected equally spaced (in logarithmic scale) molecular weights $M^{(i)}$ between the bounds of the molecular weight distribution. The volume fractions $\phi^{(i)}$ associated with the $M^{(i)}$s are proportional to $w(M^{(i)})$ and normalized to a unit sum. This procedure is quite simple and works well when a fine discretization can be achieved. To compute the linear response of the CRAFT model, we use a numerically fast semi-analytical method [35] which allows us to use very fine discretizations of the molecular weight distributions. This semi-analytical method is, however, irrelevant to compute the non-linear response, and we have to rely on a finite difference procedure coupled to a stiff ODE solver to solve the equations of the model for a given flow. The discretizations of the molecular weight distributions that are numerically feasible are therefore much coarser in the non-linear case than for the linear case. All the parameters of the model have been identified for fine discretizations of

Name	M_w (kD)	M_n (kD)	M_w/M_n
PS1	320	270	1.18
PS2	274	101	2.72
PS3	407	143	2.83
PS140	145	141	1.03

Table 4.1: Characteristics of the four PS samples.

the molecular weight distributions. In the non-linear regime, we use coarser discretizations that maintain low computational costs, but still predict reasonably well the linear response of the system. Among the investigated samples, we assumed PS140 and PS1 to be monodisperse at M_w, but considered the full molecular weight distribution for PS2 and PS3. We chose to use $N_{CR} = 3$ for the monodisperse samples and $N_{CR} = 5$ for PS2 and PS3.

Liu et al. [53] have shown that modern tube theories tend to underestimate the linear moduli of poorly entangled systems. The predicted plateau modulus decreases with the molecular weight, while a careful analysis of experimental data from various sources and for different materials shows a constant value. Although our model of linear viscoelasticity has not been considered by Liu et al., we have checked that it predicts the same molecular weight dependence of the moduli. In order to avoid this limitation of the model, we use in this work the value of G_N^0 identified by Liu et al. (200kPa) without trying to adjust it. As the sensitivity of the linear response of the model to the remaining four parameters is still very uneven, we adjusted the linear parameters using the linear moduli of PS140 and PS3. The number of Kuhn steps for polystyrene has been taken from [8] as $N_K = 22$, giving $b = 66$.

The full set of parameters we will be using for the CRAFT model is reported in Table 4.2. The predictions of the linear moduli of PS140 with the experimental data are reported in Fig. 4.1.

G_N^0	τ_e	M_e	K_f	γ	b
$2.0\,10^2$ [kPa]	$5.0\,10^{-4}$ [s]	15700[Dalton]	0.6	1.0	66

Table 4.2: Parameters resulting from the fitting of the model on the PS140 and PS3 data.

At first sight, we see that the linear response of PS140 is poorly predicted and that a better fit could be achieved with a higher value of G_N^0. But as PS140 only has a few number of entanglements, this sample is precisely in the regime where the model underestimates the linear moduli. The observed discrepancies are therefore to be related to the underlying linear theory of the CRAFT. Nevertheless, the LAOS experiments on PS140 have been carried out at frequencies between 0.05Hz and 0.2Hz, for which the linear moduli are well predicted. In Fig. 4.2(a), we show the experimental viscoelastic moduli for PS3 together with the model predictions for a coarse discretization of the molecular weight distribution. The coarse discretization of the molecular weight distribution is reported in Fig. 4.2(b). Looking at the linear predictions for PS3, we see that the moduli are very well reproduced by the model, excepted for high frequencies where the Rouse time seems to be underestimated. The high frequency regime of the

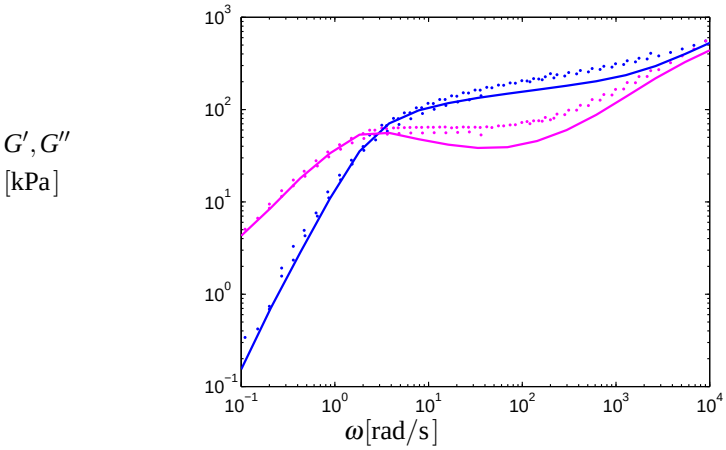

Figure 4.1: Linear viscoelastic moduli of PS140. Plain lines are the fit of the model, while the symbols are the experimental data.

loss modulus is underestimated as well.

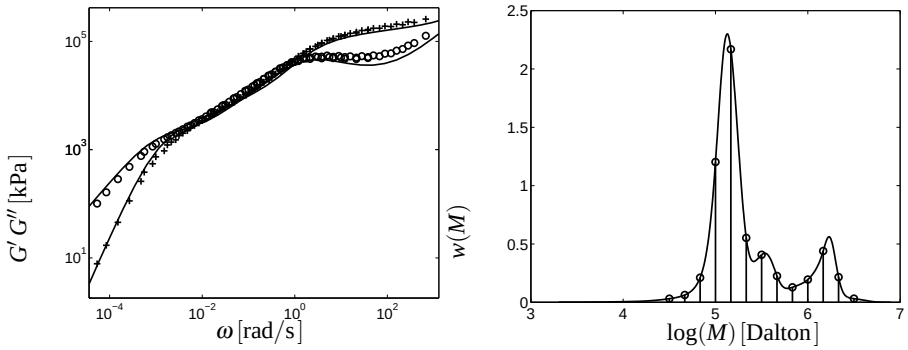

(a) (b)

Figure 4.2: (a) Linear viscoelastic moduli of PS3. Plain lines are the fit of the model, while the symbols are the experimental data. (b) Molecular weight distribution of PS3 and the discretization used for this work.

This concludes the first step of parameters identification. In Fig. 4.3, we report the predictions of the linear moduli for PS1 and PS2. The molecular weight distributions and their discretizations are shown in Fig. 4.4. For both samples, the predictions in

the high frequency regime are "wavy" but fall in the right range. These predictions could be improved by increasing the number of modes N_{CR} in the approximation of the constraint release kernel. The low frequency regime is well predicted for both samples, excepted for the storage modulus G' of PS1 which is underestimated. We believe that an accurate treatment of the high molecular weight shoulder found in the molecular weight distribution of PS1 might solve this discrepancy.

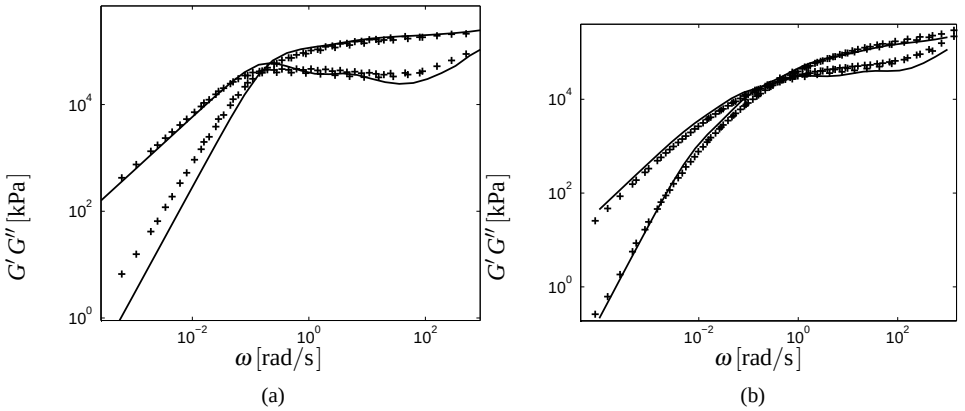

Figure 4.3: Linear viscoelastic moduli of PS1 (a) and PS2 (b). Plain lines are the model predictions, while the symbols are the experimental data.

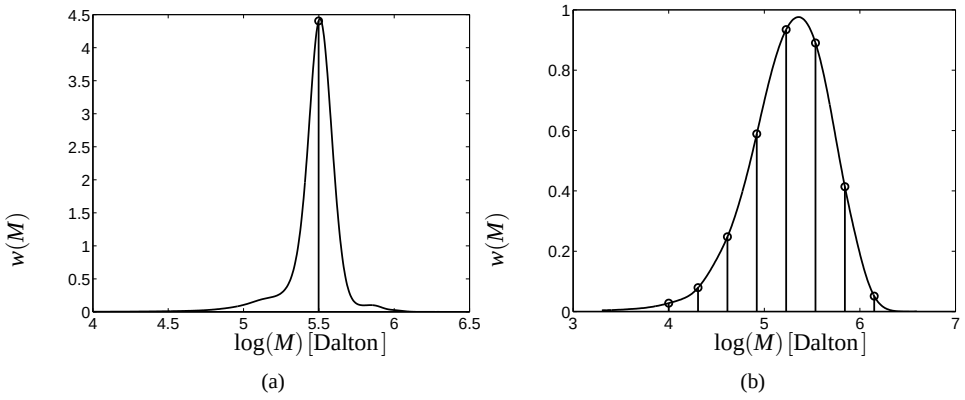

Figure 4.4: Molecular weight distributions of PS1 (a) and PS2 (b) and their discrete approximations.

4.5 LAOS predictions of PS140

In this section, we present the numerical predictions of the CRAFT model and experimental results for large amplitude oscillatory shear flows of the PS140 sample. All the predictions of the CRAFT model were computed using the parameters identified in the previous section. The only non-linear parameter is the finite extensibility parameter which has been deduced from the number of Kuhn steps between entanglements for polystyrene. We investigated LAOS flows at frequencies of $0.05\,\mathrm{Hz}$, $0.1\,\mathrm{Hz}$ and $0.2\,\mathrm{Hz}$ and maximum strains between 1 and 10. From the linear response of the model for PS140, we find the characteristic relaxation time to be $\lambda = 0.21\,\mathrm{s}$. In terms of Deborah and Weissenberg numbers, we get the following bounds:

$$\begin{aligned} 0.07 \leq \quad & \mathrm{De} \quad \leq 0.27\,, \\ 0.07 \leq \quad & \mathrm{We} \quad \leq 2.7\,. \end{aligned}$$

In Fig. 4.5, we compare the predictions and experimental data at the frequency of $0.05\,Hz$ ($\mathrm{De} = 0.07$) for four different strains. The Lissajous figures show the shear stress versus the shear rate. In those figures, the non-linearity embodied by the higher harmonics can be seen as the deviation of the shape of the loop from an ellipse. In the comparison between experiments and predictions of the model, one should keep in mind that a linear scale is used for the plots. Globally, the shape of the Lissajous loops is well predicted for all strains. From the shape of the loop in Fig. 4.5(a), we see that at this small frequency and for a maximum strain of $\gamma_0 = 2.5$ ($\mathrm{We} = 0.17$) the responses of the model and of the material are already well in the non-linear regime. At the highest strain of $\gamma_0 = 10$, the experimental Lissajous figure exhibits secondary loops, as seen in Fig. 4.5(c). The CRAFT model is able to predict both the onset and the shape of these secondary loops but, nevertheless, slightly overpredicts the shear stress.

Fig. 4.6 shows the transition from the linear to the non-linear regime as the maximum strain γ_0 increases from 1 to 10 at a frequency of $0.1\,\mathrm{Hz}$. In Fig. 4.6(a), the Lissajous loops for both the predictions and the experiments are very close to an elliptical shape. As the strain amplitude increases, we see how the loops deform and how secondary loops appear. Here again, the CRAFT model is able to predict very well the onset and the shape of the secondary loops.

The transition to the non-linear regime can be best observed in Fig. 4.7 where we show the relative magnitude of the third to the first harmonic C_3/C_1 vs. the Weissenberg number. Over one decade of We, we see how the ratio increases from a few percents to more than ten percents where it seems to saturate.

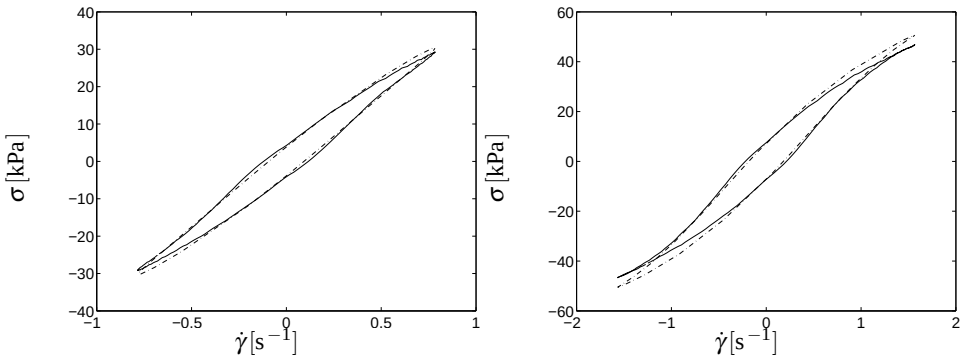

(a) $\gamma_0 = 2.5 \quad \nu = 0.05$Hz

(b) $\gamma_0 = 5 \quad \nu = 0.05$Hz

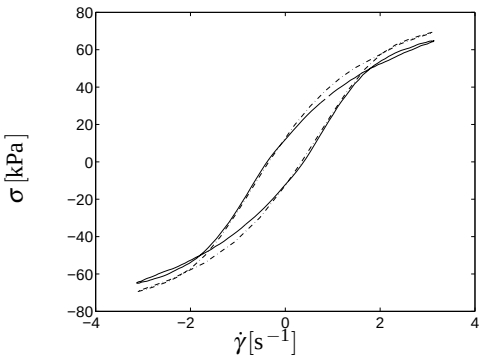

(c) $\gamma_0 = 10 \quad \nu = 0.05$Hz

Figure 4.5: Experimental results and model predictions for PS140 at 0.05 Hz, for different strains. Plain lines are the experimental results, dash-dotted lines are the model predictions.

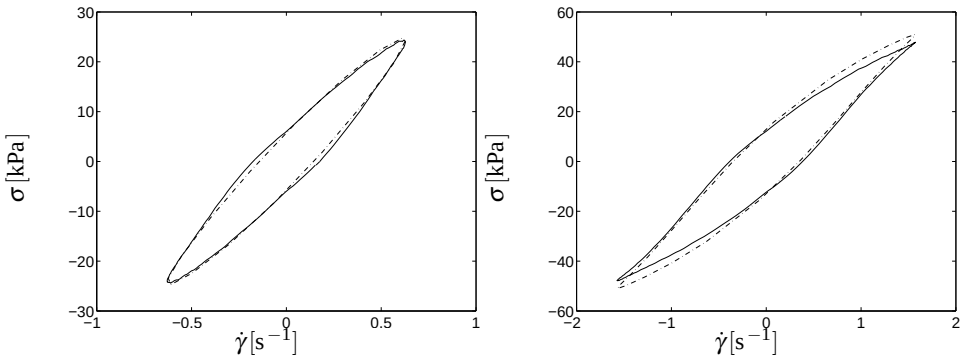

(a) $\gamma_0 = 1 \quad \nu = 0.1$Hz

(b) $\gamma_0 = 2.5 \quad \nu = 0.1$Hz

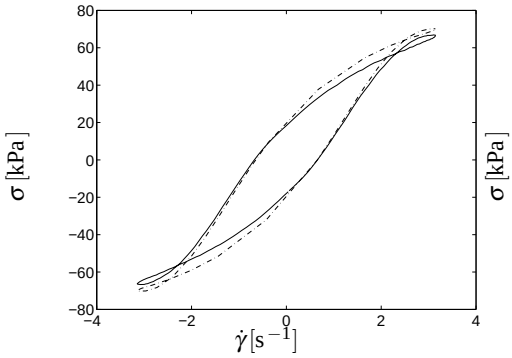

(c) $\gamma_0 = 5 \quad \nu = 0.1$Hz

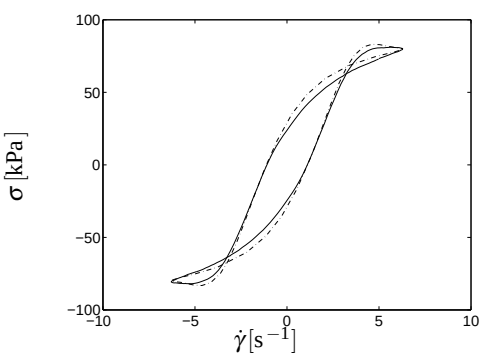

(d) $\gamma_0 = 10 \quad \nu = 0.1$Hz

Figure 4.6: Experimental results and model predictions for PS140 at 0.1 Hz, for different strains. Plain lines are the experimental results, dash-dotted lines are the model predictions.

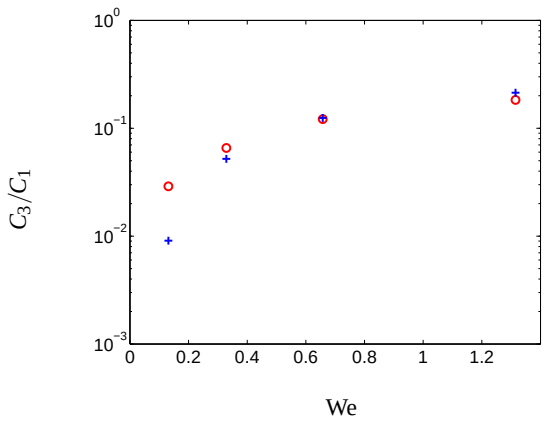

Figure 4.7: Relative magnitude of the third harmonic to the first versus the Weissenberg number for PS140 at 0.1 Hz. Comparison of the experimental data (o) with the model predictions (+).

The accurate description of the global shape of the loops tells us that not only the magnitude of the higher harmonics is well predicted but their phase as well. Table 4.3 shows the value of the three first non-zero harmonics for the experimental data and the predictions. Although we do not show the even harmonics, they are found both in the experimental and numerical data. However, their value is in both cases of the order of 0.01kPa and they belong to the experimental or numerical noise. All the components of the fundamental and of the higher harmonics are reasonably well predicted for all strains. One can, however, notice a systematic over-prediction of the magnitude of A_n, B_n and C_n at high strains. An interesting feature that is observed both numerically and experimentally is that for $\gamma_0 = 10$, the absolute value of A_3 becomes greater than A_1.

We conclude the analysis of PS140 with Fig. 4.8 where we plot the Lissajous loops for a frequency of 0.2 Hz and different γ_0. Once more, we see the ability of the CRAFT model to quantitatively predict details of the response such as the secondary loops. We do not show the details of the harmonics for this set of predictions, as the conclusions would be similar to the ones for a frequency of 0.1 Hz.

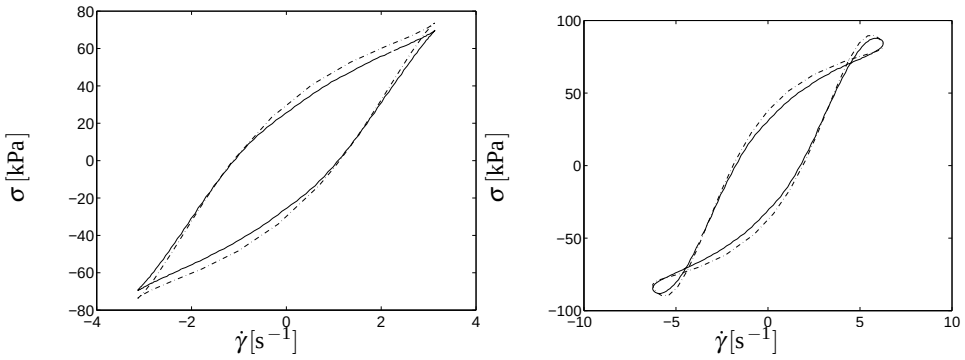

(a) $\gamma_0 = 2.5 \quad \nu = 0.2$Hz (b) $\gamma_0 = 5 \quad \nu = 0.2$Hz

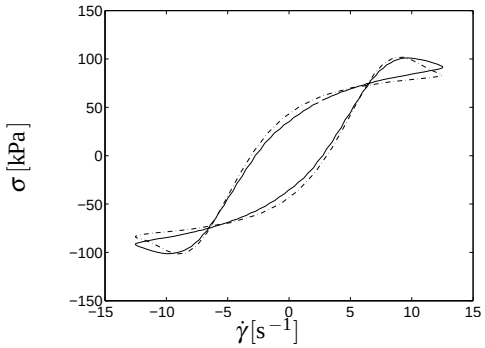

(c) $\gamma_0 = 10 \quad \nu = 0.2$Hz

Figure 4.8: Experimental results and model predictions for PS140 at $0.2\,$Hz, for different strains. Plain lines are the experimental results, dash-dotted lines are the model predictions.

		A_n[kPa]		B_n[kPa]		C_n[kPa]	
γ_0	n	Exp.	CRAFT	Exp.	CRAFT	Exp.	CRAFT
1	1	5.78	5.50	23.81	23.94	24.50	24.57
	3	-0.61	-0.22	0.37	-0.05	0.71	0.22
	5	-0.12	0.00	-0.24	0.00	0.27	0.01
2.5	1	9.28	10.15	48.82	51.89	49.69	52.87
	3	-3.18	-2.53	-0.73	-1.07	3.26	2.75
	5	0.25	0.07	-0.51	-0.20	0.57	0.21
5	1	9.76	11.38	71.91	76.69	72.57	77.53
	3	-7.28	-7.33	-4.97	-6.28	8.81	9.65
	5	1.66	1.47	-1.00	-0.91	1.94	1.73
10	1	7.98	9.66	92.51	94.11	92.85	94.60
	3	-10.19	-11.61	-13.61	-16.51	17.00	20.18
	5	5.43	6.52	0.56	1.32	5.46	6.65

Table 4.3: Amplitudes A_n and B_n of the odd harmonics (kPa) for $\nu = 0.1$ Hz. Comparison of experimental data and CRAFT predictions.

4.6 LAOS predictions of polydisperse PS samples

We now turn to the comparison between experimental data and numerical predictions of more polydisperse systems: PS1, PS2, PS3. As in section 4.4, we assume that PS1 is monodisperse and consider the discretized molecular weight distributions of Figs. 4.4 and 4.2 for PS2 and PS3. In the polydisperse case, the difficulty in analysing the results is increased by an order of magnitude as not only the non-linear relaxation mechanisms have to be understood, but the coupling between the different masses as well. We restrict therefore ourselves to the presentation of the data and of the predictions, leaving the door open for further analysis in future work.

In Fig. 4.9, we show the Lissajous figures for PS1 at 0.1 Hz and for different maximum strains. Although PS1 has a broader molecular weight distribution than PS140, it is nevertheless still quite monodisperse. As for the PS140, the CRAFT model correctly predicts the response of the sample for all γ_0. The secondary loops are well predicted and the predictions might be improved through a better discretization of the molecular weight distribution.

We now look at the ability of the CRAFT model to predict the response of polydisperse systems. In Fig. 4.10, we show the experimental data for PS2, together with the model predictions. The frequency of the LAOS flow is 0.1Hz and we consider three values for γ_0: 1, 3 and 6. For all strains, the model predicts the shape of the loops but fails to predict the secondary loops at the highest strain of $\gamma_0 = 6$.

The Lissajous figures for PS3 at a frequency of 0.1 Hz are shown in Fig. 4.11. For the two lower strains, the model correctly predicts the shape of the loop but at high strain, the stress is well overestimated by the model. This overestimation actually comes from the excessive stretch levels that the model predicts. A similar behaviour of the CRAFT model has been observed earlier [47] for bidisperse concentrated polystyrene solutions.

In Table 4.4, we compare the frequency content of the experimental data with the model predictions for $\gamma_0 = 6$ and $\nu = 0.1\,\mathrm{Hz}$. We see that all the experimental and predicted quantities agree surprisingly well, except for A_1 which seems to be the main source of discrepancies. The non-linear elastic modulus A_1 is overestimated by the model by more than a factor 2. This is again the sign of too strong an elastic response of the model, compared to the experiments.

In order to reduce the too strong elasticity of the model and the associated stretch levels, we propose to modify the finite extensibility parameter b of the CRAFT model. This parameter appears in the model in a quite arbitrary fashion through a Peterlin-like

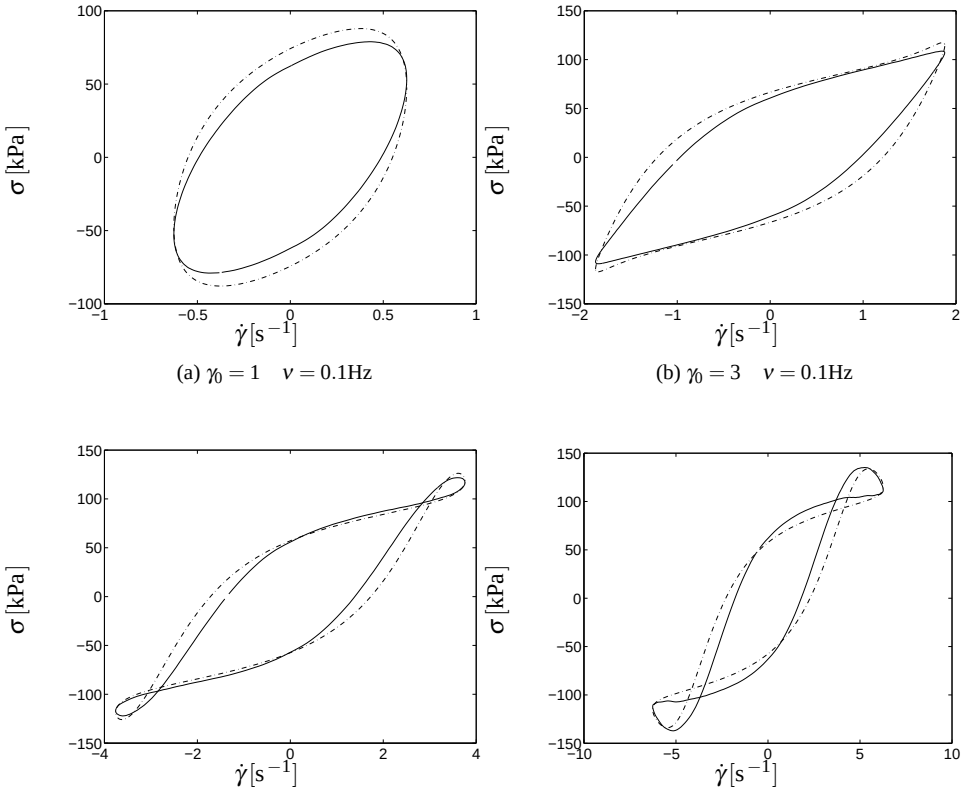

(a) $\gamma_0 = 1 \quad \nu = 0.1$Hz (b) $\gamma_0 = 3 \quad \nu = 0.1$Hz

(c) $\gamma_0 = 6 \quad \nu = 0.1$Hz (d) $\gamma_0 = 10 \quad \nu = 0.1$Hz

Figure 4.9: Experimental results and model predictions for PS1 at 0.1 Hz, for different strains. Plain lines are the experimental results, dash-dotted lines are the model predictions.

		A_n[kPa]		B_n[kPa]		C_n[kPa]	
γ_0	n	Exp.	CRAFT	Exp.	CRAFT	Exp.	CRAFT
6	1	21.17	50.80	86.96	105.33	89.50	116.94
	3	-10.25	-8.28	-3.65	-6.94	10.88	10.80
	5	1.82	1.66	-1.59	-1.54	2.42	2.27

Table 4.4: Amplitudes A_n and B_n of the odd harmonics (kPa) for $\gamma_0 = 6$ and $\nu = 0.1$ Hz. Comparison of experimental data and CRAFT predictions for PS3.

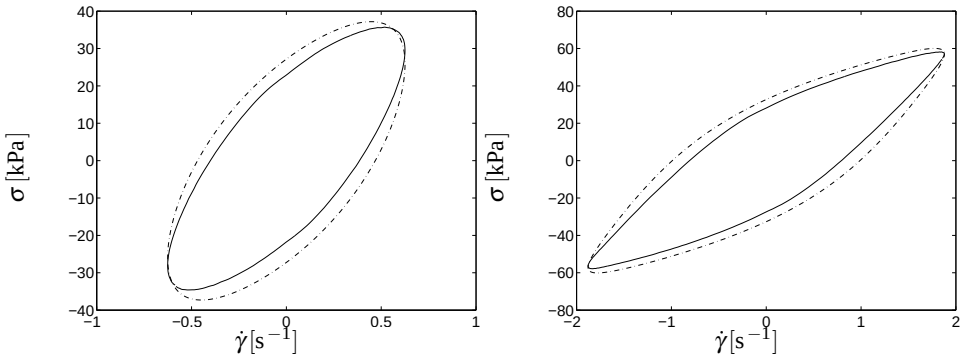

(a) $\gamma_0 = 1 \quad \nu = 0.1$Hz

(b) $\gamma_0 = 3 \quad \nu = 0.1$Hz

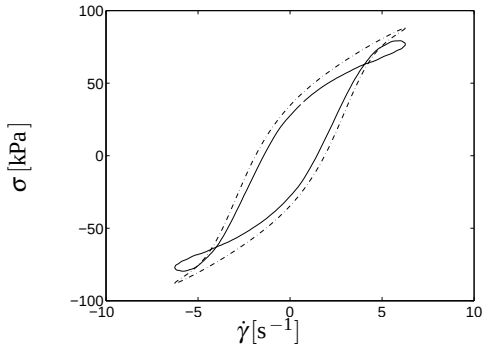

(c) $\gamma_0 = 10 \quad \nu = 0.1$Hz

Figure 4.10: Experimental results and model predictions for PS2 at $0.1\,\mathrm{Hz}$, for different strains. Plain lines are the experimental results, dash-dotted lines are the model predictions.

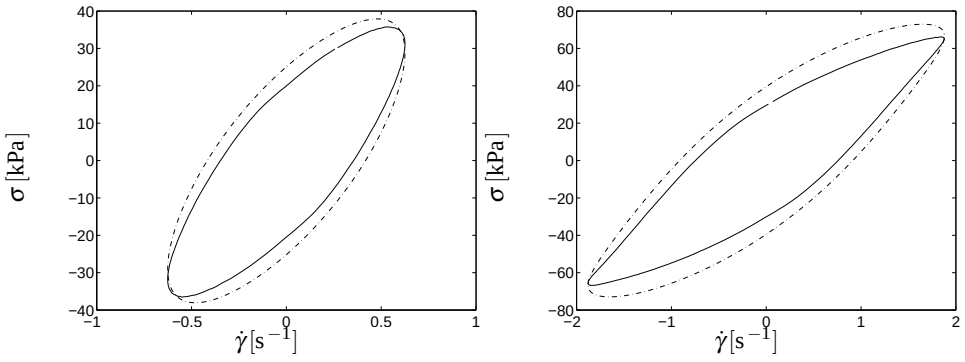

(a) $\gamma_0 = 1 \quad \nu = 0.1$Hz (b) $\gamma_0 = 3 \quad \nu = 0.1$Hz

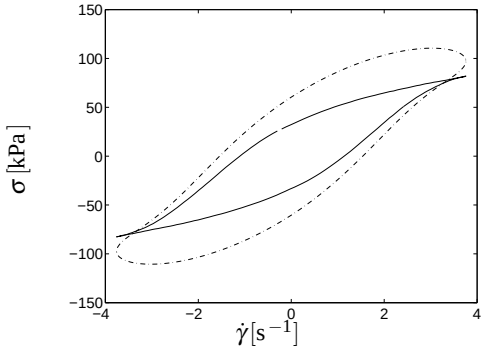

(c) $\gamma_0 = 6 \quad \nu = 0.1$Hz

Figure 4.11: Experimental results and model predictions for PS3 at 0.1 Hz, for different strains. Plain lines are the experimental results, dash-dotted lines are the model predictions.

approximation similar to that of the FENE-P model. In the case of the FENE-P model, the Peterlin approximation has been studied at length (see [3] and references therein). It has been found that the Peterlin approximation does not prevent individual chains from being stretched beyond their theoretical maximum length, therefore changing the physical meaning of the b parameter. In Fig. 4.12, we show the predictions of the CRAFT model with a finite extensibility of $b = 12$. The predictions compare somewhat better with the experiments using a small b. We do not claim that this modification provides the answer to the excessive stretch issue but it provides at least a lead for further refinements of the CRAFT model.

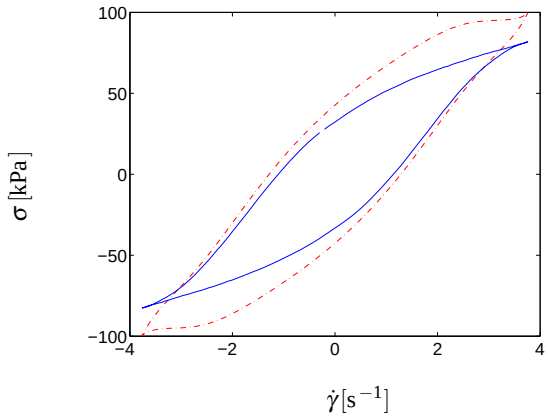

Figure 4.12: Experimental results and model predictions for PS3 at 0.1 Hz and a maximum strain of $\gamma_0 = 6$. The finite extensibility parameter has been reduced to $b = 12$. Plain line is the experimental results, the dash-dotted line is the model predictions.

4.7 Predictions in uniaxial extension

Recently, Bach et al. published [8] unique experimental data for almost monodisperse polystyrene melts. For two different masses (200k Daltons and 390k Daltons), the authors have measured the linear viscoelastic moduli, as well as the extensional stresses using a filament stretching rheometer. For both samples the data show a monotonous decrease of the Trouton ratio Tr (or equivalently the extensional viscosity) for increasing strain rates. This behaviour is even observed at strain rates greater than the reciprocal Rouse time. Moreover, the author have shown that the Trouton ratio seems to scale roughly like $\dot{\varepsilon}^{-1/2}$. Marrucci and Ianniruberto have explained [36] how these finding contradict most of the constitutive equations for entangled polymers. They

have suggested an additional relaxation mechanism involving an interchain repulsive mechanism to explain the observed $\dot{\varepsilon}^{-1/2}$ dependence of the Trouton ratio.

We have shown [47] that when the finite extensibility is small enough, the CRAFT model predicts the Trouton ratio to be a monotonously decreasing function of the extension rate. In this regime, the Trouton ratio does not exactly scale like $\dot{\varepsilon}^{-1/2}$ as the predicted curve exhibits some kinks. The average scaling is nevertheless close to $-1/2$.
Using the parameters identified in Sec. 4.4, we wish to predict the linear viscoelastic moduli and the Trouton ratio of PS200 and PS300, as measured by Bach et al. [8]. As the experiments of Bach et al. were performed at 130°C, we need to shift the parameters of the CRAFT from 170°C to 130°C. We consider here a shift of the elementary time scale τ_e only and ignore any scaling of the modulus G_N^0. The temperature shift factors a_T are computed from the WLF equation exactly as reported by Bach et al. :

$$\log a_T = \frac{-c_1^0 (T - T_0)}{c_2^0 + (T - T_0)} , \tag{4.23}$$

where $c_1^0 = 8.86$, $c_2^0 = 101.6K$, $T_0 = 136.5$°C, and T is the temperature in °C. We find that, at 130°C, we have to use $\tau_e = 0.317$.

In Fig. 4.13, we compare the linear viscoelastic moduli predicted by the CRAFT model at 130°C to the experimental data [8]. For both samples, the agreement is very good, except at intermediate frequencies, where the CRAFT model predicts too deep a local minimum of the loss modulus.

For predicting the Trouton ratio, we consider two different values for the finite extensibility parameter:

- $b = 66$ as derived from the number of Kuhn steps between entanglements,
- $b = 12$ as we know that small values of b yield an ever decreasing Trouton ratio.

Fig. 4.14 compares the predictions of the CRAFT model for both values of b with the experimental data. At low strain rates, the CRAFT model predicts the theoretical asymptotic value of 3 for the Trouton ratio. For $b = 66$, the data agree with the predictions up to moderate extension rates. At higher strain rates, where the chains become stretched, we observe a deviation of the predictions from the data as the stress rises until full extension is reached. On the other hand, we see that for $b = 12$, the predictions agree with the data for all extension rates. The only discrepancy is found at intermediate extension rates, where the predictions for PS200 are too extension thinning.

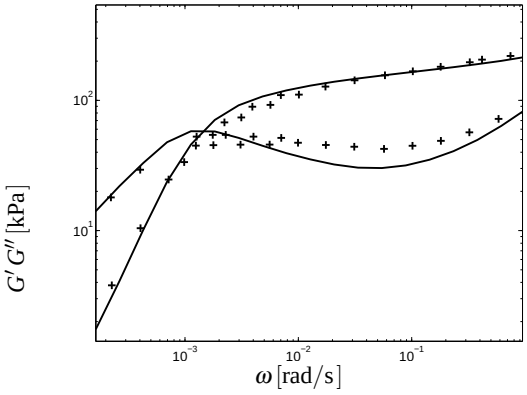

(a) PS200

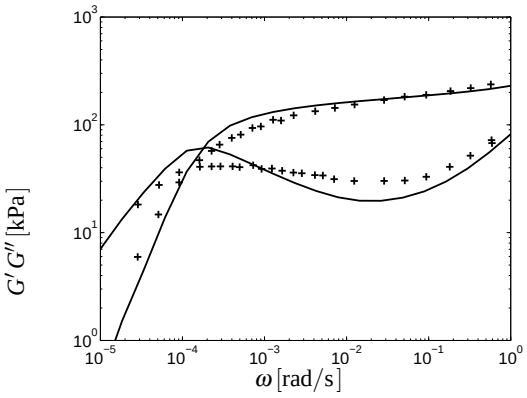

(b) PS390

Figure 4.13: Comparison of the measured and predicted linear moduli for PS200 and PS390 at 130° C. Plain lines are the model predictions, symbols are the experimental results [8].

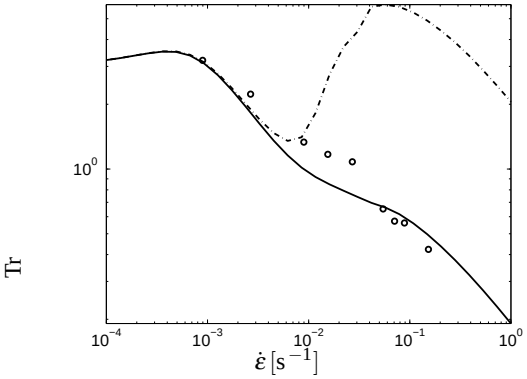

(a) PS200

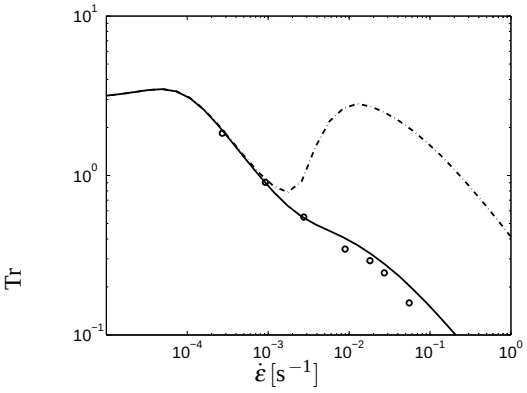

(b) PS390

Figure 4.14: Comparison of the measured and predicted Trouton ratio for PS200 and PS390 at 130° C. Plain lines are the model predictions for $b = 12$, dash-dotted lines are the model predictions for $b = 66$, symbols are the experimental results [8].

4.8 Conclusions

We have shown that the CRAFT model can quantitatively predict the LAOS response of mono- and poly-disperse polystyrene samples using only a single set of parameters identified from the linear viscoelastic response of a subset of the samples. For the monodisperse samples, the agreement between the data and the predictions is very good, and highly non-linear features can be quantitatively described. These include the higher harmonics of the spectral decomposition of the shear stress and the occurence of secondary loops in the shear stress versus shear rate Lissajous plots. We believe that the CRAFT model is highly appropriate to study the LAOS response of linear entangled polymers, as non-linear features can be related to the linear parameters of the model and to the built-in relaxation mechanisms.

The LAOS response of the polydisperse samples, which contain a fraction of high molecular weight chains, is well described at low and moderate Weissenberg numbers. At high Weissenberg numbers, the model exhibits too strong an elastic response, which we connect to chain stretch effects. By artificially decreasing the finite extensibility parameter of the CRAFT model, we somewhat improve the predictions in this highly non-linear regime.

In the case of uniaxial extension, we find that when finite extensibility is reduced, the CRAFT model can predict, using the same parameters, the extensional viscosity data of Bach et al. [8] without any modification to the constitutive equation.

Chapter 5

A constitutive equation for entangled linear polymers inspired by reptation theory and consistent with non-equilibrium thermodynamics

5.1 Foreword

In this chapter, we present some early contribution in which we show how a constitutive equation can be analyzed and then phenomenologically improved using the single generator bracket formalism of non-equilibrium thermodynamics [44]. Although the investigated model has been supersed by newer ones, we believe that a similar work could be carried on the CRAFT model, yielding improved predictions in the non-linear regime. This chapter might therefore be considered as a source of inspiration for those interested in further improving the CRAFT model.

5.2 Introduction

Since the introduction by de Gennes [11] of the reptation picture, a number of successful molecular theories have been able to describe with increasing accuracy the linear rheology of entangled linear polymers. The original idea is to consider the polymer chain confined in a tube formed by the topological constraints, or entanglements, between the chain and the surrounding polymer chains. The dominant relaxation mechanism comes from the reptation of the chain out of the confining tube. Considering chain length fluctuations, it is possible to predict with reasonable accuracy the linear viscoelastic properties of linear monodisperse polymers. The prediction of non-linear rheological properties is far less accurate however. In the classical Doi-Edwards (DE) theory [12], the tube is deformed affinely by the flow and its segments are gradually destroyed and renewed as the chain slowly reptates out of the tube. It is also assumed that the chain-retraction mechanisms are so fast that the chain always has its equilibrium length. Among the successes of the classical DE theory, we find the prediction of the plateau modulus and of the damping function in response to a step strain. The DE model also predicts a non-zero second normal stress difference in shear flows. There are nevertheless major features that the DE model fails to predict, even qualitatively [26]:

1. The transient response of DE in startup of shear flow has an overshoot in the shear stress but none for the first normal stress difference, while large overshoots both in shear and normal stresses are observed experimentally. Furthermore, DE predicts the overshoot in shear stress to occur at a strain which is independent of the shear rate, which is again incompatible with experimental observations.

2. For steady-state shear flows, DE predicts the shear stress to be a non-monotonic function of the shear rate, which is a constitutive instability. It also predicts the first normal stress to approach a constant value as the shear rate increases. Experimental data seem to show an almost constant but slowly increasing shear stress and an ever-increasing first normal stress difference.

3. For small shear deformations, DE underestimates the value of the normal stress ratio $-N_2/N_1$: its zero-strain limit is $1/7 = 0.142$, while experiments show values around 0.25 [54].

It has been shown [26] that the first discrepancy can be removed at high shear rates by consideration of chain stretch effects. Several models including this feature have been proposed. Recently, Ianniruberto and Marrucci [39] suggested that a mechanism called Convective Constraint Release (CCR) might explain the observed monotonic growth of the shear stress. This mechanism takes into account the convection of the

entanglements along the polymer chain due to the flow. At high flow rate ($\tau_d \dot{\gamma} > 1$, where τ_d is the reptation time constant), the convective removal of entanglements induces a faster relaxation of the chain at increasing shear rates, thus explaining the observed growth of the shear stress. Marrucci et al. [55] also suggested that the discrepancy concerning the normal stress ratio might come from an inappropriate strain measure in the basic DE theory. They showed that a new strain measure, derived from force balance requirements at the nodes of a simple 3-chain network, correctly predicts the correct value for the normal stress ratio in a step strain experiment. The CCR mechanism and the new strain measure have both been implemented recently by Marrucci et al. [9] in the so-called MGI constitutive equation. The latter has an integral form which is very well approximated by a differential constitutive equation. The behaviour of the MGI model in complex flows has been studied recently by Wapperom and Keunings [56].

Recent constitutive equations such as the MGI model introduce an additional coupling between the velocity gradient and the conformation variables, whose thermodynamic consistency needs to be verified. In the present work, using the single generator bracket formalism of non-equilibrium thermodynamics [44], we build a thermodynamically consistent constitutive equation of the differential type for linear entangled polymers. The starting point of our developments is the MGI differential model. We show that non-equilibrium thermodynamics suggests the introduction of an additional term in the relation between the stress and the conformation variables of the MGI model. The proposed constitutive equation has an additional parameter and contains the consistent MGI model as a particular case. Its behaviour in steady and transient shear flow is shown to be in qualitative agreement with experimental observations.

5.3 Non-equilibrium thermodynamics

The compatibility of constitutive equations with non-equilibrium thermodynamics, as developed through the single generator bracket [44] or the two generator GENERIC [57] formalisms, ensures the satisfaction of symmetry constraints for the coupling parameters describing the dissipation in the linear limit (Onsager/Casimir reciprocal relation [58]). It also ensures a non-negative entropy production.

We consider differential constitutive equations for incompressible isothermal flows in the context of the single generator bracket formalism [44] of non-equilibrium thermodynamics. In order to describe the behaviour of a fluid with an internal microstructure, one has few but important choices to make:

- The variables of the problem. In addition to the velocity v_α, we shall consider here a single second-order conformation tensor $c_{\alpha\beta}$ as an internal parameter describing the microstructure of the fluid. The physical meaning of the selected variables alone dictates the conservative convective component of the constitutive equation. In this case, the conservative part of the system follows Euler's equations of hydrodynamics with an additional component depending on $\mathbf{c}$, and an evolution equation given in the form:

$$\overset{\triangledown}{\mathbf{c}} = 0 \,,$$

  where $\overset{\triangledown}{(\cdot)}$ is the upper-convected time derivative [59]. Therefore, in the absence of dissipation, $\mathbf{c}$ can be interpreted as the Finger strain tensor, the governing equations reducing to those for large deformation elasticity [60].

- The extended Helmholtz free energy density a of the system as a function of the selected variables and possibly their gradients. Here, we consider that the gradient of the conformation tensor does not influence the free energy. At equilibrium, a reduces to the thermodynamic free energy, which is obtained when a is minimised with respect to the internal parameters. Away from equilibrium, the gradient of a is, in general, non-zero and acts like a thermodynamic driving force.

- The structure of dissipative phenomena, related for example to CCR and the relaxation of the microstructure.

For a viscoelastic constitutive model described by a single second order internal tensor parameter, the addition of dissipative phenomena described by the lowest possible order (quadratic) interaction terms yields the following general constitutive equation [44]:

$$\begin{aligned} \frac{\partial c_{\alpha\beta}}{\partial t} &= -v_\gamma \nabla_\gamma c_{\alpha\beta} + c_{\alpha\gamma}\nabla_\gamma v_\beta + c_{\gamma\beta}\nabla_\gamma v_\alpha \\ &\quad -\Lambda_{\alpha\beta\gamma\varepsilon}\frac{\partial a}{\partial c_{\gamma\varepsilon}} + L_{\alpha\beta\gamma\varepsilon}\nabla_\gamma v_\varepsilon \,, \end{aligned} \tag{5.1}$$

$$\sigma_{\alpha\beta} = 2c_{\beta\gamma}\frac{\partial a}{\partial c_{\alpha\gamma}} + L_{\alpha\beta\gamma\varepsilon}\frac{\partial a}{\partial c_{\gamma\varepsilon}} + Q_{\alpha\beta\gamma\varepsilon}\nabla_\gamma v_\varepsilon \,. \tag{5.2}$$

Equation (5.1) describes the time evolution of the conformation tensor ($c_{\alpha\beta}$), while eq. (5.2) expresses the stress as a function of the system's variables and of the derivative of the extended free energy with respect to these variables. On the first line of eq. (5.1), we recognise the upper-convected time derivative of the conformation tensor, while on the second line we find two dissipative terms. The first accounts for relaxation phenomena, while the second is a mixed term leading e.g. to the mixed convected time

derivative in the Johnson/Segalman fluid model [44]. The three terms on the right-hand side of eq. (5.2) can be respectively interpreted as a conservative term, similar to what is obtained in non-linear elasticity, a mixed correction term, and a viscous dissipation term. The fourth-order tensors $\Lambda_{\alpha\beta\gamma\varepsilon}$, $L_{\alpha\beta\gamma\varepsilon}$ and $Q_{\alpha\beta\gamma\varepsilon}$ arise in the limit of linear irreversible thermodynamics [61] and come from a first-order approximation of general dissipative phenomena. These tensors are phenomenological and can depend upon the variables of the problem but *not* their derivatives. They also need to be invariant to the following permutations of indices:

$$\alpha\beta\gamma\varepsilon \leftrightarrow \beta\alpha\gamma\varepsilon \leftrightarrow \alpha\beta\varepsilon\gamma \leftrightarrow \beta\alpha\varepsilon\gamma\,. \tag{5.3}$$

Appropriate choices for the extended free energy and the dissipative structure yield well known constitutive equations such as the UCM, Johnson/Segalman or Giesekus models [44].

At this point, it should be noticed that eqs. (5.1) and (5.2), as presented in [44], were obtained for a tensor $L_{\alpha\beta\gamma\varepsilon}$ symmetric with respect to an exchange of the first two by the last two indices, $\alpha\beta \leftrightarrow \gamma\varepsilon$. In appendix 1, we show that these equations remain valid for a general tensor $L_{\alpha\beta\gamma\varepsilon}$ where this symmetry is not obeyed.

In the following sections, we shall first present the physical phenomena we wish to include in the constitutive equation, and then we shall consider the way to express these in a form compatible with the single generator bracket formalism.

5.4 Convective constraint release and force balance

It is not a surprise that constitutive equations that consider reptation as the only source of dissipation are unable to predict a monotonic growth of the steady-state shear stress as a function of shear rate. Indeed, at increasing flow rates, the thermal relaxation terms of these equations can be considered frozen, compared to the convective part. The relatively slow relaxation of the tube segments cannot counteract alignment in the shear direction. This explains why one observes a decrease of the shear stress at increasing shear rates greater than $1/\tau_d$ [39].

Convective Constraint Release (CCR) takes into account the removal of entanglements due to their convection by the flow along the polymer chain. In this fashion, entanglements are destroyed once they are convected past the end of the chain. Considering that classical relaxation and flow-induced CCR operate in parallel, it is possible to sum their frequencies. With the assumption that the tube renewal frequency caused by CCR is proportional to the rate of convection along the tube, Ianniruberto

and Marrucci [39] obtained a modified relaxation time τ, defined as:

$$\frac{1}{\tau} = \frac{1}{\tau_d} + \beta \mathbf{k} : \langle \mathbf{uu} \rangle, \tag{5.4}$$

where τ_d is the DE disengagement time, $\langle \mathbf{uu} \rangle$ the orientation tensor, $\mathbf{k}$ is the transpose of the velocity gradient and β denotes an adjustable scalar parameter. Although a value for β of unity seems more natural, it has been argued [39] that β should be somewhat greater than unity. One should also notice that $\mathbf{k} : \langle \mathbf{uu} \rangle$ is very similar to the rate of tube stretch found in models like those presented in [26]. Ianniruberto and Marrucci showed [39] that the CCR relaxation mechanism induces a monotonic growth of the shear stress and improves the agreement of the model with the Cox-Merz rule.

In order to correct the step strain predictions of DE, Marrucci et al. [55] suggested that a strain measure taking into account some requirement of force balance at the node of the entangled network should be adopted. Using a simple three-chain cubic network, they proposed a new strain measure that automatically fulfils the force balance at the entanglements of the network. For an elastic (non-relaxing) network, the new measure is:

$$\tilde{\mathbf{Q}} = \frac{\mathbf{C}^{1/2}}{\mathrm{tr}\left(\mathbf{C}^{1/2}\right)}, \tag{5.5}$$

where $\mathbf{C}$ is the Finger tensor. For step strain deformations, just after the deformation, and before relaxation starts, the stress tensor is then given by:

$$\sigma = 6G_N^{(0)}\left(\tilde{\mathbf{Q}} - \frac{1}{3}\delta\right), \tag{5.6}$$

where $G_N^{(0)}$ is the plateau modulus and δ is the unit tensor.

5.5 Constructing the model

Relating the concepts of force balance and CCR to the bracket formalism is not straightforward and requires some insight. In this section, we present this process in a top-down approach.

Having selected a non-negative definite, symmetric second-order tensor $\mathbf{c}$ as an additional internal variable, we see from equations (5.1) and (5.2) that the remaining building blocks are:

1. The specification of the extended Helmoltz free energy density a,

2. The development of the three fourth-order tensors Λ, $\mathbf{L}$ and $\mathbf{Q}$.

Since the tensor $\mathbf{Q}$ accounts for viscous dissipation, its contribution will be neglected as we are interested in microstructure-induced stress. From eq. (5.1), we find that the CCR mechanism described earlier can only be incorporated in the model through the mixed term $L_{\alpha\beta\gamma\varepsilon}\nabla_\gamma v_\varepsilon$. Indeed, in the lowest order expansion for the dissipation, only this term can provide a coupling between the velocity and the conformation tensor other than the upper-convected time derivative. Additional constraints between Λ and $\mathbf{L}$ will also appear from eq. (5.4). In the absence of dissipative phenomena, the only degrees of freedom lie in the free energy density. This is where we incorporate the new strain measure (5.5).

5.5.1 Conservative part

In the absence of dissipative phenomena, the constitutive equation is uniquely determined by the form of the free energy density. From eq. (5.1) we see that the evolution equation of the conformation tensor $\mathbf{c}$ is compatible with its interpretation as the Finger strain tensor. In the absence of dissipation ($\Lambda = \mathbf{L} = 0$), equating the remaining non-vanishing parts of the right-hand side of eqs.(5.2) and (5.6) implies that the free energy density a satisfies:

$$6G_N^{(0)}\left(\frac{\mathbf{c}^{1/2}}{\mathrm{tr}\,\mathbf{c}^{1/2}} - \frac{1}{3}\delta\right) = 2\mathbf{c}\frac{\partial a}{\partial \mathbf{c}}\,, \tag{5.7}$$

or

$$\frac{\partial a}{\partial \mathbf{c}} = 3G_N^{(0)}\left(\frac{\mathbf{c}^{-1/2}}{\mathrm{tr}\,\mathbf{c}^{1/2}} - \frac{1}{3}\mathbf{c}^{-1}\right). \tag{5.8}$$

This expression allows us to use the thermodynamic formalism in order to describe the same strain measure as proposed by Marrucci et al. Integrating eq. (5.8), we find the following expression for the extended free energy density:

$$a(\mathbf{c}) = 6G_N^{(0)}\left\{\ln(\mathrm{tr}\,\mathbf{c}^{1/2}) - \frac{1}{6}\ln(\det\mathbf{c})\right\}\,. \tag{5.9}$$

A closer look at this expression shows that it is independent of the magnitude of $\mathbf{c}$. Indeed, if we substitute $\mathbf{c}$ for $\gamma\mathbf{c}$ in eq. (5.9), γ being a positive scalar, we get:

$$\begin{aligned} a(\gamma\mathbf{c}) &= 6G_N^{(0)}\left\{\ln(\gamma^{1/2}\mathrm{tr}\,\mathbf{c}^{1/2}) - \frac{1}{6}\ln(\gamma^3\det\mathbf{c})\right\} \\ &= 6G_N^{(0)}\left\{\frac{1}{2}\ln\gamma + \ln(\mathrm{tr}\,\mathbf{c}^{1/2}) - \frac{1}{2}\ln\gamma - \frac{1}{6}\ln(\det\mathbf{c})\right\} \\ &= a(\mathbf{c})\ . \end{aligned}$$

As a is independent of the magnitude of $\mathbf{c}$, and as $\mathbf{c}$ is by definition equal to the unit tensor at equilibrium, a should be minimised for $\mathbf{c} = \gamma\delta$. For these values indeed, the gradient $\frac{\partial a}{\partial \mathbf{c}}$ vanishes, while the second-order derivative of a reduces to:

$$\frac{\partial^2 a}{\partial \mathbf{c}^2}_{\mathrm{eq}} = \frac{G_N^{(0)}}{3\gamma^4}\delta\delta\ ,$$

which is a positive definite fourth-order tensor. Equation (5.9) describes therefore a thermodynamically valid free energy.

We can better understand the meaning of this free energy density if we rewrite it as:

$$a(\mathbf{c}) = -G_N^{(0)}\ln\det\left(\frac{\mathbf{c}^{1/2}}{\mathrm{tr}\,\mathbf{c}^{1/2}}\right)^2\ . \tag{5.10}$$

This shows that all stretching effects have been neglected through the scaling with the trace of $\mathbf{c}^{1/2}$, and only an entropic orientational contribution remains (See Eq. 13C.7-7 p.209 in [62], with $\alpha = 3\frac{\mathbf{c}}{\mathrm{tr}\,\mathbf{c}}$). The modelling assumption is thus that the orientational distribution of the tube segments is described by $\mathbf{c}^{1/2}$ rather than by $\mathbf{c}$. As taking the square root of $\mathbf{c}$ only changes the eigenvalues of the tensor, this can be interpreted as a reweighting of the eigenvectors of the conformation tensor.

5.5.2 Dissipative part

In the modelling of dissipative phenomena, we shall first focus on the relaxation tensor Λ of eq. (5.1). Since the extended free energy density (5.9) is independent of the magnitude of $\mathbf{c}$, it is also most natural to keep this feature here and obtain an evolution equation for $\mathbf{c}$ that would also be independent of its magnitude. Therefore, comparing equations (5.1) and (5.8), we find that Λ should scale like $\mathbf{c}^2$. We shall then define two

different relaxation tensors that satisfy the symmetry relations (5.3):

$$\Lambda^{(1)}_{\alpha\beta\gamma\varepsilon} = \frac{c^{1/2}_{\delta\delta}}{6\tau_d G^{(0)}_N}\left(c^{1/2}_{\alpha\gamma}c_{\beta\varepsilon}+c^{1/2}_{\alpha\varepsilon}c_{\beta\gamma}+c^{1/2}_{\beta\gamma}c_{\alpha\varepsilon}+c^{1/2}_{\beta\varepsilon}c_{\alpha\gamma}\right), \tag{5.11}$$

$$\Lambda^{(2)}_{\alpha\beta\gamma\varepsilon} = \frac{3}{6\tau_d G^{(0)}_N}\left(c_{\alpha\gamma}c_{\beta\varepsilon}+c_{\alpha\varepsilon}c_{\beta\gamma}+c_{\beta\gamma}c_{\alpha\varepsilon}+c_{\beta\varepsilon}c_{\alpha\gamma}\right). \tag{5.12}$$

The tensor $\Lambda^{(1)}$ has been constructed to obtain a constitutive equation as close as possible to the MGI differential model proposed in [9] (see appendix 2). On the other hand, the tensor $\Lambda^{(2)}$ can be seen in a naive way as the most natural tensor expression with a scaling like $\mathbf{c}^2$. This relaxation tensor is actually identical to the one found in the Giesekus model with the mobility factor equal to unity (see [44] p.265 with $\alpha = 1$). It is obtained from $\Lambda^{(1)}$ using a mobility tensor equal to $\frac{3\mathbf{c}^{1/2}}{\mathrm{tr}\mathbf{c}^{1/2}}$ (see [44], pp 252-256). The pre-factors in eqs. (5.11-5.12) are such as to obtain the right linear viscoelastic limit and to keep the physical meaning of the parameters τ_d and $G^{(0)}_N$ unchanged. Finally, we propose the relaxation tensor Λ to be a linear combination of $\Lambda^{(1)}$ and $\Lambda^{(2)}$:

$$\Lambda_{\alpha\beta\gamma\varepsilon} = (1-\alpha)\Lambda^{(1)}_{\alpha\beta\gamma\varepsilon} + \alpha\Lambda^{(2)}_{\alpha\beta\gamma\varepsilon}. \tag{5.13}$$

The phenomenological parameter α plays a role similar to that of the mobility factor in the Giesekus model [44].

5.5.3 Introducing convective constraint release

The dissipative term induced in eq. (5.1) by the Λ tensor is independent of the velocity gradient $\mathbf{k}^T$. The CCR mechanism (5.4), however, introduces an additional linear dependence on $\mathbf{k}$. The only way that this can originate within the quadratic dissipation formalism is from a non-vanishing $\mathbf{L}$ tensor in (5.1). Moreover, by comparing eqs. (5.1) and (5.4), we find that $\mathbf{L}$ must have the following form:

$$L_{\alpha\beta\gamma\varepsilon} = -J(\mathbf{c},\mathbf{k})\tau_d\beta\Lambda_{\alpha\beta\delta\phi}\frac{\partial a}{\partial c_{\delta\phi}}\frac{c^{1/2}_{\gamma\varepsilon}}{c^{1/2}_{\theta\theta}} \equiv J(\mathbf{c},\mathbf{k})L^{\star}_{\alpha\beta\gamma\varepsilon}, \tag{5.14}$$

where $J(\mathbf{c},\mathbf{k})$ is an appropriate *switch* function which is equal either to 1 or zero (see appendix 1).

At this time, we have to remark that, in contrast to the original quadratic dissipation theory (as described by equations (5.1) and (5.2)), $\mathbf{L}$ is found here to be a function of the Volterra derivative of the Hamiltonian with respect to the internal parameter $\mathbf{c}$. Indeed, this is the only way through which the CCR mechanism can be introduced into

the non-equilibrium formalism, i.e. by requiring a higher order non-linearity in the dissipation mechanism introduced by **L**. What we therefore propose here is an “ansatz”, sort of a mean field theory approach, with the form for **L** being suggested by rather than dictated from non-equilibrium thermodynamics (since the Onsager-Casimir relations from which the original term introduced by **L** in the dissipation originates are strictly applicable only for a quadratic dissipation close to the equilibrium limit). On the other hand, what non-equilibrium thermodynamics requires is that the overall rate of entropy production be non-negative. Since a non-symmetric **L** contributes to the entropy production (see appendix 1) and this contribution can be either positive or negative, and since it is not in general easy to a-priori tailor the other contributions to guarantee in all cases an overall positive entropy production, we take the further step here to also propose a corrective multiplicative factor $J(\mathbf{c},\mathbf{k})$ which acts as a "switch function" selectively turning the **L** term off when its individual contribution to the rate of entropy production is negative (see appendix 1 for a full expression). This is certainly allowed, since **L** corresponds to a higher non-linearity anyhow. It only risks to be too conservative (eliminating CCR under conditions under which it may have been thermodynamically admissible), but we propose it anyhow for two reasons:

1. it is a thermodynamically-induced correction that it is relatively easy to implement and when implemented guarantees the thermodynamic consistency of the model,

2. it is a correction that is applicable only rarely (most notably: during flow reversal) since in most flows, and certainly all the simple shear flows examined in the present work, this correction is not necessary as the corresponding rate for the entropy production term is positive (and thus $J(\mathbf{c},\mathbf{k}) = 1$) .

Finally, we note that a similar correction was found necessary to be introduced in the original MGI model [63] in connection to the physical interpretation of the CCR as a correction to the relaxation time—for consistency, such a correction needs to be taken into account only when it is positive; if negative, it risks to make the overall relaxation time negative which is aphysical. However, note that here, and in contrast to the original MGI model, we have this on-off switch affecting both the stress and the evolution equation for **c** in a concerted fashion.

A consequence of the introduction of a non-vanishing tensor **L** is that it brings an additional term in the stress equation (5.2). This term is of similar nature to the one that has to be introduced in the Johnson/Segalman model when a mixed time derivative is used instead of the upper-convected derivative. The presence of this term introduces significant changes in predictions for the extra-stress tensor.

5.6 Completed model

Combining all the building blocks presented above, we can derive a full model, which is thermodynamically-consistent and involves both the new strain measure and the Convective Constraint Release mechanism of the MGI model.

After substitution of eq. (5.14) into eqs. (5.1) and (5.2), the model reads:

$$\begin{aligned}\frac{\partial c_{\alpha\beta}}{\partial t} &= -v_\gamma \nabla_\gamma c_{\alpha\beta} + c_{\alpha\gamma}\nabla_\gamma v_\beta + c_{\gamma\beta}\nabla_\gamma v_\alpha \\ &\quad - \left(1 + J(\mathbf{c},\mathbf{k})\tau_d \beta \frac{c^{1/2}_{\delta\phi}}{c^{1/2}_{\theta\theta}} \nabla_\delta v_\phi\right) \Lambda_{\alpha\beta\gamma\varepsilon} \frac{\partial a}{\partial c_{\gamma\varepsilon}} , \qquad (5.15)\\ \sigma_{\alpha\beta} &= 2c_{\beta\gamma}\frac{\partial a}{\partial c_{\alpha\gamma}} - J(\mathbf{c},\mathbf{k})\tau_d\beta\Lambda_{\alpha\beta\delta\phi}\frac{\partial a}{\partial c_{\delta\phi}}\frac{c^{1/2}_{\gamma\varepsilon}}{c^{1/2}_{\theta\theta}}\frac{\partial a}{\partial c_{\gamma\varepsilon}} , \qquad (5.16)\end{aligned}$$

with a, Λ and $J(\mathbf{c},\mathbf{k})$ defined respectively by eqs. (5.9), (5.13) and (5.23). On the second line of eq. (5.15), we clearly see that all dissipative phenomena will occur with an apparent relaxation time corresponding to CCR, while the new strain measure appears in the first term of eq. (5.16).

In the sequel, we focus on two limiting cases of the proposed model, obtained for $\alpha = 0$ and 1. For $\alpha = 0$, the model reads:

$$\begin{aligned}\overset{\triangledown}{\mathbf{c}} &= -2\left(\frac{1}{\tau_d} + J(\mathbf{c},\mathbf{k})\beta\mathbf{k} : \frac{\mathbf{c}^{1/2}}{\mathrm{tr}\,\mathbf{c}^{1/2}}\right)\mathrm{tr}\,\mathbf{c}^{1/2}\left(\frac{\mathbf{c}}{\mathrm{tr}\,\mathbf{c}^{1/2}} - \frac{1}{3}\mathbf{c}^{1/2}\right) , \qquad (5.17)\\ \sigma &= 6G_N^{(0)}\left(\frac{\mathbf{c}^{1/2}}{\mathrm{tr}\,\mathbf{c}^{1/2}} - \frac{1}{3}\delta\right) \\ &\quad \cdot \left(\delta - J(\mathbf{c},\mathbf{k})\beta\left(3 - \frac{1}{3}\mathrm{tr}\,\mathbf{c}^{1/2}\mathrm{tr}\,\mathbf{c}^{-1/2}\right)\frac{\mathbf{c}^{1/2}}{\mathrm{tr}\,\mathbf{c}^{1/2}}\right) . \qquad (5.18)\end{aligned}$$

It can be proved (see appendix 2) that this model is almost equivalent to the MGI differential model proposed by Marrucci Greco and Ianniruberto in [9]. The evolution equation for the conformation tensor $\mathbf{c}$ is identical. The MGI model, however, lacks the last factor in the expression of the extra stress tensor (5.18), which comes from the introduction of CCR into the model. Close to equilibrium, both models are very close as the missing term in the stress equation is only a high-order term. For $\alpha = 0$, the proposed model is thus a thermodynamically-consistent version of the MGI model.

For $\alpha = 1$, the model reads:

$$\overset{\triangledown}{\mathbf{c}} = -6\left(\frac{1}{\tau_d} + J(\mathbf{c},\mathbf{k})\beta\mathbf{k} : \frac{\mathbf{c}^{1/2}}{\mathrm{tr}\,\mathbf{c}^{1/2}}\right)\left(\frac{\mathbf{c}^{3/2}}{\mathrm{tr}\,\mathbf{c}^{1/2}} - \frac{1}{3}\mathbf{c}\right), \tag{5.19}$$

$$\sigma = 6G_N^{(0)}\left(\frac{\mathbf{c}^{1/2}}{\mathrm{tr}\,\mathbf{c}^{1/2}} - \frac{1}{3}\delta\right) \cdot\left(\delta - 3J(\mathbf{c},\mathbf{k})\beta\left(3 - \frac{1}{3}\mathrm{tr}\,\mathbf{c}^{1/2}\mathrm{tr}\,\mathbf{c}^{-1/2}\right)\left(\frac{\mathbf{c}^{1/2}}{\mathrm{tr}\,\mathbf{c}^{1/2}}\right)^2\right). \tag{5.20}$$

This new model incorporates both CCR and the new strain measure as in the MGI model, but the structure of dissipative phenomena away from equilibrium, as shown in the next section, is quite different.

5.7 Model predictions

In this section, we compare the above models in various transient and steady state shear flows. In all cases, the adjustable parameter β has been set to unity as suggested in [39].

5.7.1 Step strain in shear

The normal stress ratio is an inherent feature of a model which, for step strain experiments, cannot be adjusted through a superposition of several modes; its value represents therefore a good test. Figure 5.1 shows the normal stress ratio $-\frac{N_2}{N_1}$ after a step strain in shear, as a function of the applied strain. These results were obtained numerically by applying a shear rate of large magnitude over a small time interval Δt, until a limit was reached for $\Delta t \to 0$. The experimental data are taken from Olson et al. [54]. As imposed by the strain measure (5.6) through the free energy (5.9), all three models predict a limit $\frac{-N_2}{N_1} = 0.25$ for small strains. At higher strains, however, the MGI model does seem to reach a plateau at a somewhat too large value. The proposed model, on the other hand, exhibits too strong a decrease as the strain increases. A criterion for choosing between the models would be the value of the normal stress ratio at high strains, if such data were available experimentally.

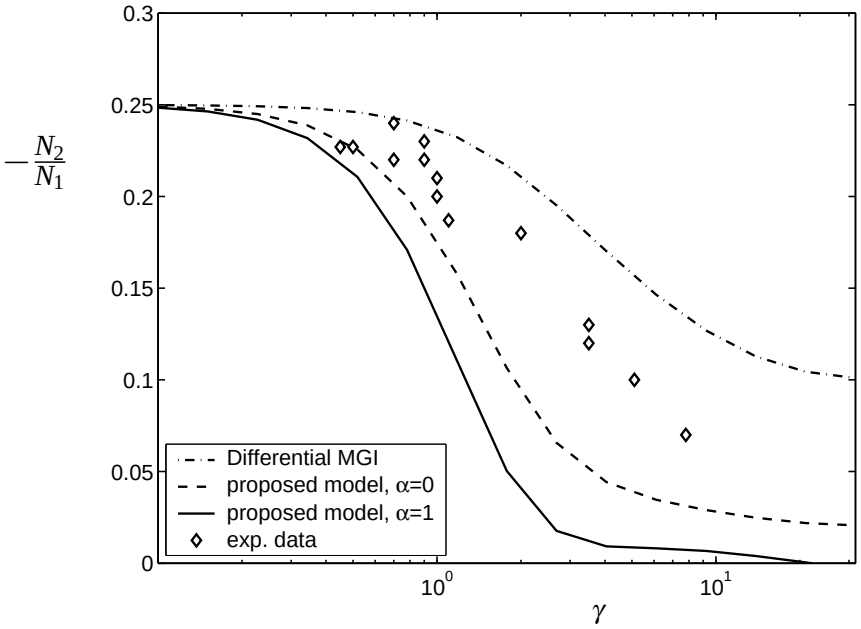

Figure 5.1: Normal stress ratio as a function of strain. Experimental data for a polystyrene solution and a poly-isoprene melt are reported from [54].

5.7.2 Steady state shear flow

As shown in Fig.5.2, the new model displays a monotonic increase of the shear stress a a function of the shear rate, with a unit value for β. On the other hand, it has been shown [9] that β needs to be greater than 3.8 in order to obtain the same feature with the MGI model. Moreover, it should be noted that, at high shear rates, the proposed model displays shear stresses approaching a plateau value very close to $G_N^{(0)}$, which is in good agreement with the Cox-Merz rule.

The steady state values of the first normal stress, shown in Fig.5.3, show a major difference between the models. While the new model with $\alpha = 0$ and MGI predict the first normal stress difference to reach a plateau, the new model with $\alpha = 1$ predicts an ever-increasing curve. Such a behaviour is in agreement with experimental data [26]. Moreover, it should be recalled that no chain stretching effects have been introduced in any of these models.

In Fig.5.4, we report the predictions of the various models as well as the experimental data for the normal stress ratio obtained by Kalogrianitis and Van Egmond

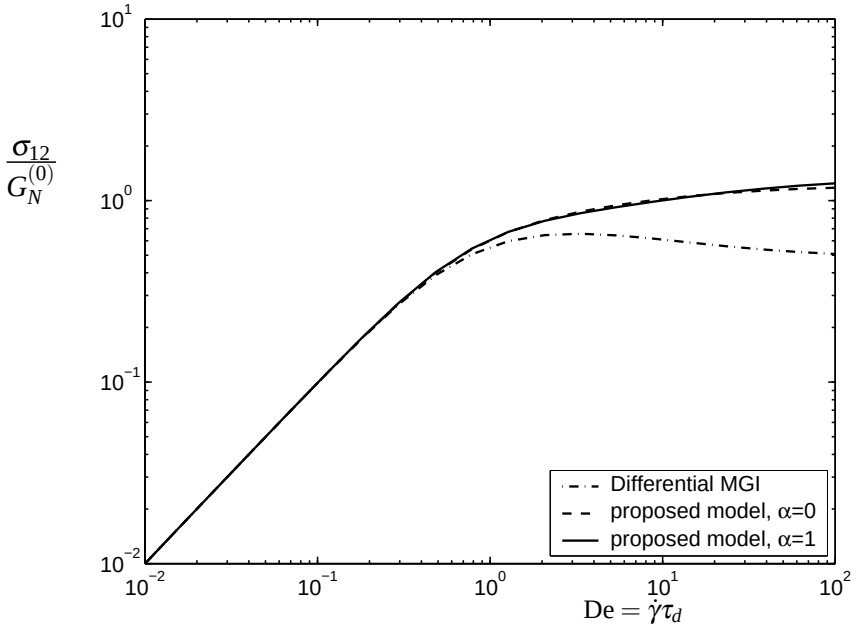

Figure 5.2: Dimensionless shear stress as a function of the Deborah number.

[64] in steady shear flow. Even though the MGI model predicts values which seem to fall in the right range, it does not predict the right slope, as the shear rate increases. The proposed model predictions for $\alpha = 0$ and 1 however provide an envelope for the experimental data. Interestingly the asymptotic limit of the normal stress ratio is a function of the α parameter. For $\alpha = 1$, the limiting ratio is $1/2$ in shear flow, while it is 0.25 in step strain (Fig.5.1). These numerical predictions have also been checked with an asymptotic analytical solution of the governing equations at small De.

5.7.3 Startup and cessation of shear flow

In this section, we consider a non-trivial transient flow, namely the startup of shear flow followed by its sudden cessation. The simulation results should be compared qualitatively with the extensive set of experiments carried out by Kalogrianitis and Van Egmond [64] on an entangled semi-dilute high molecular weight polystyrene solution. Among the features reported by these authors, we note an overshoot in the first normal stress difference upon inception of the flow, as well as an overshoot in the second normal stress difference both upon inception and cessation of the flow. Another important observation is that the relaxation of the normal stress ratio follows a

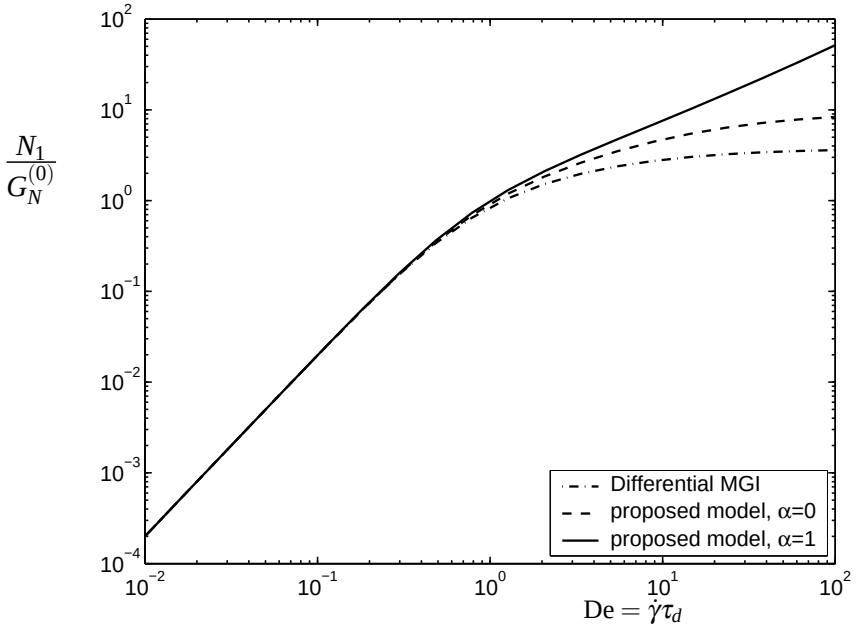

Figure 5.3: Dimensionless first normal stress difference as a function of the Deborah number.

single curve, independent of the shear rate previously applied. Also, the relaxation is non-exponential and the normal stress ratio approaches a constant value of about 0.9 at long times.

As shown in Fig.5.5, all models display an overshoot in the first normal stress difference upon inception of the flow, but it is only significant for the new model with $\alpha = 1$.

Predictions of the second normal stress difference (Fig.5.6) also show that the best behaviour is provided by the new model with $\alpha = 1$. Indeed, only this model predicts an overshoot upon cessation of the shear flow, in agreement with experimental observations [64].

The evolution of the normal stress ratio is shown in Fig. 5.7. First, we see that all the models predict the same limit at small deformations but reach different steady-state values. Upon cessation of the flow, only the new model with $\alpha = 1$ does predict the normal stress ratio to relax towards a value of 0.9, as observed experimentally. Also, the normal stress ratio predicted by the MGI model is unaffected by the cessation of the flow, in contrast with its thermodynamically-consistent version (proposed model,

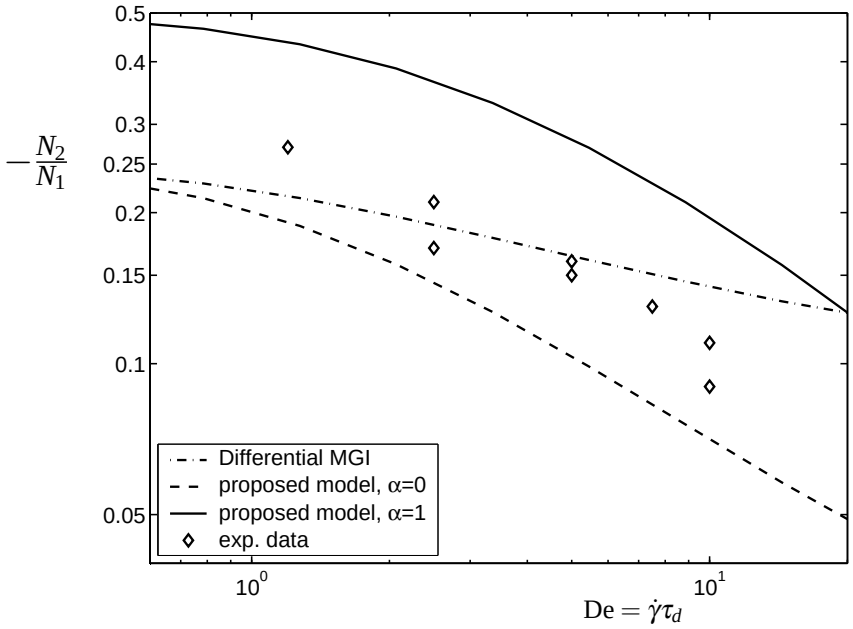

Figure 5.4: Normal stress ratio as a function of the Deborah number. Experimental data for a polystyrene solution are reported from [64].

$\alpha = 0$). Of course these two models have the same response at large times.

In Fig.5.8, we compare the transient predictions for the ratio $-\frac{N_2}{N_1}$ obtained with the proposed model against the experimental data of Kalogrianitis and Van Egmond [64]. We see from there that the new model with $\alpha = 1$ predicts the normal stress ratio to relax towards a high value of 0.9, independently of the magnitude of the previously-applied shear rate. The very fast response upon inception of the flow is caused by the selected strain measure which enforces a value of 0.25 for small deformations.

5.8 Conclusions

Using the single generator bracket formalism of non-equilibrium thermodynamics, we propose here a new constitutive equation for linear entangled polymers that incorporates a simple version of the convective constraint release as well as a new strain measure proposed by Marrucci et al. [55]. This new model reproduces the conservative behaviour of the MGI differential model also proposed by Marrucci et al. [9]

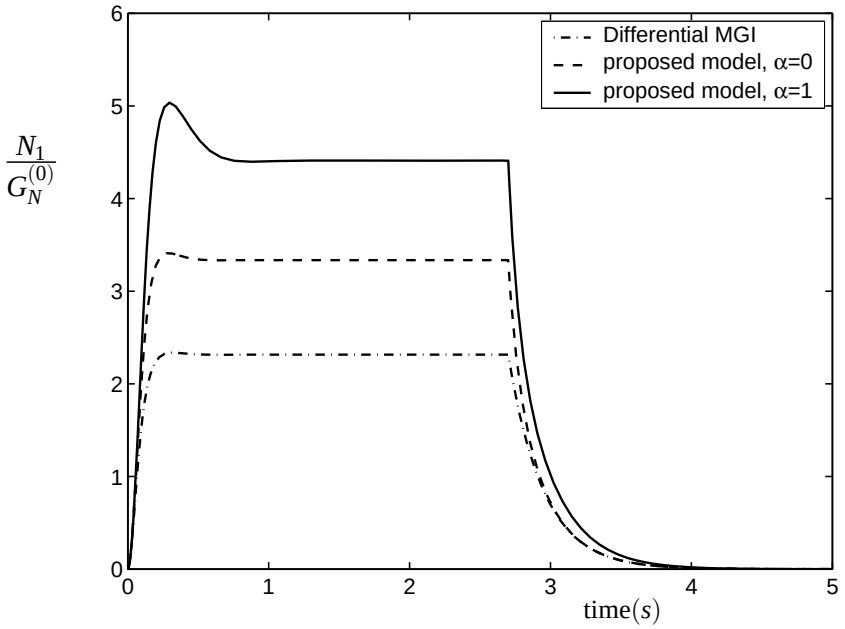

Figure 5.5: Transient first normal stress difference as a function of time. As reported in [64], a strain rate of $20s^{-1}$ is applied between time $0s$ and $2.7s$. , and $\tau_d = 0.25s$.

but has additional dissipative terms, in order to incorporate in a thermodynamically consistent fashion the convective constraint release mechanism. In steady shear flow, the new model predicts shear and normal stresses in good qualitative agreement with available experimental data. In transient shear flow, the proposed model is able to predict the qualitative behaviour of the normal stresses, especially during relaxation, after cessation of the flow.

Since these results were achieved using a single conformation tensor and with relatively simple expressions for relaxation and convective constraint release, the use of the single generator bracket formalism is considered quite encouraging for further refinements which could make the model more quantitatively correct.

Appendix 1

In this work, we considered an extended dissipative bracket, with respect to the one presented in [44]. For two arbitrary functionals F and G, the new dissipative bracket

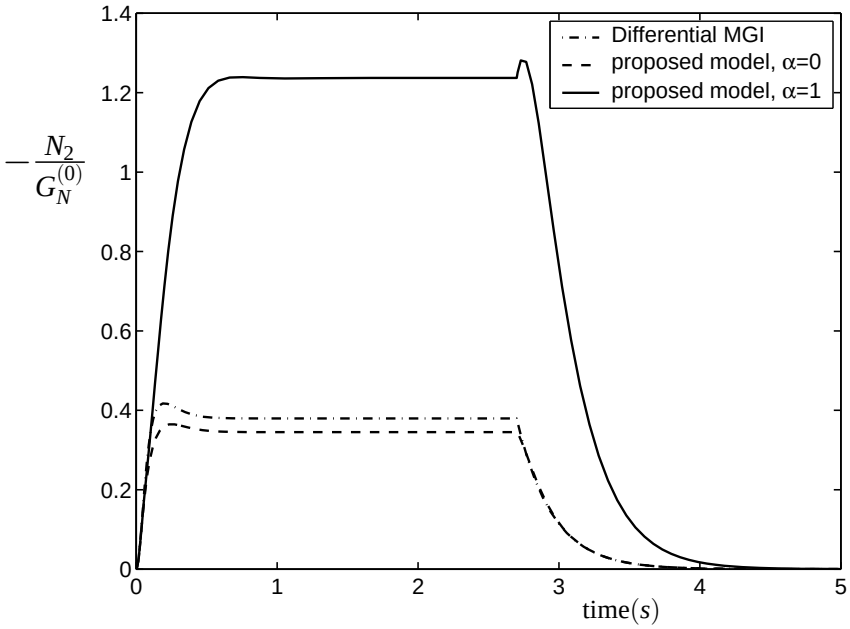

Figure 5.6: Transient second normal stress difference as a function of time. As reported in [64], a strain rate of $20s^{-1}$ is applied between time $0s$ and $2.7s$. , and $\tau_d = 0.25s$.

based on general quadratic contributions in terms of the Volterra derivatives of F and G with respect to **c** and **M** reads:

$$\begin{aligned}
[F,G] \;=\; & -\int_\Omega \Lambda_{\alpha\beta\gamma\varepsilon}\frac{\delta F}{\delta c_{\alpha\beta}}\frac{\delta G}{\delta c_{\gamma\varepsilon}}\mathrm{d}^3x \\
& -\int_\Omega Q_{\alpha\beta\gamma\varepsilon}\nabla_\alpha\frac{\delta F}{\delta M_\beta}\nabla_\gamma\frac{\delta G}{\delta M_\varepsilon}\mathrm{d}^3x \\
& -\int_\Omega L_{\alpha\beta\gamma\varepsilon}\nabla_\alpha\frac{\delta F}{\delta M_\beta}\frac{\delta G}{\delta c_{\gamma\varepsilon}} - L_{\gamma\varepsilon\alpha\beta}\nabla_\alpha\frac{\delta G}{\delta M_\beta}\frac{\delta F}{\delta c_{\gamma\varepsilon}}\mathrm{d}^3x \\
& +\text{entropy correction ,}
\end{aligned} \tag{5.21}$$

where $\frac{\delta\cdot}{\delta\cdot}$ is the Volterra derivative, M is the momentum and Ω is the flow domain. In this new expression, only the last term changes from eq. (8.1-5) in [44]. When the tensor $L_{\alpha\beta\gamma\varepsilon}$, is symmetric upon exchange of $\alpha\beta$ with $\gamma\varepsilon$, both expressions are identical. However, this new bracket allows the incorporation of a more general **c**-velocity coupling which, in the linear regime, leads to flux-potential relations that remain compatible with the extended Onsager/Casimir reciprocal relations. Direct identification leads to the dissipative terms of eqs. (5.1) and (5.2).

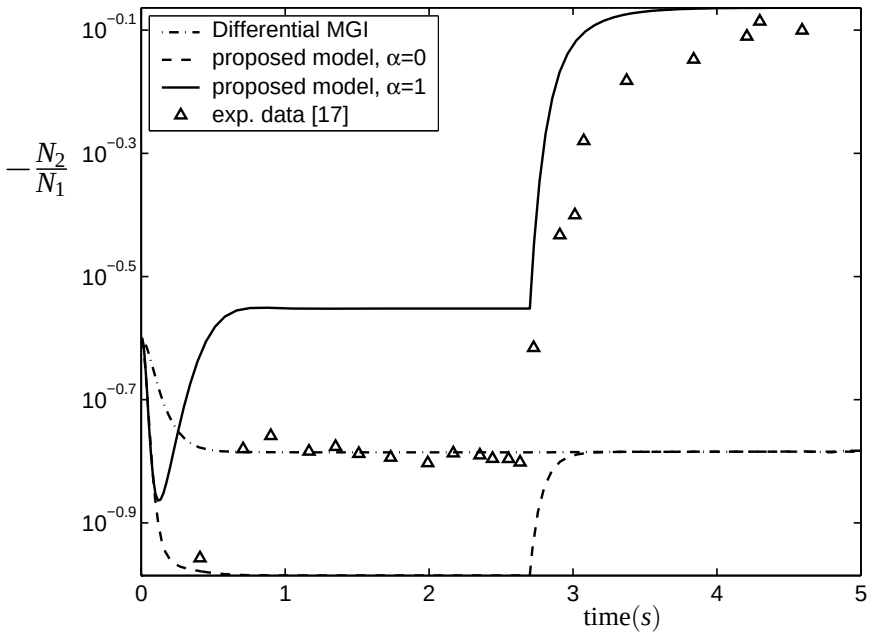

Figure 5.7: Transient normal stress ratio as a function of time. As reported in [64], a strain rate of $20s^{-1}$ is applied between time $0s$ and $2.7s$. , and $\tau_d = 0.25s$.

It is interesting to note here that in the last term of (5.21), only the anti-symmetric part of $L_{\alpha\beta\gamma\varepsilon}$ (w.r.t. $\alpha\beta \leftrightarrow \gamma\varepsilon$) brings a contribution to the entropy production, while its corresponding term in the bracket (8.1-5) of [44] was not producing any entropy. The magnitude of the **L** term needs therefore to be tailored so that it always leads to a non-negative entropy production. This is achieved by making it proportional to a *switch* function $J(\mathbf{c},\mathbf{k})$, which turns it off as soon as its rate of entropy production becomes negative. From [44], we know that the entropy production is given by:

$$\frac{\partial s}{\partial t} = -\frac{1}{T}\,[H,H]_{\text{wec}}\ , \tag{5.22}$$

where s is the entropy functional, T is the temperature, H is the Hamiltonian of the system, and the subscript wec means "without entropy correction". This immediately yields the following expression for $J(\mathbf{c},\mathbf{k})$:

$$J(\mathbf{c},\mathbf{k}) = \frac{1}{2}\left(1 + \frac{L^{\star}_{\alpha\beta\gamma\varepsilon}(\nabla_\alpha v_\beta \frac{\partial a}{\partial c_{\gamma\varepsilon}} - \nabla_\gamma v_\varepsilon \frac{\partial a}{\partial c_{\alpha\beta}})}{\left|L^{\star}_{\alpha\beta\gamma\varepsilon}(\nabla_\alpha v_\beta \frac{\partial a}{\partial c_{\gamma\varepsilon}} - \nabla_\gamma v_\varepsilon \frac{\partial a}{\partial c_{\alpha\beta}})\right|}\right)\ , \tag{5.23}$$

which is either equal to 1 or 0.

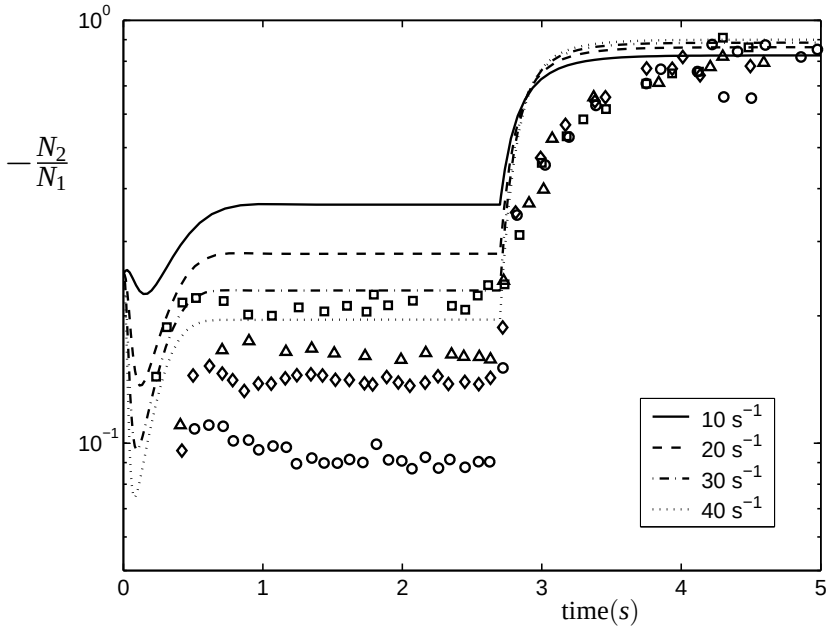

Figure 5.8: Transient first normal stress ratio as a function of time for the proposed model with $\alpha = 1$. Corresponding experimental data taken from [64].

We believe however that further developments of the convective constraint release theory might lead to a formulation of a new dissipation bracket where phenomenological corrections such as this would not be necessary anymore.

Appendix 2

The differential MGI model proposed by Marrucci et al. [9] has the following form:

$$\begin{aligned}\mathbf{T}\cdot\frac{D\mathbf{T}}{Dt}+\frac{D\mathbf{T}}{Dt}\cdot\mathbf{T} &= \mathbf{k}\cdot\mathbf{T}^2+\mathbf{T}^2\cdot\mathbf{k}^{\mathrm{T}} \\ &\quad -2\mathbf{T}^2\left(\mathbf{k}:\frac{\mathbf{T}}{G}\right) \\ &\quad -2\frac{\mathbf{T}}{\tau}\cdot\left(\mathbf{T}-\frac{G}{3}\delta\right)\,, \end{aligned} \tag{5.24}$$

$$\sigma = \mathbf{T}-\frac{G}{3}\delta\,, \tag{5.25}$$

$$\frac{1}{\tau} = \frac{1}{\tau_d}+\beta\mathbf{k}:\frac{\mathbf{T}}{G}\,, \tag{5.26}$$

where $\mathbf{k}$ is the transpose of the velocity gradient, $\frac{D\cdot}{Dt}$ is the material derivative and $G=6G_N^{(0)}$. In the absence of dissipative phenomena, $\mathbf{T}$ is linked to the Finger strain tensor $\mathbf{C}$ by the following relation:

$$\mathbf{T}=G\frac{\mathbf{C}^{1/2}}{\mathrm{tr}\,\mathbf{C}^{1/2}}\,. \tag{5.27}$$

In order to relate this constitutive equation to the proposed model with $\alpha=0$, we shall start from the evolution equation (5.1) of the conformation tensor $\mathbf{c}$:

$$\frac{D\mathbf{c}}{Dt}=\mathbf{k}\cdot\mathbf{c}+\mathbf{c}\cdot\mathbf{k}^{\mathrm{T}}+\Omega\,, \tag{5.28}$$

where Ω represents the dissipative terms. When Ω can be neglected, $\mathbf{c}$ becomes the Finger strain tensor. Defining $\mathbf{q}$ as:

$$\mathbf{q}=\mathbf{c}^{1/2}\,, \tag{5.29}$$

we find the equation describing the evolution of the trace of $\mathbf{q}$ by taking the contraction of eq. (5.28) with $\mathbf{q}^{-1}$:

$$\frac{D\mathrm{tr}\,\mathbf{q}}{Dt}=\mathbf{k}:\mathbf{q}+\frac{1}{2}\mathbf{q}^{-1}:\Omega\,. \tag{5.30}$$

Writing $\mathbf{T}$ as $\mathbf{T}=G\frac{\mathbf{q}}{\mathrm{tr}\,\mathbf{q}}$, we have:

$$\frac{D\mathbf{T}}{Dt}=\frac{G}{\mathrm{tr}\,\mathbf{q}}\frac{D\mathbf{q}}{Dt}-\frac{G}{(\mathrm{tr}\,\mathbf{q})^2}\frac{D\mathrm{tr}\,\mathbf{q}}{Dt}\mathbf{q}\,. \tag{5.31}$$

Making use of eqs. (5.30) and (5.31), we obtain an evolution equation for $\mathbf{T}$:

$$\begin{aligned}\mathbf{T}\cdot\frac{D\mathbf{T}}{Dt}+\frac{D\mathbf{T}}{Dt}\cdot\mathbf{T} &= \mathbf{k}\cdot\mathbf{T}^2+\mathbf{T}^2\cdot\mathbf{k}^{\mathrm{T}} \\ &\quad -2\mathbf{T}^2\left(\mathbf{k}:\frac{\mathbf{T}}{G}\right) \\ &\quad -\frac{\mathbf{q}^{-1}:\Omega}{\mathrm{tr}\,\mathbf{q}}\mathbf{T}^2 \\ &\quad -\left(\frac{G}{\mathrm{tr}\,\mathbf{q}}\right)^2\Omega\,.\end{aligned} \tag{5.32}$$

Identifying terms between eqs. (5.24) and (5.32), we obtain the following expression for Ω:

$$\Omega=-2\left(\frac{\mathrm{tr}\,\mathbf{q}}{\tau_d}+\beta\mathbf{k}:\mathbf{q}\right)\left(\frac{\mathbf{q}^2}{\mathrm{tr}\,\mathbf{q}}-\frac{1}{3}\mathbf{q}\right)\,. \tag{5.33}$$

The two dissipative contributions of eq. (5.32) indeed reduce to:

$$\begin{aligned}\frac{\mathbf{q}^{-1}:\Omega}{\mathrm{tr}\,\mathbf{q}}\mathbf{T}^2 &= \mathbf{0}\,, \\ \left(\frac{G}{\mathrm{tr}\,\mathbf{q}}\right)^2\Omega &= -2\frac{\mathbf{T}}{\tau}\cdot\left(\mathbf{T}-\frac{G}{3}\delta\right)\,.\end{aligned}$$

The exact form of $\Lambda^{(1)}$ is then obtained by comparing eqs. (5.1), (5.8), (5.14) and (5.33).

The expression (5.18) for the stress equation of the proposed model with $\alpha=0$ differs however from eq. (5.25) as we are using a non-zero $\mathbf{L}$ tensor in the modelling of dissipation. Combining eq. (5.2) with eqs. (5.8), (5.11) and (5.14) we obtain the following stress equation for the new model ($\alpha=0$):

$$\sigma=\left(\mathbf{T}-\frac{G}{3}\delta\right)\cdot\left(\delta-\beta\frac{\mathbf{T}}{G}\left(3-\frac{G}{3}\mathrm{tr}\,\mathbf{T}^{-1}\right)\right)\,. \tag{5.34}$$

This expression clearly shows that the new term in the stress equation (compared with equation (5.25)) is a higher order term (order $\mathbf{T}^2$), which vanishes close to equilibrium. It should also be noticed that

$$3-\frac{G}{3}\mathrm{tr}\,\mathbf{T}^{-1}=0\,,$$

at equilibrium.

Conclusions

Throughout this thesis, we have investigated the modelling of entangled polymers with a clear focus on the non-linear rheology of linear polymers. We have studied both the linear and the non-linear regimes, trying to model the latter as a continuous extension of the former.

We first proposed a differential formulation of thermal constraint release for mono- and poly-disperse systems of entangled linear polymers. This formulation allows one to compute in a self consistent way the tube survival probability of linear chains subject to reptation and thermal constraint release. Although the involved equations are highly non-linear, an analytical solution has been proposed. This allowed us to prove that our approach to thermal constraint release yields results that are mathematically equivalent to the double reptation theory, as formulated by Des Cloizeaux [5]. The phenomenological mixing exponent found in double reptation appears naturally in the differential formulation, as a parameter controlling the effectiveness of thermal constraint release. When the rate of constraint release can be approximated by a constant, we show that the tube survival probability is governed by a linear equation.

The differential formulation of the tube survival probability equation under reptation and thermal constraint release has then been extended to account for contour-length fluctuations as well. We used the position-dependent diffusion approach implemented by Graham et al. [23] to model the enhanced relaxation due to the fluctuation of the chain ends. We showed the ability of the resulting model to quantitatively predict, with a single set of parameters, the linear viscoelastic moduli of different polystyrene samples having very different molecular weight distributions. Using a simple multi-mode decomposition of the constraint release dynamics, we proposed a mathematically linear model to compute the tube survival probability of a polydisperse system of chains subject to reptation, contour-length fluctuations and thermal constraint release.
Only a mathematically linear theory of the linear viscoelasticity may be extended to a

full non-linear constitutive equation that would predict both the linear and non-linear rheology.

The CRAFT model is built as a non-linear extension of our mathematically linear model of linear viscoelasticity. The model uses an internal parametric coordinate to model the conformation of the entangled segments along the primitive path. The dynamics of the chain is described through partial differential operators along this coordinate. The physical phenomena accounted for are reptation and contour-length fluctuation, chain stretch relaxation and thermal as well as convective constraint release. Due to the deep roots of the model in the linear regime, most of the material parameters can be identified from the linear response of an entangled linear polymer. The only truly non-linear parameter is related to the finite extensibility of the chains and can be inferred from the number of Kuhn steps between entanglements. Nevertheless, we tend to consider this parameter as a fully adjustable parameter. Indeed, a number of mathematical approximations found between the microstructural picture and the final model actually degrades the physical meaning of the parameter. Polydispersity can be accounted for without any additional parameter but the molecular weight distribution of the system. Convective constraint release provides the necessary coupling between the dynamics of all masses.

The predictions of the CRAFT model have been validated with experimental data for polystyrene melts [8] and concentrated solutions [6; 7]. We found that the CRAFT model is capable of predicting quantitatively both the linear and non-linear rheology of entangled linear polymers in a wide variety of shear and extensional flows. The most stringent tests involved large amplitude oscillatory shear flows of mono- and poly-disperse samples. For these tests, the CRAFT model is capable of quantitatively predicting highly non-linear features such as secondary loops in the Lissajous figures, or the magnitude of high harmonics of the shear stress. Furthermore, the CRAFT model is, today, among of the few constitutive equations that can predict the rare extensional viscosity data measured by Bach et al. [8].

The CRAFT model shows that much of the non-linear rheology of entangled systems can be predicted quantitatively using a combination of few linear parameters and some linear and non-linear relaxation mechanism. The non-linear constitutive model has, however, to be built carefully in order to preserve the quantitative physical meaning of the linear parameters.

Despite the successes of the CRAFT model, many issues remain open in the more general field of constitutive equations for entangled systems. We mention here some of those which could be addressed in future work or that we find of particular interest.

In the case of polymer melts, we have shown the excessive elastic behaviour of

the CRAFT model, characterized by too high stretch levels. In a first attempt to solve this issue, we tried to arbitrarily reduce the maximum extensibility parameter. This approach has proved to be successful, especially in extensional flows, but its impact in other types of flows should be addressed. Another option might be to consider inter-chain pressure effects as suggested by Marrucci and Ianniruberto [36]. As the non-linear rheology of entangled systems is still a very active field of research, new relaxation phenomena will be identified and will have to be accounted for in future constitutive models.

In the case of concentrated entangled polymer solutions, we have shown that there are some differences between the Rouse time needed to fit the experimental linear moduli and the Rouse time needed to fit non-linear features such as overshoots in the transient response or strain hardening in extensional flows. Some additional modelling efforts on entangled polymer solutions might help reduce these differences in the Rouse time.

We have studied the compatibility of constitutive equations with the single-generator bracket formalism of non-equilibrium thermodynamics [44], and showed how this tool could provide consistency checks for a model and improve the predictions of a model. The compatibility of the CRAFT model with the bracket formalism, or any similar formalism such as GENERIC [57], has not been established yet but we believe that the task should not be too complicated. Most of the work should actually be devoted to the proper description of the chain stretch dynamics. Furthermore, these frameworks are powerful tools to phenomenologically modify constitutive models in order to improve their predictions in the non-linear regime.

Due to the crude approximations made in the description of the stretch dynamics, the CRAFT model does not predict a second normal stress difference. Is there an easy way to correct this while preserving the simple structure of the model? The single-generator bracket formalism might provide an easy way to alleviate this shortcoming of the model using a consistent Giesekus-like modification of the dissipative terms.

Can the CRAFT model be extended to more complex architectures such as star polymers?

Although the mechanism of convective constraint release is today better understood in steady flows, most of its implementations yield a negative rate of constraint release in reversing flows such as LAOS. We believe that additional efforts should be spent to come with a description of convective constraint release that would be valid for all kind of flows. Stochastic full-chain models can provide a strong lead in this specific issue. The study of other reversing deformations such as double step shear strain provides a tough test for the model.

As research goes on in the field of constitutive models for entangled polymers, as more and more models are developed, it is always possible to take another step forward and further push the limitations of the existing models. As the available computing power increases, mesoscopic stochastic models and atomistic models become the tools of choice for a deeper investigation. We nevertheless believe that robust micro-structural models at the level of continuum mechanics still have a bright future in the field of complex flow simulation or numerical rheometry.

Related Contributions A

Numerical simulation of large amplitude oscillatory shear of a high-density polyethylene melt using the MSF model

A.1 Introduction

Molecular models have become increasingly popular to describe the complex rheological behavior of entangled polymeric liquids. Practically all recently developed molecular models are extensions of the Doi–Edwards theory. Although the basic Doi–Edwards (DE) model [12] can successfully predict the damping function and the plateau modulus of linear viscosity, it has some important deficiencies like excessive shear thinning in fast shearing flows. Recent extensions of the Doi–Edwards theory have alleviated these shortcomings. We consider one of such extensions, the molecular stress function (MSF) model which has recently been proposed by Wagner *et al.* [10]. The nonlinear response is captured through the introduction of an extra evolution equation for the molecular stress function. The model has two additional material parameters, one to describe extensional and one to describe shear flows. With only two nonlinear parameters, the MSF model is able to accurately predict the nonlinear response in start up of shear and extension for a commercial linear high-density and

branched low-density polyethylene [10].

The linear spectrum of polymer melts is normally determined in small amplitude oscillatory shear flow. At low strains, the material response is approximately linear. At larger strains, however, nonlinear effects do play an important role. Early large amplitude oscillatory shear (LAOS) experiments date already from almost 50 years ago [65]. A recent overview of LAOS has been given by Giacomin and Dealy [48]. Wilhelm *et al.* [49; 50] introduced high sensitivity Fourier-transform rheology and analyzed large amplitude step shear oscillations of polymer melts [66]. Very recently, Debbaut and Burhin [52] performed LAOS experiments on a commercial high density polyethylene melt up to high strains of 10. Their simulations with a Giesekus model showed good agreement for moderate non-linear regimes and larger deviations for the most non-linear regimes that were experimentally achievable.

In this paper, we study the rheometrical response of the MSF model in large amplitude oscillatory shear flow. In particular, we investigate whether such models derived from molecular theory are able to accurately predict experimental data of a commercial linear polymer melts. In order to perform the simulations in an efficient and accurate manner, we modify the deformation field method of Hulsen *et al.* [67] (Sec. A.4). After validation of the numerical technique in Sec. A.6, we show that the MSF model, having only one relevant material parameter in LAOS, can accurately predict experimental results for a linear high-density polyethylene melt [52]. At medium strains, the performance is comparable to that of a six-mode Giesekus fluid having six material parameters to describe the nonlinear regime. At these strains the basic Doi–Edwards model already underpredicts the experimental data. At the higher strains, both the MSF and Giesekus model overpredict the experimental data, although the MSF model renders slightly to significantly better predictions depending on the value of the nonlinear material parameter. Completely unexpectedly, it is the Doi–Edwards model that shows excellent agreement with the experimental data at the high strains. Then the DE model, having no nonlinear material parameters, outperforms both nonlinear models.

A.2 Governing equations

For the MSF model the stress is related to the deformation history by

$$T(t) = 5 \int_{-\infty}^{t} m(t-t') f_{t'}^2(t) Q[B_{t'}(t)] \, \mathrm{d}t', \tag{A.1}$$

where $B_{t'}(t)$ is the Finger tensor which measures the deformation of a fluid particle at the current time t with respect to a reference time t'. The memory function m assumes

the classical multimode Maxwell form

$$m(t-t') = \sum_i \frac{G_i}{\lambda_i} \int_{-\infty}^{t} \mathrm{e}^{-(t-t')/\lambda_i}, \tag{A.2}$$

where G_i are the moduli and λ_i are the relaxation times of the fluid.

The tensor Q is the strain measure for which the independent alignment approximation was used in the original derivation in [10]. Instead, we use the Currie approximation to the Doi–Edwards deformation tensor [68]. The orientation tensor Q is then directly related to the Finger strain $B_{t'}$ and the Cauchy strain $B_{t'}^{-1}$ by

$$Q = \frac{1}{J-1} B_{t'} - \frac{1}{(J-1)(I_2+3.25)^{1/2}} B_{t'}^{-1}. \tag{A.3}$$

Here, $J = I_1 + 2(I_2+3.25)^{1/2}$ and I_1 and I_2 are the first and second invariant of $B_{t'}$, respectively. For large amplitude oscillatory shear flow this is a very good approximation to the Doi–Edwards tensor using the independent alignment approximation, as we show in Sec. A.7.

The MSF model is completed by an evolution equation for the Finger tensor and the molecular stress function $f_{t'}$. The Finger tensor is governed by

$$\frac{DB_{t'}}{Dt} = \kappa \cdot B_{t'} + B_{t'} \cdot \kappa^T, \tag{A.4}$$

where κ is the transpose of the velocity gradient. For the MSF model, the evolution equation for square of the molecular stress function takes different forms for linear and branched polymers. For linear polymers we have

$$\frac{Df_{t'}^2}{Dt} = f_{t'}^2 \left[\kappa : Q - \frac{1}{f_{t'}^2 - 1} \mathrm{CR} \right] \tag{A.5}$$

while for branched polymers the right-hand side is slightly modified [10; 69]. The dissipative constraint release CR is expressed as

$$\mathrm{CR} = \frac{1}{2}(f_{t'}^2 - 1)^2 \left[a_1 \sqrt{A_1^2 : Q} + a_2 \sqrt{|A_2 : Q - A_1^2 : Q|} \right], \tag{A.6}$$

where A_1^2 and A_2 are second-order Rivlin–Erickson tensors which are related to the rate-of-deformation tensor $d = (\kappa + \kappa^T)/2$ and rate-of-rotation tensor $w = (\kappa - \kappa^T)/2$ by

$$\begin{aligned} A_1^2 &= 4d^2, \\ A_2 &= \frac{DA_1}{Dt} + A_1^2 + 2w \cdot d + 2d \cdot w^T. \end{aligned} \tag{A.7}$$

The parameters a_1 and a_2 in Eq. (A.6) are the only two nonlinear parameters in the MSF model. The only parameter that is relevant in steady non-rotational flows is a_1, since $A_2 : Q - A_1^2 : Q$ vanishes in that case. The value of a_1 can be determined by fitting extensional flow data. Next, a_2 can be obtained from shear viscosity and first normal stress data.

The MSF theory is an extension of the basic Doi–Edwards tube theory [12]. The difference between the models is the inclusion of the molecular stress function for the MSF model. To evaluate the improvement of this model in large amplitude oscillatory shear, we use the Doi–Edwards (DE) model for comparison. The governing equations are then Eqs. (A.1-A.4) with $f_{t'}^2 = 1$ in the expression for the polymer stress. The DE model has no nonlinear parameters and is fully characterized by the linear spectrum.

A.3 Large amplitude oscillatory shear flow

In large amplitude oscillatory shear flow a fluid is subject to a periodic shear deformation γ with amplitude γ_0 and frequency ν,

$$\gamma(t) = \gamma_0 \sin(2\pi\nu t). \tag{A.8}$$

The deformation is applied for $t > 0$ and up to $t = 0$ the fluid is assumed at rest. The corresponding periodic shear rate $\dot{\gamma}$ equals

$$\dot{\gamma}(t) = 2\pi\nu\gamma_0 \cos(2\pi\nu t). \tag{A.9}$$

With this shear rate, the polymeric stress is obtained as a function of time from the constitutive equations Eqs. (A.1,A.2,A.3,A.4) and the evolution equation for the molecular stress function for linear polymers, Eq. (A.5,A.6,A.7). Since the stress response attains a steady periodic state, a Fourier transform facilitates a detailed quantitative analysis. The shear stress is decomposed into an infinite sum of trigonometric functions,

$$T_{xy}(t) = \frac{A_0}{2} + \sum_{n=1}^{\infty} A_n \sin(2n\pi\nu t) + \sum_{n=1}^{\infty} B_n \cos(2n\pi\nu t), \tag{A.10}$$

where A_n and B_n are the Fourier coefficients. For a real signal, these coefficients are given by

$$A_n = 2\nu \int_c^{c+1/\nu} T_{xy} \sin(2n\pi\nu t)\, \mathrm{d}t, \qquad B_n = 2\nu \int_c^{c+1/\nu} T_{xy} \cos(2n\pi\nu t)\, \mathrm{d}t \tag{A.11}$$

for an arbitrary period ranging from c to $c + 1/\nu$. The Fourier coefficient A_0 vanishes in view of the two-fold symmetry of the periodic shear stress signal. Standard numerical integration has been used to evaluate the integrals in Eq. (A.11).

Recently, Debbaut and Burhin [52] have described a new viscometric device to characterize polymer melts in large amplitude oscillatory shear flows. The experimental equipment consisted of an oscillatory device with a closed chamber to allow for higher frequencies. At a temperature of 170 °C, LAOS experiments have been performed at various frequencies and amplitudes for the commercially available high density polyethylene melt Finathene®3802 YCF. Experimental data are available for the frequencies $\nu = 0.1$ Hz, $\nu = 0.3$ Hz, $\nu = 1$ Hz, and $\nu = 3$ Hz and for the amplitudes $\gamma_0 = 0.5$, $\gamma_0 = 1$, $\gamma_0 = 2.5$, $\gamma_0 = 5$, and $\gamma_0 = 10$. For the higher frequencies, not all amplitudes can be achieved experimentally. For $\nu = 1$ Hz the highest achievable amplitude is $\gamma_0 = 5$ while for $\nu = 3$ Hz this is $\gamma_0 = 1$. For further reference, we note that the maximum shear rates that occur at the highest amplitude for each frequency are $\dot{\gamma}_{\max} \approx 6.28\ \mathrm{s}^{-1}$ for $\nu = 0.1$ Hz, $\dot{\gamma}_{\max} \approx 18.85\ \mathrm{s}^{-1}$ for $\nu = 0.3$ Hz and $\nu = 3$ Hz, and $\dot{\gamma}_{\max} \approx 31.42\ \mathrm{s}^{-1}$ for $\nu = 1$ Hz.

A.4 Numerical method for simulation in LAOS

The evolution equations for the Finger tensor $B_{t'}$ are easily integrated analytically for large amplitude oscillatory shear, i.e. for the shear rate specified by Eq. (A.9). We obtain for the non-constant components of the Finger tensor

$$\begin{aligned} B^{xy}_{t'}(t) &= \begin{cases} \gamma_0 \sin(2\pi\nu t) & t' \le 0 \\ -\gamma_0 \sin(2\pi\nu t') + \gamma_0 \sin(2\pi\nu t) & t' > 0 \end{cases} \\ B^{xx}_{t'}(t) &= 1 + \left(B^{xy}_{t'}\right)^2(t). \end{aligned} \tag{A.12}$$

The strain measure Q can thus be obtained analytically and the only evolution equation that remains to be solved numerically in LAOS is the evolution equation for $f^2_{t'}$, Eq. (A.5) for linear polymers. To solve the evolution equation for $f^2_{t'}$, we follow the idea of Hulsen *et al.* [67], who used the age $\tau = t - t'$ as independent variable instead of t' to solve the evolution equation for the Finger tensor $B(t,\tau) = B_{t'}(t)$. The introduction of τ as an independent variable modifies the time derivative in the evolution equation, but leaves the right-hand side unaltered. The proper equation for $f^2(t,\tau) = f^2_{t'}(t)$ involves a derivative with respect to t and τ resulting from the material derivative while leaving the right-hand side of an evolution equation unaltered. For the molecular stress function describing linear polymers, Eq. (A.5), we obtain

$$\frac{Df^2}{Dt} + \frac{\partial f^2}{\partial \tau} = f^2 \left[\kappa : Q - \frac{1}{(f^2-1)} \mathrm{CR} \right] \tag{A.13}$$

subject to the boundary condition $f^2(t,0) = 1$ and the initial condition $f^2(0,\tau) = 1$, since the fluid is assumed to be at rest for $t < 0$.

In [67], the Discontinuous Galerkin (DG) method is used for the discretization of the differential equation for the Finger tensor in the τ direction. For transient flow problems involving large and small time scales, the DG discretization in τ is not very appealing. Large relaxation times imply a long time before a steady periodic state has been reached. For the simulations in Sec. A.7 we used 200 s. The small relaxation times on the other hand require a fine discretization for small τ. The DG method requires a time step of $\Delta t < \Delta\tau/6$ for reasons of stability. For our simulations in Sec. A.7 we use 1520 τ intervals which have a minimum length of $9.69\,10^{-6}$ s. For the Discontinuous Galerkin method to remain stable, the maximum time step is approximately $1.6\,10^{-6}$. To avoid very long computation times, we proceed differently.

Discretization of the age τ is performed in a similar way as in [67]. We replace the semi-infinite age interval $\tau \in [0,\infty)$ by a finite interval $[0,\tau_c]$ with τ_c the cut-off age. This value has to be large compared to the largest relaxation time $\lambda_{\max}$ of the fluid. For the LAOS simulations in Sec. A.7 we have used $\tau_c = 20\lambda_{\max}$, which is a rather conservative value. The interval $[0,\tau_c]$ is divided into N subintervals $[\tau_j,\tau_{j+1}]$ for each $j = 0,\ldots,N-1$. These subintervals are of increasing size to take advantage of the fast decaying memory function for large values of τ/λ_i. For a one mode upper-convected Maxwell integral model, Hulsen *et al.* [67] used a stretched mesh and determined an optimal stretching factor. We found that this was not the optimal τ discretization for our multimode MSF model. To determine the mesh for the age discretization, we define a cut-off time $\tau_{c,i} = 20\lambda_i$ for every relaxation time. For the interval $[0,\tau_{c,1}]$, we compute the τ discretization exactly as in [67]. For other intervals $[\tau_{c,i},\tau_{c,i+1}]$, we use less subintervals since the region up to $\tau_{c,i}$ has already been discretized based on the smaller relaxation times.

In view of the evaluation of the stress integral Eq. (A.1), solutions to Eq. (A.13) are computed in the two-point Gauss points on each subinterval. The $2N$ Gauss points τ_k^G for each $k = 1,\ldots,2N$ define the mesh on which we compute the molecular stress function. To include the end points of the τ domain we define $\tau_0^G = 0$ and $\tau_{2N+1}^G = \tau_c$. At each Gauss point τ_k^G for $k = 1,\ldots,2N+1$, we need to solve Eq. (A.13). Note that for LAOS, the Finger tensor and thus the deformation tensor is known as a function of time and τ via Eq. (A.12).

Integration of Eq. (A.13) from time t_i to t_{i+1} and over a τ interval between two Gauss points $[\tau_k^G,\tau_{k+1}^G]$ is performed using a trapezoidal rule for the time and τ direction. This results, for each $k = 0,\ldots,2N$, in a difference equation for the molecular stress function at the new time level $i+1$,

$$f^2_{i+1,k+1} = f^2_{i,k} + \frac{\Delta t - \Delta\tau}{\Delta t + \Delta\tau}\left(f^2_{i+1,k} - f^2_{i,k+1}\right) + \frac{1}{2}\frac{\Delta t\Delta\tau}{\Delta t + \Delta\tau}\left(r_{i+1,k+1} + r_{i,k+1} + r_{i+1,k} + r_{i,k}\right), \tag{A.14}$$

where $\Delta t = t_{i+1} - t_i$, $\Delta\tau = \tau^{\mathrm{G}}_{k+1} - \tau^{\mathrm{G}}_k$, and r denotes the right-hand side of Eq. (A.13). All quantities $f^2_{i,*}$ and $r_{i,*}$ are at the previous time level and are known at the start of a new time step. The quantities $f^2_{i+1,0}$ and $r_{i+1,0}$ are known from the boundary condition at $\tau = 0$, $f^2_{i+1,0} = 1$. For the first τ interval $[0, \tau_1]$, only the quantities $f^2_{i+1,1}$ and $r_{i+1,1}$, which is a nonlinear function of f^2, are unknown. To handle the non-linearity of the right-hand side, we use a predictor-corrector scheme, for which we use $f^2_{i,j+1}$ as a predictor. Once $f^2_{i+1,1}$ is known, we can apply the same procedure to obtain $f^2_{i+1,2}$ and so on, till we have computed $f^2_{i+1,2N+1}$ at the cut-off age of the largest relaxation time.

The molecular stress function for a linear polymer melt has to remain in the range $(0, f^2_{\max})$. When we use Eq. (A.14) in LAOS simulations, we found that f^2 can easily exceed the lower and upper bound under strongly nonlinear flow conditions, particularly at large ages τ where the difference between two consecutive ages is large. This makes the method unstable. For example, once f^2 becomes negative for some value of τ it remains negative and rapidly increases in magnitude. The instability disappeared when we applied a transformation that ensures that the molecular stress function always remains between its lower and upper bound. For all our computations we used the transformation

$$h = \ln \frac{f^2}{f^2_{\max} - f^2}$$

which maps $(0, f^2_{\max})$ to $(-\infty, \infty)$. Instead of solving the differential equation for f^2, we solve the corresponding differential equation for h. Since $-\infty < h < \infty$, we can not violate any constraints. After obtaining the value of h at a new time level, the value of f^2 is recovered using the inverse mapping

$$f^2 = \frac{\mathrm{e}^h f^2_{\max}}{1 + \mathrm{e}^h}$$

which indeed ensures that $0 < f^2 < f^2_{\max}$.

In terms of time t and age τ, the integral for the stress, Eq. (A.1), becomes

$$T(t) = 5 \int_0^\infty m(\tau) f^2(t,\tau) Q\left[B(t,\tau)\right] \, \mathrm{d}\tau. \tag{A.15}$$

Once the molecular stress function is computed at the new time level, the polymer stress $T(t_{i+1})$ can be computed by integrating over τ. On the interval $[0, \tau_c]$, the integral is approximated by a finite sum and on $[\tau_c, \infty)$ we assume $f^2(t,\tau) = f^2(t,\tau_c)$ and $B(t,\tau) = B(t,\tau_c)$, so that the integral can be integrated exactly. The resulting stress at the new time level is of the form

$$\begin{aligned} T(t_{i+1}) = 5 \sum_{k=1}^{2N} w_k m(\tau^{\mathrm{G}}_k) f^2(t_{i+1}, \tau^{\mathrm{G}}_k) Q\left[B(t_{i+1}, \tau^{\mathrm{G}}_k)\right] \\ + 5M(\tau_c) f^2(t_{i+1}, \tau_c) Q[B(t_{i+1}, \tau_c)], \end{aligned} \tag{A.16}$$

where w_k, $k = 1,\ldots,2N$ are the weights corresponding to a 2-point Gauss quadrature rule and $M(\tau_c) = \sum_i G_i \exp(-\tau_c/\lambda_i)$.

The numerical simulation of the Doi–Edwards model in LAOS is more straightforward since no evolution equation needs to be solved for f^2. For every time step, only the stress needs to be computed using Eq. (A.16) with $f^2 = 1$ and the analytic solution for the Finger tensor Eq. (A.12). For this we use exactly the same age discretization as for the MSF model.

A.5 Melt properties

The linear spectrum of the Finathene melt that we use in all our viscoelastic simulations is the six-mode spectrum identified in [52] where it was used for LAOS simulations with the Giesekus model.

In addition to the linear spectrum, the MSF model only contains two nonlinear parameters for the molecular stress function, a_1 and a_2. The parameter a_1 describes the melt rheology in nonrotational flows and its value can be obtained from fitting elongational data. Next, the value of a_2, which is relevant for rotational flows, can be determined from the shear viscosity and first normal stress difference. For the Finathene melt, however, only shear data are available. This is not a major limitation since the impact of the parameter a_1 in large amplitude oscillatory shear flows is very small as we show in Sec. A.7. In this section, we use the value $a_1 = 0.02$ which was identified in [10] for another high-density polyethylene melt.

The second parameter a_2 is identified using steady shear viscosity data. These shear data were obtained from small amplitude oscillatory shear measurements and the Cox–Merz rule which is valid for the Finathene fluid [52]. For another high density polyethylene melt, the value of $a_2 = 2.3$ was identified in [10]. Using this parameter value, steady shear viscosity predictions also agree well with experimental data of the Finathene fluid as can be observed from Fig. A.1. At shear rates of order unity, the experimental data are slightly overpredicted while for $\dot{\gamma} > 10\ \mathrm{s}^{-1}$ a slight underprediction is apparent. Increasing the value of a_2 leads to better agreement with experimental data at shear rates around $\dot{\gamma} \approx 1\ \mathrm{s}^{-1}$. The underprediction of the data for $\dot{\gamma} > 10\ \mathrm{s}^{-1}$, however, persists and even slightly increases when a_2 is increased. We conclude from Fig. A.1 that the steady shear viscosity predictions are not very sensitive to changes in a_2 and that a rather wide range of parameter values a_2 fits the data equally well. For this reason, we will consider both $a_2 = 2.3$, 4, and 8 in the LAOS simulations in Sec. A.7.

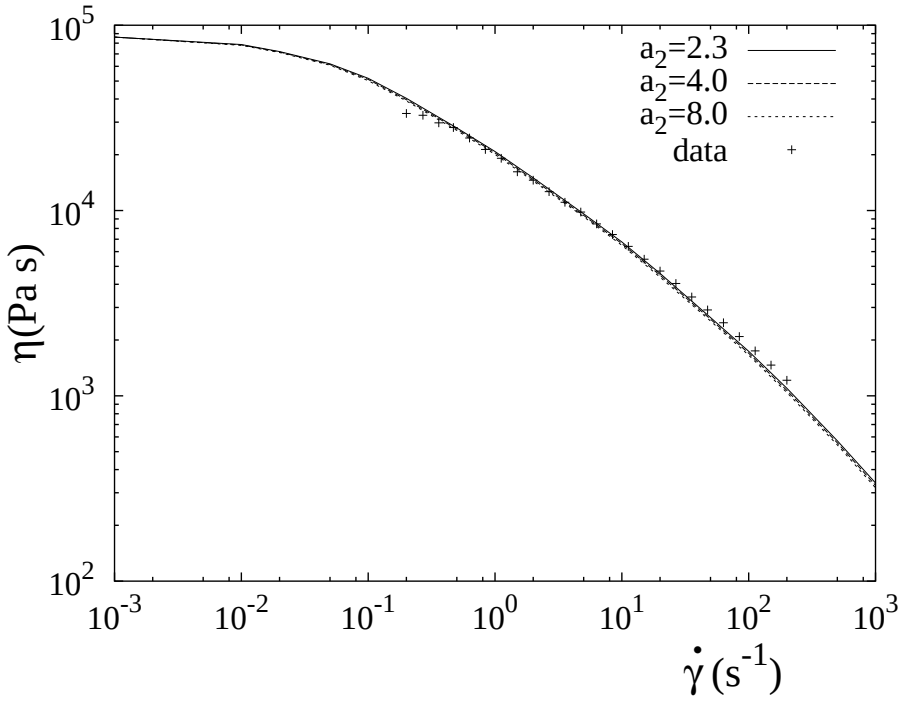

Figure A.1: Steady shear viscosity of the Finathene melt: experimental data of [52] and model predictions of the MSF model using various values of a_2 ($a_1 = 0.02$).

Results of the MSF model in large amplitude oscillatory shear will be compared with the basic Doi–Edwards model, the Giesekus model, and the inelastic Carreau–Yasuda model [70]. For both viscoelastic models, we use the same linear spectrum as for the MSF model. For the Giesekus model we use in addition the nonlinear parameter values identified in [52]. The viscosity of the Carreau–Yasuda model is given by

$$\eta = \eta_0 \left(1 + [\lambda I_2]^a\right)^{(n-1)/a}, \tag{A.17}$$

where I_2 is the second invariant of the rate-of-strain tensor d. The four adjustable parameters in the model are the zero-shear viscosity η_0, a time constant λ, the power-law index n and a numerical parameter a. The parameters are obtained from fitting the shear viscosity. We found a good fit using $\eta_0 = 8.66 \times 10^4$ Pa s, $\lambda = 18$ s, $n = 0.5$, and $a = 0.85$

The steady shear viscosity predictions of the Doi–Edwards and Carreau–Yasuda models are displayed in Fig. A.2. Surprisingly, the predictions of the Doi–Edwards

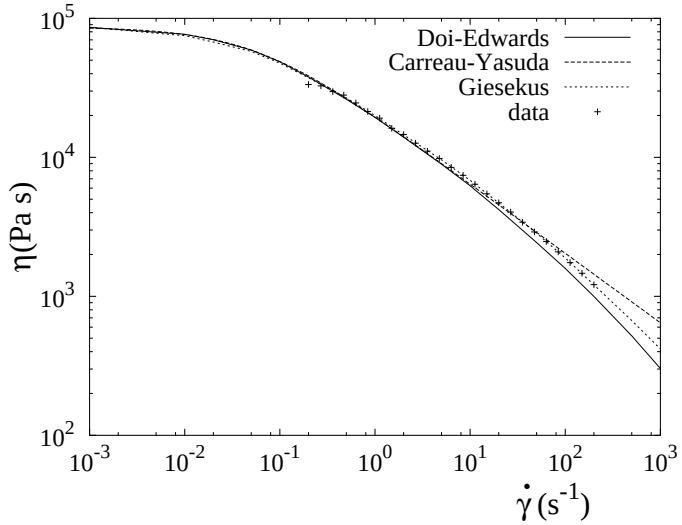

Figure A.2: Steady shear viscosity of the Finathene melt: experimental data of [52] and model predictions of the Doi–Edwards, Carreau–Yasuda and Giesekus model.

model, which has no adjustable parameters, agree well with the data up to moderate shear rates. At higher shear rates, $\dot{\gamma} > 10$ s^{-1}, the Doi–Edwards model underpredicts the experimental data. Up to shear rates that can be reached in the LAOS experiments ($\dot{\gamma} < 32$ s^{-1}), however, differences are relatively small. In fact, the predictions of the DE model are only slightly lower than those of the MSF model with $a_2 = 8$ as can be observed by comparing Fig. A.1 and Fig. A.2. The Carreau-Yasuda fit overpredicts

the viscosity at large shear rates. However, for the range of shear rates in the LAOS experiments, $\dot{\gamma} \leq 32\ \mathrm{s}^{-1}$, the purely viscous model shows good agreement. For further reference, we have also included in Fig. A.2 the steady shear viscosity predictions of the Giesekus model. The Giesekus model shows excellent agreement up to the largest experimental shear rate.

To analyse shear predictions for a transient flow like LAOS, it is also important to know the response in transient rheometrical flows. Figure A.3 displays the viscosity in start up of shear and start up of uniaxial elongation at various deformation rates. The differences between the results of the MSF models with different values of the nonlinear parameter a_2 are small. Both $a_2 = 2.3$, 4, and 8 show small time overshoots at moderate shear rates. The magnitudes of these overshoots and the steady viscosity slightly decrease with increasing value of a_2. For the largest value of $a_2 = 8$, the predictions lie only just above those of the Doi–Edwards model. For further reference, we also include in Fig. A.3(a) the model predictions of the Giesekus model. There are two differences with the molecular models. First, the larger time overshoots. This becomes apparent at relatively low shear rates of $\dot{\gamma} = 1$ and becomes more pronounced when the shear rate is increased. Second, the Giesekus has a higher steady shear viscosity at high shear rates. This is in better agreement with the data in Fig. A.1. For the LAOS experiments, however, such high rates can not be achieved experimentally.

Figure A.3(b) shows that the differences between the models is much more pronounced in start up of uniaxial extension, at significantly large values of the extension rate $\dot{\varepsilon}$. The MSF model shows considerable strain hardening which increases when a_1 is increased. This behaviour is absent for the Doi–Edwards model.

A.6 Validation of the numerical results

For the validation of the numerical technique and various numerical parameters, we use the MSF model for linear polymers with parameter values $a_1 = 0.02$ and $a_2 = 2.3$. Other parameter settings, not shown in this section, gave identical results.

We first validate our numerical technique described in Sec. A.4, by comparing with the deformation field method using the discontinuous Galerkin method to discretise the τ direction in the equation governing the molecular stress function. This is exactly the same approach as discussed in [67] for the Finger tensor. For both techniques we take the same τ discretization using 1520 τ subintervals. Figure A.4(a) shows the results of both techniques in LAOS with $\nu = 1$ Hz and $\gamma_0 = 5$ which has the highest achievable shear rate in the experiments. At the scale of the plot the methods

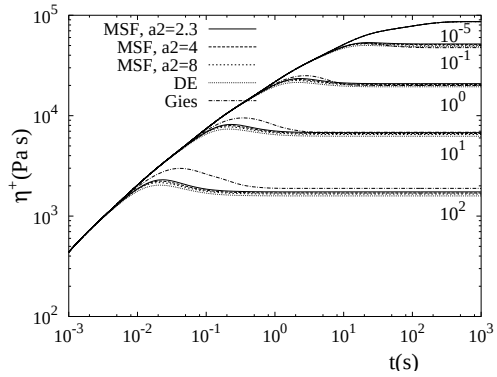

(a)

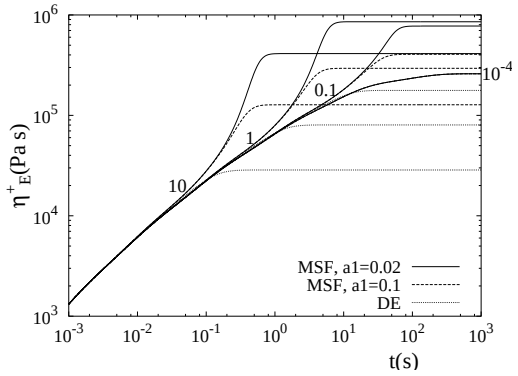

(b)

Figure A.3: Transient viscosity of MSF model for various parameter settings. The Doi–Edwards and Giesekus model are included for comparison. Deformation rates (s^{-1}) are indicated in the figures. (a) start up of shear for $a_1 = 0.02$ and values of a_2 indicated in the legend, and (b) start up of uniaxial elongation for values of a_1 indicated in the legend (a_2 irrelevant).

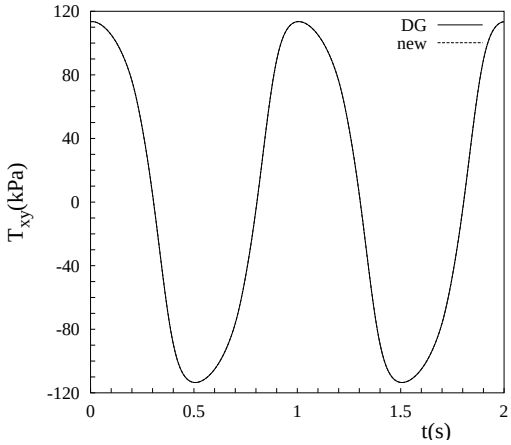

(a)

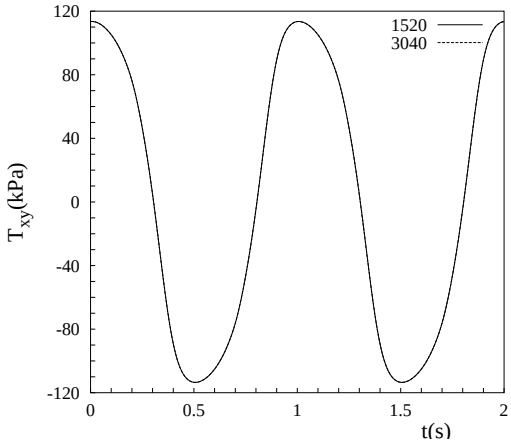

(b)

Figure A.4: Validation of the numerical technique a) Comparison of new method with the DG method of [67] b) Comparison of various τ discretizations.

are indistinguishable. The main difference lies in the time step employed. For the new method we have used a time step of $\Delta t = 2.5\ 10^{-4}$ s while for the DG method a time step of $\Delta t = \Delta\tau/6$ is necessary for reasons of stability [67]. For a τ discretization using 1520 subintervals, the minimum length of a subinterval equals $\Delta\tau_{\min} = 9.6\ 10^{-6}$ s. This requires a time step smaller than $\Delta t = 1.6\ 10^{-6}$ s. In combination with the long time required to reach a periodic steady state, such small time steps lead to long simulation times for the DG method. The new technique, however, remains stable for much larger time steps leading to substantially smaller computation times.

Second, it needs to be checked whether the discretization in τ using $N = 1520$ subintervals is sufficient to capture the steady periodic stress response. In order to verify this, we compare with a τ discretization that has twice as many subintervals, $N = 3040$, which implies a smallest τ subinterval which is halved, $\tau_{\min} = 4.8\ 10^{-6}$ s. For both computations we used a time step of $\Delta t = 2.5\ 10^{-4}$ s. The steady periodic shear stress for both τ discretizations is displayed in Fig. A.4(b). On the scale of the figure there are no differences between the two τ discretizations. Henceforth, we use the smallest number of subintervals, $N = 1520$, for all simulations with the MSF model.

A time step of $\Delta t = 2.5\ 10^{-4}$ s is sufficiently small to capture the steady periodic regime as can be observed from Fig. A.5(a). When the time step is halved to $\Delta t = 1.25\ 10^{-4}$ s, both time steps produce identical results on the scale of the figure. For both simulations we used $N = 1520$ subintervals for the τ discretization. Henceforth, we use $\Delta t = 2.5\ 10^{-4}$ s for all LAOS simulations.

In Section A.7, LAOS simulations are performed for a time of $t_s = 200$ s. Fig. A.5(b) compares shear stresses using $t_s = 200$ s and $t_s = 1000$ s for the highest experimentally achievable amplitudes at a low frequency ($\nu = 0.1$ Hz) and a high frequency ($\nu = 1$ Hz). For both calculations we used $\Delta t = 2.5\ 10^{-4}$ s and $N = 1520$. We conclude from Fig. A.5(b) that $t_s = 200$ s is sufficiently large to reach the steady periodic regime. This value of t_s is a rather conservative choice. The stress maxima only differ 0.1% from the steady periodic value after 3 and 15 cycles for $\nu = 0.1$ Hz and $\nu = 1$ Hz, respectively.

A.7 Large amplitude oscillatory shear results

The MSF theory uses the strain measure based on the independent alignment approximation. In view of the large number of time steps that have to be performed, it is advantageous to use the computationally much more efficient Currie approximation

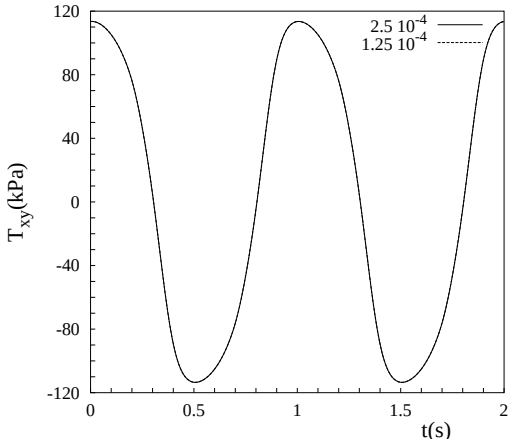

(a)

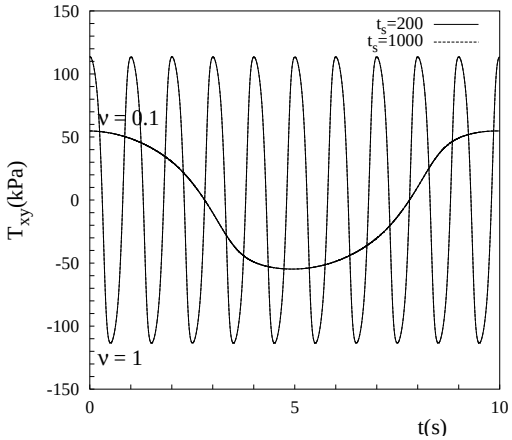

(b)

Figure A.5: Validation of sufficiently small time step (a) and sufficiently large t_s (b).

instead. This is a good approximation in steady and start-up of shear for the Doi–Edwards model [68]. It is, however, a priori not clear how well both strain measures correspond in large amplitude oscillatory shear flows of an MSF fluid. For this we compared the steady periodic shear stress at a low ($\nu = 0.1$ Hz) and high frequency ($\nu = 1$ Hz) for the two highest amplitudes γ_0 that are experimentally achievable for each frequency. As can be seen from Fig. A.6, the flow curves of the Currie and independent alignment approximation agree very well. Only near the minima and maxima we observe that the Currie approximation slightly overpredicts the independent alignment approximation. This is, however, negligible compared to the differences between the various model predictions and the experimental data as we discuss shortly. The approximation is equally good for the other two frequencies, $\nu = 0.3$ Hz and $\nu = 3$ Hz, which are not shown in Fig. A.6. We conclude from Fig. A.6 that in large amplitude oscillatory shear simulations of an MSF fluid, the Currie approximation is a very good approximation to the independent alignment approximation of the Doi–Edwards strain measure. Henceforth, we use the Currie approximation in all LAOS simulations.

To accurately determine the parameter a_1 of the MSF model for a polymeric fluid, extensional data are required. For the Finathene melt, however, only shear data are available. Therefore, we first compare the periodic steady shear response for two realistic values of a_1. For the first value, we take $a_1 = 0.02$ ($f^2_{\max} = 51$) as identified in [10] for another high density polyethylene melt. The linear polymers considered in [71] have a lower $f^2_{\max}$. For the second value, we take $f^2_{\max} = 11$ which corresponds to $a_1 = 0.1$. Figure A.7 shows the impact of a_1 on the periodic steady shear response for $\nu = 1$ Hz at the two highest experimentally achievable amplitudes $\gamma_0 = 2.5$ and 5. At the scale of the figure, both parameter values of a_1 result in identical model predictions. We conclude that the only relevant MSF model parameter for large amplitude oscillatory shear flow of linear polymers is a_2 and henceforth we use $a_1 = 0.02$ for all simulations.

The LAOS experiments have been performed at various frequencies and amplitudes. At low values of ν and γ_0, the flow doesn't deviate much from low amplitude oscillatory shear. It is therefore not surprising that all viscoelastic models predict similar results that do not differ much from the experimental data. As an example, we display for $\gamma_0 = 1$ the steady periodic response for $\nu = 0.1$ Hz and for $\nu = 1$ Hz in Fig. A.8. All viscoelastic models considered predict the correct phase shift of the periodic shear stress. The MSF model, for all parameter values of a_2 considered, also correctly predict the amplitude. The Doi–Edwards model, however, clearly underpredicts the amplitude in the mildly nonlinear regime. To investigate the impact of viscoelasticity we also display results of an inelastic model possessing only shear-thinning behaviour. This model is only able to predict the correct amplitude and fails to predict the phase shift. At $\nu = 1$ Hz and $\gamma_0 = 1$, which corresponds to a maximum shear rate of $\dot{\gamma} \approx 6.3$, the inelastic model also significantly overpredicts the amplitude

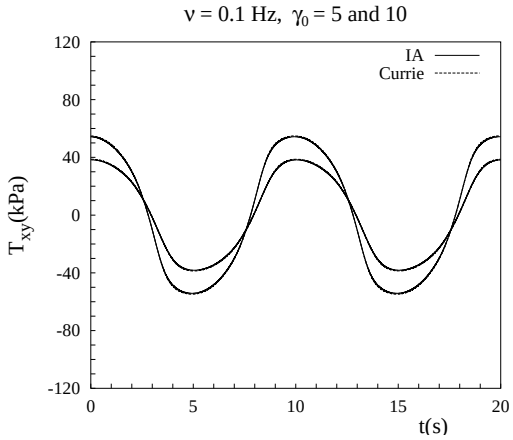

(a)

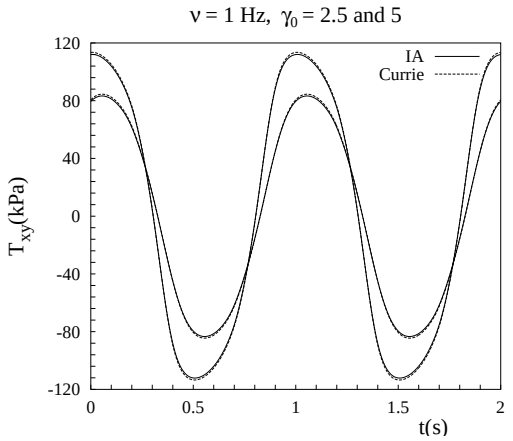

(b)

Figure A.6: Comparison of the steady periodic shear stress prediction of the MSF model using the Currie and independent alignment approximation at amplitudes γ_0 indicated in the figures; (a) $\nu = 0.1$ Hz and (b) $\nu = 1$ Hz.

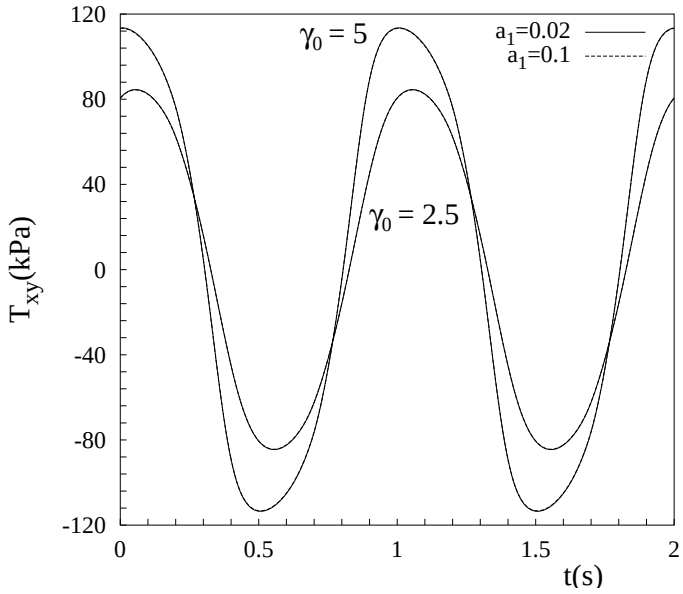

Figure A.7: Steady periodic shear stress at $\nu = 1$ Hz for the MSF model using $a_2 = 2.3$ and values of a_1 indicated in the legend.

of the periodic shear stress signal.

At larger values of γ_0, differences between the various parameter settings in the MSF model and the Doi–Edwards model become more apparent. In Figs. A.9 and A.10we display for each frequency the steady periodic shear stress for the two largest experimentally achievable values of γ_0.

At the lowest strains, the Doi–Edwards model consistently underpredicts the experimental data, while the MSF predictions still show good agreement for all values of a_2 considered, particularly $a_2 = 4$. For the larger γ_0 (and thus larger shear rates) the Doi–Edwards predictions are again fairly close to the experimental data. Surprisingly, the results are in better agreement with the experiments than most of the predictions of the MSF model which has two extra parameters to capture the non-linear behavior. The best MSF parameter for the largest strains seems to be $a_2 = 8$. The parameter values $a_2 = 4$ and particularly $a_2 = 2.3$ overpredict the shear response. This is most apparent at $\nu = 1$ Hz, $\gamma_0 = 5$ which has the highest maximum shear rate. We note in passing that the Giesekus model also overpredicts the experimental signal at more nonlinear flow conditions [52]. At $\nu = 1$ Hz, $\gamma_0 = 5$ the predicted shear stress amplitude is for example 117 kPa for the Giesekus model, while the largest amplitude that

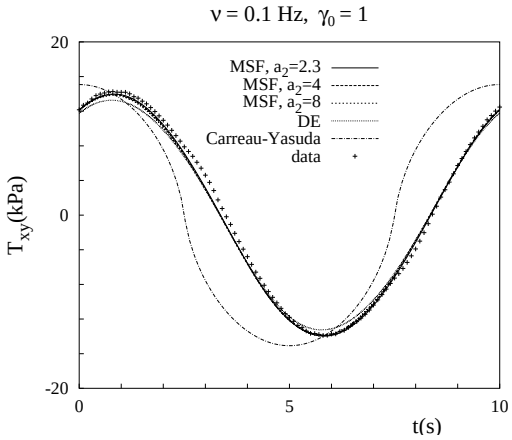

(a)

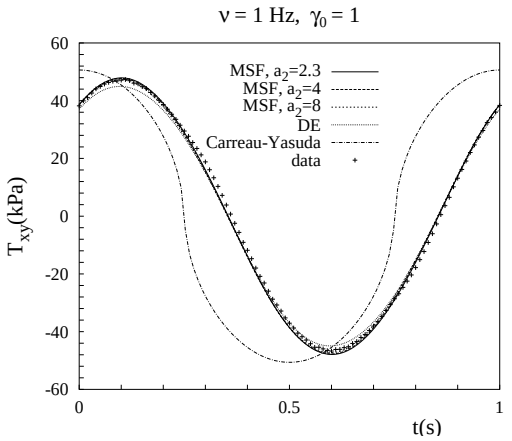

(b)

Figure A.8: Periodic shear stress at moderate shear rates predicted by the viscous and viscoelastic models together with the Finathene data. Frequencies and strains indicated in the figures.

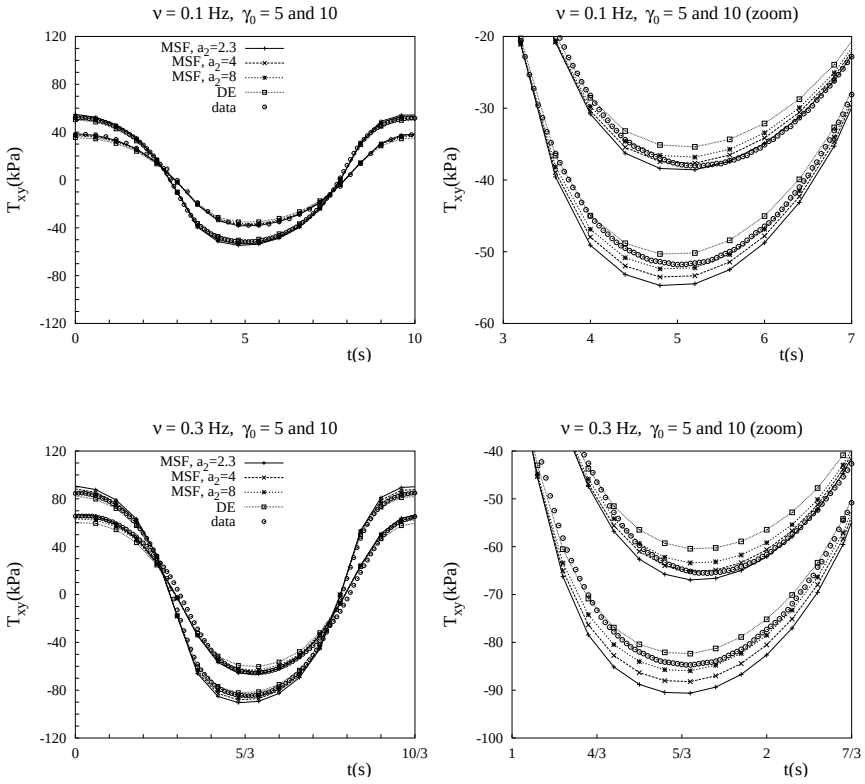

Figure A.9: Comparison of MSF model using values of a_2 as in the legends and Doi–Edwards model with periodic shear stress data for Finathene melt [52]. Left column: one period; right column: zoom around minimum.

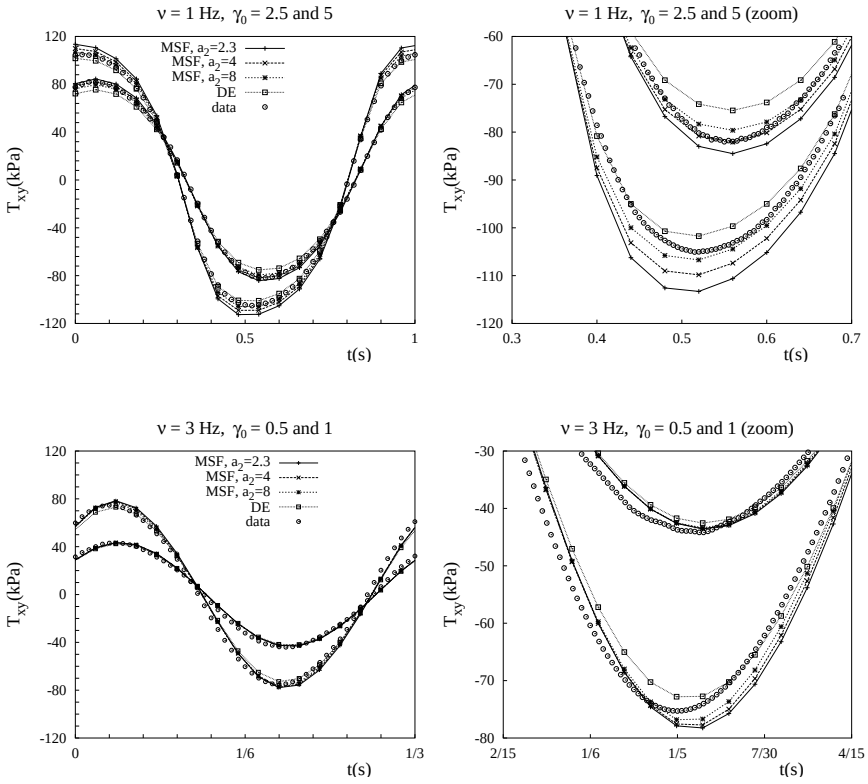

Figure A.10: Comparison of MSF model using values of a_2 as in the legends and Doi–Edwards model with periodic shear stress data for Finathene melt [52]. Left column: one period; right column: zoom around minimum.

occurs for the MSF model is 113.5 kPa for $a_2 = 2.3$. At this amplitude and frequency, the amplitude of the experimental signal 106 kPa is best predicted by $a_2 = 8$ which gives an amplitude of 106.8 kPa. The Doi–Edwards model slightly underpredicts the amplitude, 101.8 kPa. Similar trends are visible at the lower frequencies $\nu = 0.1$ Hz and $\nu = 0.3$ Hz. At $\nu = 3$ Hz no data are available at high enough γ_0 to confirm the counter intuitive result that the Doi–Edwards model gives better predictions at large strains (large shear rates). It is remarkable that at corresponding values of the shear rate, the steady shear viscosity data in Fig. A.1 are better predicted by the MSF and Giesekus model than by the Doi–Edwards model which shows a stronger underprediction of the shear viscosity at high shear rates. We also observe that the LAOS simulations are more sensitive to changes in the parameter a_2 than steady shear flow at corresponding shear rates. This indicates that large oscillatory shear might be a better flow to determine the nonlinear parameters that are important for shearing flows.

The Lissajous plot for a frequency $\nu = 1$ Hz and all experimentally available strain amplitudes are depicted in Fig. A.11. All viscoelastic models predict the deviation from an ellipsoidal shape that is characteristic for the nonlinear response at large strains. Quantitative differences are observed at the largest strain $\gamma_0 = 5$ for the Giesekus model and the MSF model, particularly with $a_2 = 2.3$ and to a lesser extent with $a_2 = 4$. At this strain, predictions of the MSF model with $a_2 = 8$ and Doi–Edwards model are in good agreement with the experimental data. At lower strains, however, some discrepancies are noticeable for the Doi–Edwards model. For all viscoelastic models, deviations are in accordance with the over and underprediction of the amplitude of the periodic shear stress signal as a function of time observed in Fig. A.9.

For the first normal stress difference N_1, no experimental data are available. For completeness, we have included the model predictions at experimentally achievable strains for $\nu = 1$ Hz in Fig. A.12. The periodic N_1 response has a period that is half of the corresponding shear stress signal and has a non-zero average. All models predict the same phase shift for all strains and nearly the same minimum value of N_1. The difference between the models lie in the maxima of the amplitudes. Similar to the periodic shear stress, the Doi–Edwards model predicts the lowest and the MSF model with smallest value of a_2 the largest amplitude. Different magnitudes of the amplitudes become already apparent at relatively low strains of $\gamma = 1$ where the shear stress predictions are still very similar, particularly for the various values of a_2 of the MSF model (Fig. A.8). The periodic normal stress, however, can clearly be distinguished and differences between the models continue to grow when the strain is increased. It would be interesting to compare these results with experimental data to establish whether the Doi–Edwards model also better predicts the first normal stress difference at high strains.

Differences between the model predictions are better quantified in the frequency

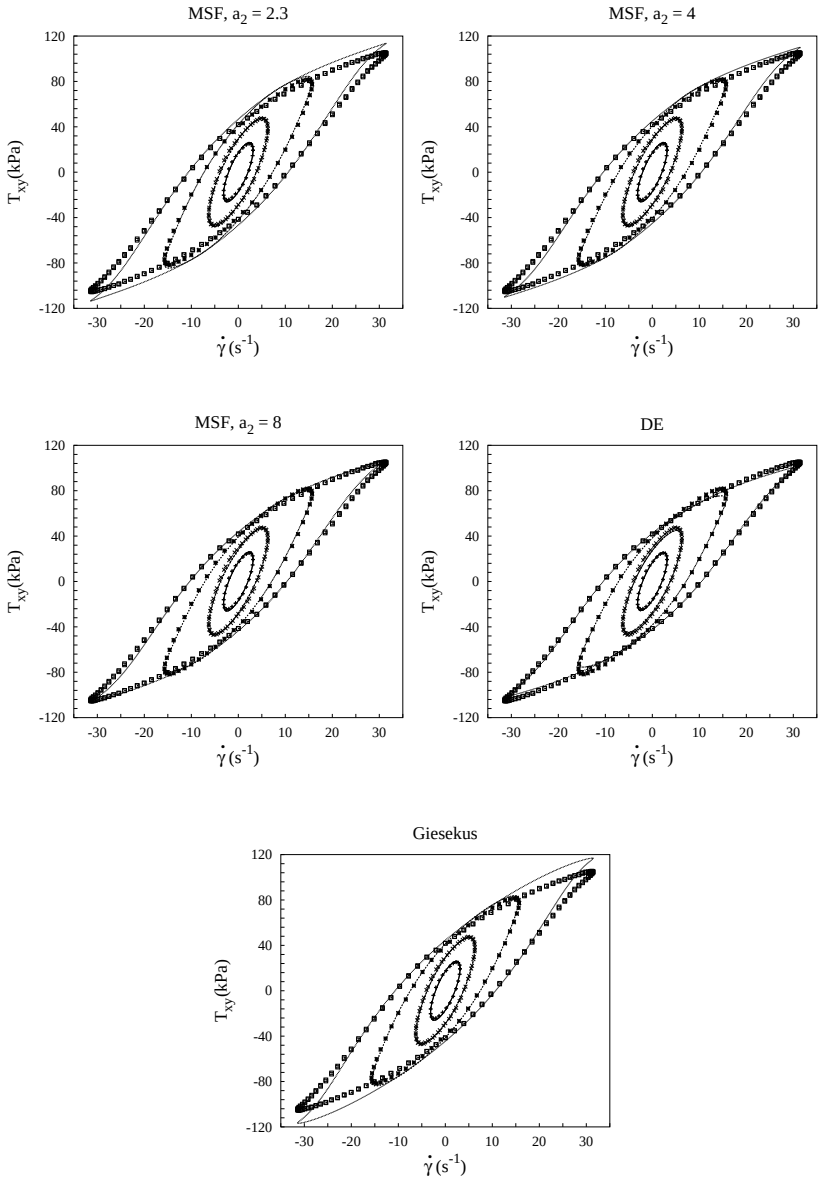

Figure A.11: Lissajous plots for $\nu = 1$ Hz for Finathene data of [52] and model predictions. Strain amplitudes γ_0 are 0.5, 1, 2.5, and 5 (from innermost to outermost loops).

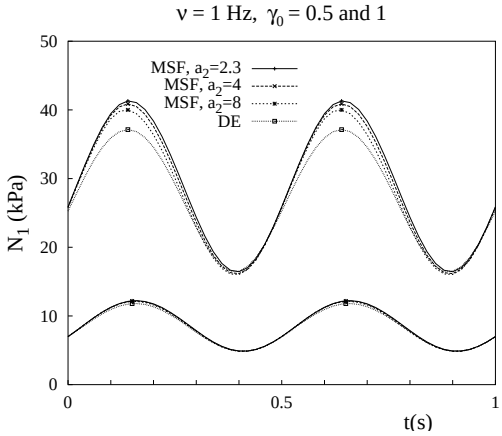

(a)

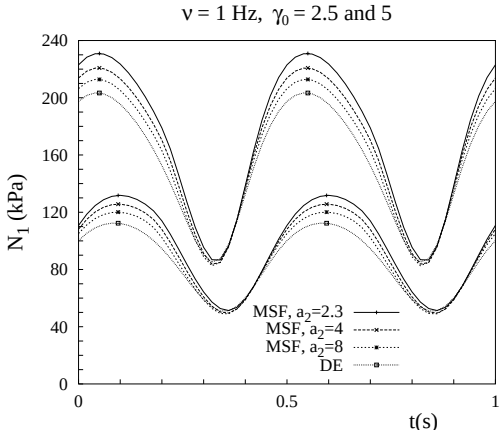

(b)

Figure A.12: Comparison of N_1 predictions for the MSF model using values of a_2 as indicated in the legends and the Doi–Edwards model.

domain than in the time domain. Under more non-linear flow conditions, the higher odd harmonics become more significant. The even harmonics should vanish except for some numerical noise. For the following computations the order of magnitude of the even harmonics was at least 6 orders lower than that of the largest odd harmonics. We focus on the two highest experimentally achievable amplitudes at a low frequency of $\nu = 0.1$ Hz and a high frequency of $\nu = 1$ Hz.

We first consider the two highest experimentally achievable strains at the lowest frequency $\nu = 0.1$ Hz. Table A.1 shows the Fourier coefficients A_n and B_n for the MSF model using various values of a_2. At this low frequency the response in phase with

		A_n(kPa)				B_n(kPa)			
γ_0	n	Exp.	$a_2 = 2.3$	$a_2 = 4$	$a_2 = 8$	Exp.	$a_2 = 2.3$	$a_2 = 4$	$a_2 = 8$
5	1	10.9	9.07	8.69	8.39	38.8	39.7	38.9	38.1
	3	-2.84	-3.32	-3.25	-3.13	-0.34	-0.598	-0.761	-0.847
	5	0.259	0.146	0.199	0.231	-0.534	-0.499	-0.499	-0.487
	7	0.027	0.139	0.159	0.160	0.116	0.001	0.029	0.068
10	1	8.44	7.41	7.14	6.94	55.3	58.7	57.5	56.4
	3	-4.15	-4.92	-4.70	-4.51	-3.43	-3.75	-3.83	-3.85
	5	1.38	1.48	1.47	1.43	-0.219	-0.505	-0.391	-0.311
	7	-0.295	-0.030	-0.073	-0.096	0.37	0.435	0.431	0.419

Table A.1: Amplitudes A_n and B_n of the odd harmonics (kPa) for $\nu = 0.1$ Hz. Comparison of experimental data and MSF results using various values of a_2.

the shear rate is dominating and becomes more dominant when the strain is increased. This is correctly predicted by the MSF model for all parameter values considered. Furthermore, the MSF model predicts the signs of all Fourier coefficients correctly. There are only small quantitative differences. At the low strain $\gamma_0 = 5$, the low harmonics agree best for $a_2 = 4$, particularly the dominating amplitude B_1 which corresponds to the lost work per cycle [48]. At the high strain $a_2 = 8$ gives the best agreement for the dominating amplitude B_1. This explains the better agreement of $a_2 = 4$ at $\gamma_0 = 5$ and of $a_2 = 8$ at $\gamma_0 = 10$ in Fig. A.9.

The amplitudes of the first four non-zero harmonics for the Doi–Edwards, Carreau–Yasuda, and Giesekus model are tabulated in Table A.2. The amplitudes of the Doi–Edwards model closely follow the MSF results with $a_2 = 8$, with the exception of B_1 which is somewhat lower. At $\gamma_0 = 5$, the underprediction of the amplitude of the experimental shear stress signal in Fig. A.9 is caused by an underprediction of the first harmonics A_1 and B_1. The higher harmonics of the Doi–Edwards model are, however, in good agreement with the experimental data, while the Giesekus model predicts the signs of some higher harmonics incorrectly. It is remarkable that at the larger strain

		A_n(kPa)				B_n(kPa)			
γ_0	n	Exp.	DE	CY	G	Exp.	DE	CY	G
5	1	10.9	8.06	-	8.19	38.8	36.6	39.3	39.2
	3	-2.84	-3.02	-	-2.90	-0.34	-0.799	-5.29	-0.163
	5	0.259	0.297	-	-0.124	-0.534	-0.499	2.30	-0.704
	7	0.027	0.103	-	0.151	0.116	0.106	-1.32	-0.062
10	1	8.44	6.70	-	6.51	55.3	54.1	56.2	59.4
	3	-4.15	-4.34	-	-4.34	-3.43	-3.71	-7.76	-3.27
	5	1.38	1.42	-	1.20	-0.219	-0.284	3.43	-1.11
	7	-0.295	-0.152	-	0.388	0.37	0.411	-2.01	0.419

Table A.2: Amplitudes A_n and B_n of the odd harmonics (kPa) for $\nu = 0.1$ Hz. Comparison of experimental data, Doi–Edwards, inelastic Carreau–Yasuda model, and Giesekus model. Data for the Giesekus model are from [52].

of $\gamma_0 = 10$, the differences with the experimental A_1 and B_1 are considerably smaller, resulting in a slightly better agreement with the experimental data than the best MSF model at this γ_0. Furthermore, the higher harmonics of the Doi–Edwards model are in excellent agreement with the experimental data while the Giesekus model shows again much larger deviations and predicts some signs incorrectly.

At the frequency $\nu = 0.1$ Hz and at the strain values in Table A.2, the Carreau–Yasuda model is still able to predict correctly the coefficient B_1, i.e. the lost work per cycle. The amplitudes B_3, B_5, and B_7, however, are off by a factor 2 to 10 and these might have the wrong sign. Furthermore, the inelastic model only predicts non-zero values for the coefficients B_n and is therefore incapable to predict the phase shift in the shear stress response.

At the frequency $\nu = 1$ Hz, the response in phase with the strain is much larger than for the low frequency of $\nu = 0.1$ Hz. This is correctly predicted by the MSF model. The deviations between the experiments and the MSF results are caused by an overprediction of B_1, as can be observed from Table A.3. For the parameter value $a_2 = 2.3$, the value of B_1 is overpredicted by at least 5% and deviations become larger when the strain increases. For larger values of a_2, the deviations from the experimentally obtained B_1 become smaller. Particularly $a_2 = 8$ agrees well with the experimental data. For some other amplitudes like A_3 and B_3, however, we then find larger differences with the experiments. These amplitudes are off by at least 25%.

Table A.4 shows the corresponding results for the Doi–Edwards, Giesekus, and Carreau–Yasuda model. In this more non-linear regime, the purely viscous model is not capable to predict any of the amplitudes correctly. Also B_1 is now overpredicted

		A_n(kPa)				B_n(kPa)			
γ_0	n	Exp.	$a_2 = 2.3$	$a_2 = 4$	$a_2 = 8$	Exp.	$a_2 = 2.3$	$a_2 = 4$	$a_2 = 8$
2.5	1	38.0	38.6	37.0	35.6	74.6	79.2	77.7	75.7
	3	-2.92	-4.09	-4.38	-4.44	2.40	1.53	1.26	0.977
	5	-0.04	-0.458	-0.550	-0.576	-0.512	-0.082	-0.178	-0.346
	7	0.098	0.100	0.128	0.161	0.296	-0.083	-0.073	-0.029
5	1	33.1	34.5	33.0	31.9	108	117	114	111
	3	-9.66	-12.4	-12.1	-11.7	-1.23	-1.79	-2.43	-2.75
	5	0.817	0.467	0.670	0.785	-1.62	-1.84	-1.83	-1.77
	7	0.075	0.519	0.595	0.599	0.412	-0.008	0.095	0.238

Table A.3: Amplitudes A_n and B_n of the odd harmonics (kPa) for $\nu = 1$ Hz. Comparison of experimental data and MSF results using various values of a_2.

		A_n(kPa)				B_n(kPa)			
γ_0	n	Exp.	DE	CY	G	Exp.	DE	CY	G
2.5	1	38.0	34.1	-	38.2	74.6	71.6	89.5	77.8
	3	-2.92	-4.52	-	-3.45	2.40	1.14	-12.6	2.31
	5	-0.04	-0.274	-	-0.474	-0.512	-0.538	5.65	-0.227
	7	0.098	0.063	-	-0.008	0.296	-0.025	-3.35	-0.059
5	1	33.1	30.7	-	35.1	108	106	127	119
	3	-9.66	-11.2	-	-10.2	-1.23	-2.46	-18.0	-0.211
	5	0.817	0.996	-	-0.492	-1.62	-1.85	8.11	-2.42
	7	0.075	0.391	-	0.492	0.412	0.385	4.83	-0.242

Table A.4: Amplitudes A_n and B_n of the odd harmonics (kPa) for $\nu = 1$ Hz. Comparison of experimental data, Doi–Edwards, inelastic Carreau–Yasuda model, and Giesekus model. Data for the Giesekus model are from [52].

considerably. The Doi–Edwards model underpredicts both A_1 and B_1 at the lower strain $\gamma_0 = 2.5$. For this strain, the amplitudes of the low harmonics are better predicted by the Giesekus and MSF model. The higher harmonics, which arise due to non-linear effects, are again much better predicted by the Doi–Edwards than by the Giesekus model. For the more non-linear regime at the higher strain, the Doi–Edwards model does not only show better agreement with experimental data for the higher harmonics. Also the dominating term B_1 is much better predicted than the Giesekus model does. This confirms the counter intuitive result found for the lower frequency of $\nu = 0.1$ Hz that the Doi–Edwards model, which has no nonlinear parameters and underpredicts the steady shear viscosities at high rates, is more accurate in the more nonlinear regimes.

Figure A.13 shows the model predictions of the MSF and Doi–Edwards model outside the experimental window. To compare the model predictions with a macroscopic stress model, results for the Giesekus model have been included as well. All models predict the same trends at large strains, for example, the same sign is predicted for all Fourier coefficients B_n and A_n at large strains. The dominating amplitude is B_1, while the magnitude of A_1 decreases at large strains and reaches a plateau. For the higher harmonics, all amplitudes B_n in phase with the shear seem to reach a higher magnitude at large strains than the corresponding amplitudes A_n that are in phase with the strain. The Fourier coefficient B_n seems to continue to increase in magnitude for a much longer range of strains than the corresponding A_n, which reaches a plateau value. For the two lowest harmonics, the plateau is reached at medium strains of 10. For the higher harmonics much higher strains are necessary. Quantitatively, however, there are differences between the models. Only for A_1, all models predict the same values. For all other Fourier coefficients, the Doi–Edwards model predicts the lowest magnitudes. At large strains, the amplitudes are considerably lower than those of the MSF model with $a_2 = 8$. For the MSF model, the magnitudes of the odd harmonics increase when the parameter a_2 is decreased. The magnitudes predicted by the MSF model with $a_2 = 2.3$ are, however, still considerably lower than those predicted by the Giesekus model. Particularly for the dominant amplitude B_1 the molecular models predict significantly lower magnitudes at large strains. This is consistent with the smaller time overshoots for these models in the transient shear viscosity in Fig. A.3(a). Whether the trends at large strains are correct and whether the Doi–Edwards predictions are still more accurate than those of the nonlinear models remains to be established.

A.8 Concluding remarks

We have evaluated the rheometrical response of the integral molecular stress function model in large amplitude oscillatory shear. For reasons of efficiency, we modified the deformation field method to avoid the restrictive time step constraint resulting from

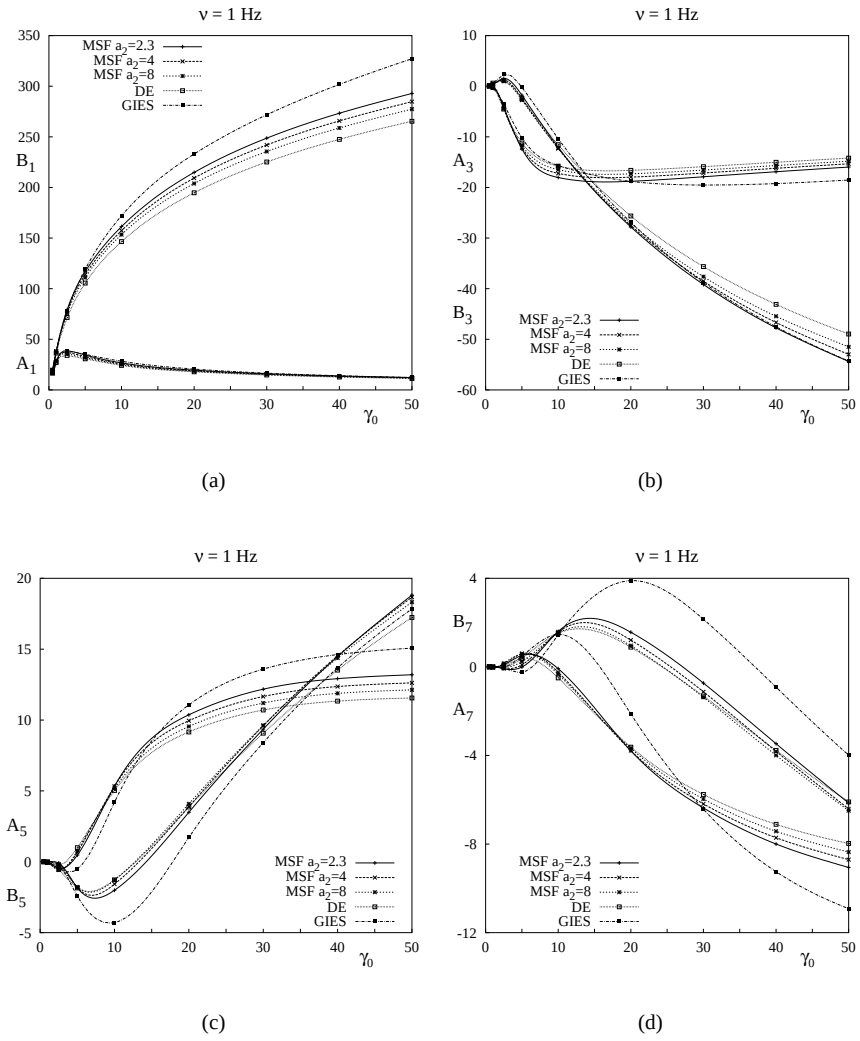

Figure A.13: Amplitudes A_n and B_n of the odd harmonics (kPa) outside the experimental window for MSF model using values of a_2 as in the legends. The Doi–Edwards and Giesekus model are included for comparison.

the discontinuous Galerkin method used in [67]. The new technique is both accurate and efficient for the LAOS computations we performed.

In LAOS, the MSF model only has one relevant material parameter to describe the nonlinear material response. By fitting this parameter to steady shear data of a linear high-density polyethylene melt, the MSF model is able to predict qualitatively and quantitatively the response in large amplitude oscillatory shear. Up to medium strains, results agree very well with experimental data and are comparable with those of a six-mode Giesekus fluid, having six parameters to describe the nonlinear material response. At medium strains the nonlinear response becomes important. As expected, the introduction of the molecular stress function results in better predictions than the basic Doi–Edwards theory which has no material parameters to describe the nonlinear response. Although correctly predicting the phase shift, the DE model underpredicts the amplitude of the experimental signal. This is caused by an underprediction of the amplitude of the most dominant odd harmonics.

At the highest experimentally achievable strains both the MSF and Giesekus model overpredict the amplitude of the periodic shear stress, although this is more significant for the Giesekus model. At these strains, however, it is the Doi–Edwards model that shows excellent agreement with the experimental data. In the time domain it only slightly underpredicts the amplitude of the periodic shear stress. In the frequency domain the correspondence of both the dominant harmonic and the higher odd harmonics is striking. We recall that the DE model does not have any nonlinear parameters and underpredicts the steady shear stress at high shear rates. This is a remarkable and unexpected result indeed. Whether this trend continues at higher strains remains to be established. Since the Doi–Edwards model is well known to underpredict experimental data in start-up of shear and steady shear flows, this also raises the question whether the experimental data are somewhat inaccurate at high strains. Further experimental results are clearly needed to confirm our counter intuitive findings at high strains.

Bibliography

[1] G Tsolou, VG Mavrantzas, and DN Theodorou. Detailed atomistic molecular dynamics simulation of cis-1,4-poly(butadiene). *Macromolecules*, 38(4):1478–1492, 2005.

[2] VA Harmandaris, VG Mavrantzas, DN Theodorou, M Kroger, J Ramirez, HC Ottinger, and D Vlassopoulos. Crossover from the rouse to the entangled polymer melt regime: Signals from long, detailed atomistic molecular dynamics simulations, supported by rheological experiments. *Macromolecules*, 36(4):1376–1387, 2003.

[3] R. Keunings. On the peterlin approximation for finitely extensible dumbbels. *J. Non Newtonian Fluid Mech.*, 68:85–100, 1997.

[4] C. Tsenoglou. Viscoelasticity of binary polymer blends. *ACS Polym. Prepr.*, 28:185–186, 1987.

[5] J. Des Cloizeaux. Double reptation *vs* simple reptation in polymer melts. *J. Europhys. Lett.*, 5:437–442, 1988.

[6] C. Pattamaprom, R.G. Larson. Constraint release effects in monodisperse and bidisperse polystyrenes in fast transient shearing flows. *Macromolecules*, 34:5229–5237, 2001.

[7] X. Ye, R.G. Larson, C.J. Pattamaprom, T. Shridar. Extensional properties of monodisperse and bidisperse polystyrene solutions. *J. Rheol.*, 47(2):443–468, March 2003.

[8] A. Bach, K. Almdal, H.K. Rasmussen, O. Hassager. Elongational viscosity of narrow molar mass distribution polystyrene. *Macromolecules*, 36(14):5174–5179, 2003.

[9] G. Marrucci, F. Greco, G. Ianniruberto. Integral and differential constitutive equations for entangled polymers with simple versions of CCR and force balance on entanglements. *Rheol. Acta*, 40(2):98–103, 2001.

[10] M. H. Wagner, P. Rubio, and H. Bastian. The molecular stress function model for polydisperse polymer melts with dissipative convective constraint release. *J. Rheol.*, 45:1387–1412, 2001.

[11] P.G. De Gennes. Reptation of a polymer chain in the presence of fixed obstacles. *J. Chem. Phys.*, 55:572–579, 1971.

[12] M. Doi, S.F. Edwards. *The Theory of Polymer Dynamics*. Oxford University Press, 1986.

[13] C. Pattamaprom, R.G. Larson, T.J. Van Dyke. Quantitative predictions of linear viscoelastic rheological properties of entangled polymers. *Rheol. Acta*, 39(6):517–531, 2000.

[14] F. Léonardi, J-C. Majesté, A. Allal, G. Marin. Rheological models based on the double reptation mixing rule : The effects of a polydisperse environment. *J. Rheol.*, 44:675–692, 2000.

[15] E. van Ruymbeke, R. Keunings, V. Stéphenne, A Hagenaars, C. Bailly. Evaluation of reptation models for predicting the linear viscoelastic properties of entangled linear polymers. *Macromolecules*, 35(7):2689–2699, 2002.

[16] A.E. Likhtman, T.C.B. McLeish. Quantative theory for linear dynamics of linear entangled polymers. *Macromolecules*, 35:6332–6343, 2002.

[17] S.T. Milner, T.C.B. McLeish. Reptation and contour-length fluctuations in melts of linear polymers. *Phys. Rev. Lett.*, 81(3):725–728, 1998.

[18] S.T. Milner, T.C.B. McLeish. Parameter-free theory for stress relaxation in star polymer melts. *Macromolecules*, 30:2159–2166, 1997.

[19] A.L. Frischnecht, S.T. Milner, A. Pryke, R.N. Young, R. Hawkins, T.C.B. McLeish . Rheology of three-arm asymmetric star polymer melts. *Macromolecules*, 35:4801–4820, 2002.

[20] S.T. Milner, T.C.B. McLeish, R.N. Young, A. Hakiki, J.M. Johnson. Dynamic dilution, constraint-release, and star-linear blends. *Macromolecules*, 31:9345–9353, 1998.

[21] S.J. Park, R.G. Larson. Tube dilution and reptation in binary blends of monodisperse linear polymers. *Macromolecules*, 37:597–604, 2004.

[22] G. Marrucci. Relaxation by reptation and tube enlargement: A model for polydisperse polymers. *J. Polym. Sci., Polym. Phys.*, 23:159–177, 1985.

[23] R.S. Graham, A.E. Likhtman, T.C.B. McLeish, S.T. Milner. Microscopic theory of linear entangled polymer chains under rapid deformation including chain stretch and convective constraint release. *J. Rheol.*, 47(5):1171–1200, 2003.

[24] C.C. Hua, J.D. Schieber, D.C. Venerus. Segment connectivity, chain-length breathing, segmental stretch, and constraint release in reptation models. i. theory and single-step strain predictions. *J. Chem. Phys.*, 109(22):10018–10032, 1998.

[25] J.L. Viovy, M. Rubinstein, R.H. Colby. Constraint release in polymer melts: Tube reorganization versus tube dilation. *Macromolecules*, 24(12):3587–3596, 1991.

[26] D.W. Mead, R.G. Larson, M. Doi. A molecular theory for fast flows of entangled polymers. *Macromolecules*, 31(22):7895–7914, 1998.

[27] R.H. Colby, M. Rubinstein. Two-parameter scaling for polymers in ? solvents. *Macromolecules*, 23:2753–2757, 1990.

[28] J.H. Lee, L.A. Archer. Stress relaxation of star/linear polymer blends. *Macromolecules*, 35:6687–6696, 2002.

[29] E. van Ruymbeke, R. Keunings, C. Bailly. Prediction of linear viscoelastic properties for polydisperse mixtures of entangled star and linear polymers: Modified tube-based model and comparison with experimental results. *J. Non Newtonian Fluid Mech.*, In press, 2005.

[30] Y. Masubuchi, J. Takimoto, K. Koyama, G. Ianniruberto, G. Marrucci, F. Grecco. Brownian simulations of a network of reptating primitive chains. *J. Chem. Phys.*, 115(9):4387–4394, 2001.

[31] J. Des Cloizeaux. Relaxation of entangled polymers in melts. *Macromolecules*, 23(17):3992–4006, 1990.

[32] J. Des Cloizeaux. Relaxation and viscosity anomaly of melts made of long entangled polymers. *Macromolecules*, 23(21):4678–4687, 1990.

[33] A. Leygue, C. Bailly, R. Keunings. A differential formulation of thermal constraint release for entangled polymers. *J. Non Newtonian Fluid Mech.*, In press, 2005.

[34] L.G. Leal G.H. McKinley A.E. Likhtman R.G. Larson, T. Shridar and T.C.B. McLeish. Definitions of entanglement spacing and time constants in the tube model. *J. Rheol.*, 47:809–818, 2003.

[35] A. Leygue, C. Bailly, R. Keunings. A differential tube-based model for predicting the linear viscoelastic moduli of polydisperse entangled linear polymers. *Submitted*, 2005.

[36] G. Marrucci, G. Ianniruberto. Interchain pressure effect in extensional flows of entangled polymer melts. *Macromolecules*, 37:3934–3942, 2004.

[37] G. Marrucci, N. Grizzuti. Fast flows of concentrated polymers-predictions of the tube model on chain stretching. *Gazz. Chim. Ital.*, 118:179–185, 1988.

[38] G. Marrucci. Dynamics of entanglements: A nonlinear model consistent with the cox-merz rule. *J. Non Newtonian Fluid Mech.*, 62:279–289, 1996.

[39] G. Ianniruberto, G. Marrucci. On compatibility of the cox-merz rule with the model of Doi and Edwards. *J. Non Newtonian Fluid Mech.*, 65(2-3):241–246, 1996.

[40] A. Leygue, A.N. Beris, R. Keunings. A constitutive equation for entangled linear polymers inspired by reptation theory and consistent with non-equilibrium thermodynamics. *J. Non Newtonian Fluid Mech.*, 101:95–111, 2001.

[41] G. Marrucci, G. Ianniruberto. Flow-induced orientation and stretching of entangled polymers. *Philos. Trans. R. Soc. A*, 361:677–687, 2003.

[42] P. Wapperom, R. Keunings. Impact of decoupling approximation between stretch and orientation in rheometrical and complex flow of entangled polymers. *J. Non Newtonian Fluid Mech.*, 122(1-3):33–43, 2004.

[43] M. Denberg. Study of the stretch dynamics of the craft model using a monte-carlo method. Technical report, Université catholique de Louvain, 2004.

[44] A.N. Beris, B.J. Edwards. *Thermodynamics of Flowing Systems with Internal Microstructure*. Oxford University Press, 1994.

[45] A. N. Beris. personal communication.

[46] P.K. Bhattacharjee, J.P. Oberhauser, G.H. McKinley, L.G. Leal, T. Shridar. Extensional rheometry of entangled solutions. *Macromolecules*, 35:10131–10148, 2002.

[47] A. Leygue, C. Bailly, R. Keunings. A tube-based constitutive equation for polydisperse entangled linear polymers. *Submitted*, 2005.

[48] A. J. Giacomin and J. M. Dealy. Using large-amplitude oscillatory shear. In A. A. Collyer and D. W. Clegg, editors, *Rheological measurements*, pages 327–356. Kluwer Academic Publisher, Dordrecht, 2nd edition, 1998.

[49] M. Wilhelm, D. Maring, and H. W. Spiess. Fourier-transform rheology. *Rheol. Acta*, 37:399–405, 1998.

[50] M. Wilhelm, P. Reinheimer, and M. Ortseifer. High sensitivity Fourier-transform rheology. *Rheol. Acta*, 38:349–356, 1999.

[51] HG Sim, KH Ahn, and SJ Lee. Large amplitude oscillatory shear behavior of complex fluids investigated by a network model: a guideline for classification. *J. Non Newtonian Fluid Mech.*, 112(2-3):237–250, 2003.

[52] B. Debbaut and H. Burhin. Large amplitude oscillatory shear and Fourier transform rheology for a high-density polyethylene: Experiments and numerical simulation. *J. Rheol.*, 46:1155–1176, 2002.

[53] C. Bailly C-Y. Liu, R. Keunings. Evaluation of different methods for the determination of the plateau modulus gn0. *In preparation*, 2005.

[54] D.J. Olson, E.F. Brown, W.R. Burghardt. Second normal stress difference relaxation in a linear polymer melt following step-strain. *J. Polym. Sc. Part B*, 36(14):2671–2675, 1998.

[55] G. Marrucci, F. Greco, G. Ianniruberto. Simple strain measure for entangled polymers. *J. Rheol.*, 44(4):845–854, 2000.

[56] P. Wapperom, R. Keunings. Simulation of linear polymer melts in transient complex flow. *J. Non Newtonian Fluid Mech.*, 95(1):67–83, 2000.

[57] H.C. Öttinger, M. Grmela. Dynamics and thermodynamics of complex fluids. ii. illustration of a general formalism. *Phys. Rev. E*, 56(6):6633–6655, 1997.

[58] S.R. De Groot, P. Mazur. *Non-Equilibrium Thermodynamics*. North Holland Publishing Company : Amsterdam, 1969.

[59] M. Grmela. Hamiltonian dynamics of incompressible elastic fluids. *Phys. Lett. A*, 130:81–86, 1988.

[60] B.J. Edwards, A.N. Beris. Noncanonical poisson bracket for nonlinear elasticity with extensions to viscoelasticity. *J. Phys. A: Math. Gen.*, 24:2461–2480, 1991.

[61] G. Nicolis. Irreversible thermodynamics. *Rep. Prog. Phys.*, 42:225–268, 1979.

[62] R.B. Bird, C.F. Curtiss, R.C. Armstrong, O. Hassager. *Dynamics of Polymeric Liquids, Vol. 2, Kinetic Theory*. Wiley-Interscience, New York, 2nd edition, 1987.

[63] G. Marrucci. personal communication.

[64] S.G. Kalogrianitis, J.W. van Egmond. Full tensor optical rheometry of polymer fluids. *J. Rheol.*, 41(2):343–364, 1997.

[65] W. Philippoff. Vibrational measurements with large amplitudes. *Trans. Soc. Rheol.*, 10:317–334, 1966.

[66] D. van Dusschoten, M. Wilhelm, and H. W. Spiess. Two-dimensional Fourier transform rheology. *J. Rheol.*, 45:1319–1339, 2001.

[67] M. A. Hulsen, E. A. J. F. Peters, and B. H. A. A. van den Brule. A new approach to the deformation fields method for solving complex flows using integral constitutive equations. *J. Non Newtonian Fluid Mech.*, 98:201–221, 2001.

[68] P. K. Currie. Constitutive equations for polymer melts predicted by the Doi–Edwards and Curtiss–Bird kinetic theory models. *J. Non Newtonian Fluid Mech.*, 11:53–68, 1982.

[69] M. H. Wagner, M. Yamaguchi, and M. Takahashi. Quantitative assesssment of strain hardening of low-density polyethylene melts by the molecular stress function model. *J. Rheol.*, 47:779–793, 2003.

[70] R. B. Bird, R. C. Armstrong, and O. Hassager. *Dynamics of Polymeric Liquids*, volume 1. Wiley-Interscience, New York, 2nd edition, 1987.

[71] M. H. Wagner, H. Bastian, A. Bernnat, S. Kurzbeck, and C. K. Chai. Determination of elongational viscosity of polymer melts by RME and Rheotens experiments. *Rheol. Acta*, 41:316–325, 2002.